

# Diboson Production in Proton-Proton Collisions at $\sqrt{s} = 7$ TeV

---

M. Schott,<sup>a,1</sup> J. Zhu<sup>b</sup>

<sup>a</sup>*Johannes Gutenberg-University, Mainz, Germany*

<sup>b</sup>*University of Michigan, Ann Arbor, MI, United States of America, 48103*

*E-mail:* [mschott@cern.ch](mailto:mschott@cern.ch), [junjie@umich.edu](mailto:junjie@umich.edu)

ABSTRACT: This review article summarizes results on the production cross section measurements of electroweak boson pairs ( $WW$ ,  $WZ$ ,  $ZZ$ ,  $W\gamma$  and  $Z\gamma$ ) at the Large Hadron Collider (LHC) in  $pp$  collisions at a center-of-mass energy of  $\sqrt{s} = 7$  TeV. The two general-purpose detectors at the LHC, ATLAS and CMS, recorded an integrated luminosity of  $\approx 5 \text{ fb}^{-1}$  in 2011, which offered the possibility to study the properties of diboson production to high precision. These measurements test predictions of the Standard Model (SM) in a new energy regime and are crucial for the understanding and the measurement of the SM Higgs boson and other new particles. In this review, special emphasis is drawn on the combination of results from both experiments and a common interpretation with respect to state-of-the-art SM predictions.

---

<sup>1</sup>Corresponding author.

---

## Contents

<b>1</b>	<b>Introduction</b>	<b>1</b>
<b>2</b>	<b>Dibosons in the Standard Model</b>	<b>2</b>
2.1	The Electroweak Sector	2
2.2	Diboson Production at the LHC	4
2.3	Event Generation and Available Computer Programs	7
2.4	SM Predictions of Diboson Production Cross Sections	8
2.5	Description of SM Extensions and aTGCs	9
<b>3</b>	<b>Experimental Aspects of Diboson Measurements at the LHC</b>	<b>12</b>
3.1	The LHC machine	12
3.2	The ATLAS and CMS Detectors	13
3.3	Reconstruction Objects for Physics Analysis	14
3.4	Methodology of Cross-Section Measurements at the LHC	17
<b>4</b>	<b>Studies of the <math>WW</math>, <math>WZ</math> and <math>W\gamma</math> final states</b>	<b>19</b>
4.1	$WW$ Analysis	19
4.1.1	Event Selection	19
4.1.2	Background Estimation	21
4.1.3	Cross Section Measurement	22
4.1.4	Derived Results and Discussion	26
4.2	$WZ$ Analysis	27
4.2.1	Event Selection	27
4.2.2	Background Estimation	28
4.2.3	Cross Section Measurement	30
4.2.4	Derived Results and Discussion	32
4.3	$W\gamma$ Analysis	33
4.3.1	Event Selection	33
4.4	Background Estimation	34
4.4.1	Fiducial Cross Section Results	35
4.4.2	Derived Results and Discussion	36
<b>5</b>	<b>Studies of the <math>ZZ^{(*)}</math> and <math>Z\gamma</math> final states</b>	<b>37</b>
5.1	$ZZ^{(*)}$ Analysis	38
5.1.1	Event Selection	39
5.1.2	Background Estimation	40
5.1.3	Inclusive and Fiducial Cross Section Results	41
5.1.4	Derived Results and Discussion	42
5.2	$Z\gamma$ Analysis	44
5.2.1	Event Selection	44

5.2.2	Background Estimation	44
5.3	Cross Section Results	46
5.3.1	Derived Results and Discussion	48
<b>6</b>	<b>Interpretation of Results and Outlook</b>	<b>48</b>
6.1	Inclusive Cross Section Measurements	48
6.2	Limits on Anomalous Triple Gauge Couplings	50
6.3	Outlook on Quartic Gauge Coupling Measurements	53
<b>7</b>	<b>Summary and Outlook</b>	<b>56</b>

---

## 1 Introduction

The Standard Model (SM) of particle physics is a quantum field theory based on the  $SU(3)_C \otimes SU(2)_L \otimes U(1)_Y$  gauge symmetry group and describes the strong, weak and electromagnetic interactions among elementary particles[1]. As a direct consequence of the non-Abelian gauge symmetry of the electroweak sector, i.e. the  $SU(2)_L \otimes U(1)_Y$  gauge group, the SM predicts self-coupling vertices of the gauge bosons. At the Large Hadron Collider (LHC), these vertices lead to the production of diboson final states. Moreover, the discovery of the Higgs boson in the year 2012 [2], [3] was due to its diboson decay channels. The production of pairs of vector bosons is therefore not only an important background for studies of the newly-discovered Higgs boson, but also provides a unique opportunity to test the electroweak sector of the SM.

These precision tests have already a long history in particle physics. The LEP experiments performed precise measurements of the  $e^+e^- \rightarrow W^+W^-$  and  $e^+e^- \rightarrow ZZ$  cross sections as a function of center-of-mass energy[4–7]. The clean experimental signature and nature of the purely electroweak calculations allowed for a precise study of the gauge-group nature of the SM. Limits on possible extensions and deviations from the SM predictions were also drawn. Some of those limits are still the most stringent ones available. Since the  $e^+e^- \rightarrow WW$  cross section depends crucially on the mass of the  $W$  boson ( $m_W$ ), the cross section dependence on the center-of-mass energy allowed for an indirect determination of  $m_W$ .

The Tevatron experiments allowed studies of all possible diboson final states  $W^+W^-$ ,  $W^\pm Z$ ,  $ZZ$ ,  $W\gamma$  and  $Z\gamma$  [8–10]. In contrast to the LEP collider, the bulk part of the production process is governed by the Quantum Chromodynamic (QCD) processes. Nevertheless, precise measurements of these production cross sections allow again tests of the predicted gauge-boson self-interactions and searches for physics beyond the SM.

With the start of the Large Hadron Collider at CERN, a completely new energy regime became accessible, and the corresponding production cross sections increased by more than a factor of five compared to the Tevatron. The increase in available statistics and the

higher center of mass energies allow for an improved study of perturbative Quantum Chromodynamic predictions, which are by now available to next-to-next-to-leading order in the strong coupling constant  $\alpha_s$  for some processes[11]. In addition, for the first time, limits on new physics scenarios that modify the triple gauge coupling vertices could be improved compared to the LEP experiments.

This review article summarizes the results of diboson production cross section measurements at the LHC with a center-of-mass energy of  $\sqrt{s} = 7$  TeV, based on data collected by the ATLAS and CMS experiments in 2011. We present the experimental signatures and the differences between the measurement strategies in detail. Special focus is drawn on combinations of various results from both experiments and their interpretations within the SM. The results published by the ATLAS and CMS collaborations form the basis for this review. The combinations of these results and further derived information have been conducted with great care, but are solely based on the private work of the authors of this article and do not reassemble any official joint ATLAS and CMS effort.

This article is structured as follows. In Sect. 2, we briefly summarize the most important features of the electroweak sector of the SM, the theoretical methodology for the predictions of diboson production in  $pp$  collisions, and the description of new physics scenarios regarding diboson production. The LHC collider, the ATLAS and CMS experiments, as well as further experimental aspects are discussed in Sect. 3. Measurements that are sensitive to the  $WWZ$  and  $WW\gamma$  vertices, i.e. measurements of the  $W^+W^-$ , the  $W^\pm Z$  and the  $W^\pm\gamma$  final states, are presented in Sect. 4. The  $ZZ$  and  $Z\gamma$  final states are sensitive to  $ZZZ$ ,  $ZZ\gamma$  and  $Z\gamma\gamma$  vertices that are not allowed in the SM; they are discussed in Sect. 5. The results on the cross section measurements and the limits on anomalous triple gauge couplings (aTGCs) are interpreted in Sect. 6. In addition, the sensitivity to quartic gauge couplings (QGCs) is briefly discussed. Section 7 summarizes all the results and gives an outlook for future measurements at the LHC.

## 2 Dibosons in the Standard Model

### 2.1 The Electroweak Sector

The Lagrangian of the electroweak sector of the SM can be written as

$$\mathcal{L}_{EW} = \mathcal{L}_{Kin} + \mathcal{L}_N + \mathcal{L}_C + \mathcal{L}_{WWV} + \mathcal{L}_{WWVV} + \mathcal{L}_H + \mathcal{L}_{HV} + \mathcal{L}_Y, \quad (2.1)$$

where the different terms are schematically shown in Fig. 1 as tree-level Feynman diagrams[1]. The free movements of all fermions and bosons are described by the kinematic term  $\mathcal{L}_{Kin}$ . The neutral current interactions, i.e. the exchange of photon and the  $Z$  boson, are summarized in  $\mathcal{L}_N$ . The  $W$  boson interaction to left-handed particles and right-handed anti-particles is represented by the charged current term  $\mathcal{L}_C$ . Since the weak interaction is based on an  $SU(2)_L$  group structure, three-point and four-point interactions of the electroweak gauge bosons appear, denoted by  $\mathcal{L}_{WWV}$  and  $\mathcal{L}_{WWVV}$ . The self-interactions of the Higgs boson and the interaction of the Higgs boson with the electroweak gauge bosons are represented by the terms  $\mathcal{L}_H$  and  $\mathcal{L}_{HV}$ , respectively. The Yukawa couplings between the Higgs field and the fermions is denoted by  $\mathcal{L}_Y$ .

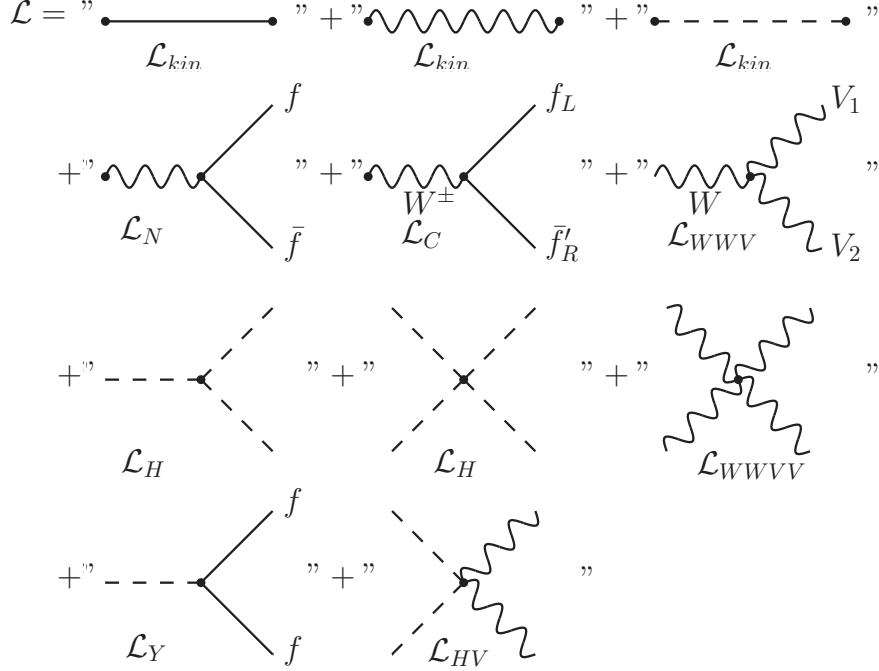


**Figure 1.** Feynman diagrams of tree-level interactions of the Lagrangian describing the electroweak sector of the SM.

The production of single photons and  $Z$  bosons within the SM is given by

$$\mathcal{L}_N = eJ_\mu^{em}A^\mu + \frac{g}{\cos\theta_W}(J_\mu^3 - \sin^2\theta_W J_\mu^{em})Z^\mu, \quad (2.2)$$

where  $J_\mu^{em}$  and  $J_\mu^3$  denote the electromagnetic and weak current,  $A^\mu$  is the photon field, and  $Z^\mu$  is the  $Z$  boson. Each current contains the sum over all fermionic fields weighted by their respective charges. In addition, the weak current  $J_\mu^3$  involves only left-handed particles and right-handed anti-particles. The relative strength of the electromagnetic and weak interactions is described by the weak mixing angle,  $\theta_W$ .

The charged current term,

$$\mathcal{L}_C = -\frac{g}{\sqrt{2}}\left[\bar{u}_i\gamma^\mu\frac{1-\gamma^5}{2}M_{ij}^{CKM}d_j + \bar{\nu}_i\gamma^\mu\frac{1-\gamma^5}{2}e_i\right]W_\mu^+ + h.c. \quad (2.3)$$

describes the production of charged bosons via fermions, i.e.  $f\bar{f}' \rightarrow W^\pm$ . For simplicity, only the terms of the first generation are shown and the quark and lepton spinor fields are labeled by  $u_i, d_j$  and  $\nu_i, e_i$ , respectively. The mixing of quark generations is described by

the CKM matrix  $M_{ij}^{CKM}$ . The  $(1 - \gamma^5)/2$  operator is introduced to describe the exclusive interaction of left-handed particles and right-handed anti-particles with the  $W$  boson.

It should be noted that the terms  $L_N$  and  $L_C$  can lead to diboson final states at hadron colliders through  $t$ - and  $u$ - exchange of a fermion. However, as a direct consequence of the  $SU(2)$  gauge group of the weak interaction, the production of vector boson pairs through the  $s$ -channel process is also allowed. The corresponding term in the Lagrangian reads as

$$\mathcal{L}_{WWV} = -ig \left[ W_{\mu\nu}^+ W^{-\mu} (A^\nu \sin \theta_W - Z^\nu \cos \theta_W) + W_\nu^- W_\mu^+ (A^{\mu\nu} \sin \theta_W - Z^{\mu\nu}) \right]. \quad (2.4)$$

This term leads to TGCs at the tree level. It is thus interesting to experimentally demonstrate that gauge bosons couple not only to electric charge but also to weak isospin. It is apparent from Eqn. 2.4 that the SM allows only  $\gamma WW$  and  $ZWW$  couplings. Various models of physics beyond the SM predict aTGCs but also new vertices like  $ZZZ$ ,  $ZZ\gamma$  and  $Z\gamma\gamma$ .

The last contribution to diboson final states comes from the decay of the Higgs boson, described by

$$\mathcal{L}_{HVV} = \left( gm_W H + \frac{g^2}{4} H^2 \right) \left( W_\mu^+ W^{\nu-} + \frac{1}{2 \cos^2 \theta_W} Z_\mu Z^\mu \right). \quad (2.5)$$

However, for a SM Higgs boson with a mass close to 125 GeV, the decay into a diboson pair must involve at least one off-shell vector boson. This production mode is therefore significantly suppressed if we only consider on-shell vector bosons in the final state.

The vector boson fusion or four-point self-interaction as described by  $L_{WWVV}$ , is not discussed in this review, as the expected production cross sections at 7 TeV  $pp$  collisions are negligible. However it should be noted that this channel has never been experimentally observed and measurements of these processes at 14 TeV would be a crucial test of the SM predictions.

## 2.2 Diboson Production at the LHC

Several introductory articles on the production of vector bosons in hadron collisions are available. Before discussing the experimental results, we summarize here the essential aspects of the theoretical predictions of the diboson production at the LHC along the lines of the following publications. [8, 12–14].

The diboson production at hadron colliders is significantly different than the production mechanism at lepton colliders due to the complicated internal structure of protons. The proton structure can be described phenomenologically by parton density functions (PDFs), written as  $f_{A,q}(x, Q^2)$  for parton-type  $q$  in proton  $A$  with a relative momentum of  $x = p_q/p_A$  in the direction of the proton's motion for an energy scale  $Q^2$  of the scattering process. Here,  $p_q$  and  $p_A$  denote the momenta of the parton and proton, respectively. For the production of vector boson pairs ( $VV$ ), the energy scale is often set to the invariant mass of the two vector bosons, i.e.  $Q^2 = M_{VV}^2$ .

The factorization theorem states that the production cross section in  $pp$  collisions can be expressed by combining PDFs with a fundamental partonic cross section  $\hat{\sigma}_{q\bar{q} \rightarrow VV}$ , illustrated

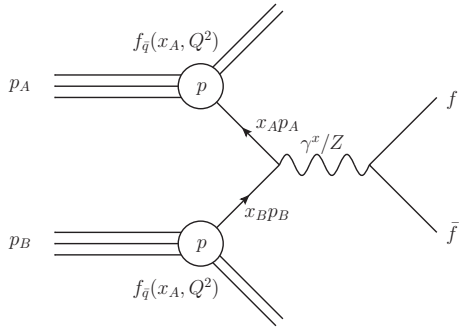


**Figure 2.** Illustration of the factorization theorem used to calculate the production cross section in  $pp$  collisions.

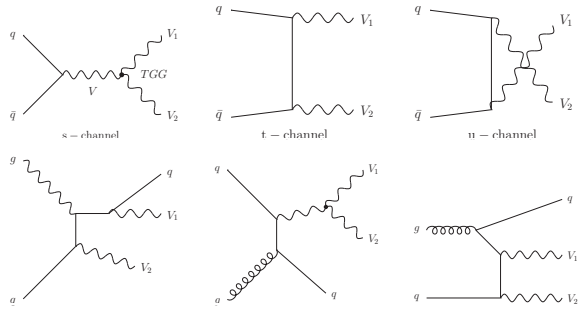


**Figure 3.** LO (top) and NLO (bottom) Feynman diagrams for diboson production.

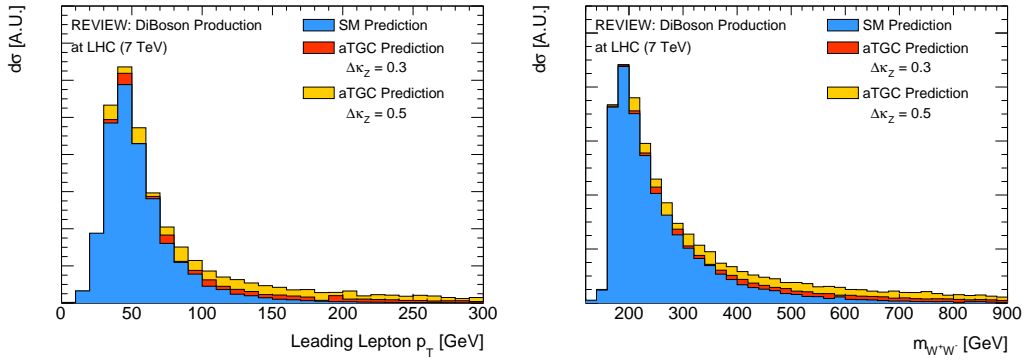


**Figure 4.** Example of an enhanced cross section as a function of the leading lepton transverse momentum (left) and the invariant mass of the  $W^+W^-$  system (right) with two aTGC scenarios.

in Fig. 2:

$$\sigma_{pp \rightarrow VV} = \sum_q \int dx_A dx_B f_{q_B}(x_B, M_{VV}^2) f_{q_A}(x_A, M_{VV}^2) \hat{\sigma}_{q\bar{q} \rightarrow VV}, \quad (2.6)$$

where  $\hat{\sigma}_{q\bar{q} \rightarrow VV}$  is the cross section of the inclusive hard scattering process of two partons leading to two vector bosons in the final state. The sum runs over all quark flavors, and the integration is performed over the momentum fractions of the two colliding partons  $x_A$  and  $x_B$ . The factorization theorem holds not only for inclusive hard-scattering processes but also for perturbative QCD corrections.

The partonic cross section is governed by the  $\mathcal{L}_N$ ,  $\mathcal{L}_C$ , and  $\mathcal{L}_{WV}$  terms of the SM Lagrangian given in Eqn. 2.1. The corresponding leading-order (LO) and some next-to-leading-order (NLO) Feynman diagrams are shown in Fig. 3 for different production channels. It should be noted that  $W\gamma$  and  $Z\gamma$  final states can also be realized by initial and/or final state radiation processes of the participating fermions.

Of special importance is the  $s$ -channel as it involves TGCs that are predicted within the SM. Any new physics model that involves new or alternative interactions between the SM electroweak gauge bosons may change these TGCs and hence change the corresponding

observables. An enhancement of the  $s$ -channel contribution to the full diboson production cross section is predicted to increase with rising parton collision energy  $\hat{s}$ , i.e. with the invariant mass of diboson system  $M_{VV}$ . This dependence is shown in Fig. 4 where an aTGC scenario is assumed for the  $WW(Z/\gamma)$  production vertex. Regions in the phase space that correspond to high center-of-mass energies of the interacting partons therefore provide a high sensitivity to new physics scenarios.

Figure 3 shows some examples of Feynman diagrams due to the NLO QCD corrections. In particular, the quark-gluon fusion in the initial state leads to a significant increase in the production cross section at a  $pp$  collision energy of 7 TeV<sup>1</sup>. The gluon-gluon fusion with fermions in the loop contribute approximately 3%. The NLO QCD corrections have been first calculated in [15–23]. It should be noted that usually additional jets in the  $W^+W^-$  diboson production are experimentally vetoed to reduce the background from the pair production of top quarks. Hence, a significant contribution of the NLO QCD corrections to the  $W^+W^-$  process are not directly studied experimentally.

The most up-to-date QCD calculations include off-shell effects in gluon fusion processes, subsequent decay, and effects of massive quarks in the loop [24]. Leptonic decay modes are accounted for in the narrow-width approximation and include all spin-correlation effects. For predictions beyond the narrow-width approximation, gauge invariance requires the inclusion of single resonant diagrams in the calculations, which was first done in [22]. The next-to-next-to-leading order (NNLO) QCD calculation for the  $ZZ$  production in  $pp$  collisions became available recently [11].

Electroweak corrections have been calculated so far only for the  $W^+W^-$  process [25–29]. Since the electroweak coupling parameter ( $\alpha_{EW}$ ) is small compared to the strong coupling constant ( $\alpha_s$ ), the effects of the EW corrections are expected to be minor. However, EW corrections increase with the square of  $\log(\hat{s})$  and can reach several percent at the energies. While electroweak corrections modify the inclusive production cross section by less than 0.5%, they induce variations up to 10% in the rapidity distribution of the diboson pair. For large diboson invariant masses ( $M_{VV} > 1$  TeV), EW corrections could modify the inclusive production cross section by more than 15% [29]. EW corrections also open the  $W^+W^-$  production via photon-photon fusion (as shown in Fig. 5) since the photon PDFs inside protons are non-vanishing. This channel results in a predicted cross section enhancement of  $\approx 1.5\%$  compared to the LO calculations at  $\sqrt{s} = 7$  TeV.

Finally, the  $W^+W^-$  and  $ZZ$  boson pairs can also be produced via the decay of the SM Higgs boson (as shown in Fig. 6), which is described by the  $\mathcal{L}_{HVV}$  term of the SM Lagrangian. The Higgs boson production is known to NNLO in  $\alpha_s$  [30] and to NLO in  $\alpha_{EW}$  [31]. Since diboson production from the decay of the SM Higgs bosons involves at least one off-shell vector boson, the contribution of this decay channel to the full inclusive diboson production is typically less than 5%, depending on the experimental analysis requirements. Further details are discussed in the experimental sections of this review.

In summary, the rich phenomenology of the electroweak sector can be tested via studies of diboson production at hadron colliders. Four terms on the Lagrangian contribute to the

---

<sup>1</sup>E.g. the  $WW$  cross section increases by  $\approx 25\%$ .



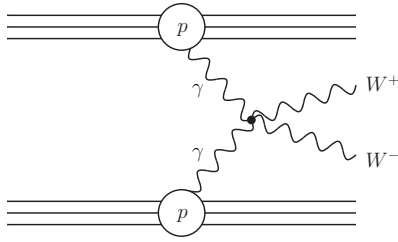


**Figure 5.**  $\gamma\gamma$  fusion contributing to the  $W^+W^-$  production.

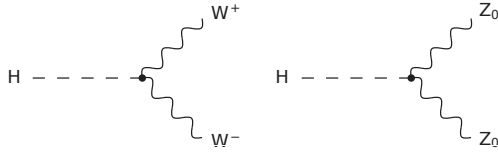


**Figure 6.** Higgs decay to the  $W^+W^-$  and  $ZZ$  final states.

production, namely  $\mathcal{L}_N$ ,  $\mathcal{L}_C$ ,  $\mathcal{L}_{HVV}$ ,  $\mathcal{L}_{WWV}$  and  $\mathcal{L}_{WVWV}$ , and therefore not only the  $SU(2)$  gauge group structure but also higher-order calculations in QCD and partially the Higgs sector can be tested.

### 2.3 Event Generation and Available Computer Programs

The central part of the prediction of the diboson production cross sections at the LHC is the calculation of the matrix element of the hard scattering process as introduced in Sect. 2. The integration over the full phase space in Eqn. 2.6 including spin- and color-effects is a complicated task, and can be only achieved with Monte Carlo (MC) sampling methods that are implemented in MC event generators.

The connection of hard scattering processes at high energy scales to the partons within the proton at low scales is described by parton shower models. The basic idea of these models is to relate the partons from the hard interaction at  $Q^2 \gg \Lambda_{QCD}^2$  to partons near the energy scale of  $\Lambda_{QCD}$  via an all-order approximation in the soft and collinear regions. The commonly used approach is the leading-log approximation, where parton showers are modeled as a sequence of the splitting of a mother parton to two daughter partons. The implementation of parton showers is achieved with MC techniques. A detailed discussion of these models can be found elsewhere [32]. Phenomenological models have to be applied at the scale  $\Lambda_{QCD}$  to describe the process of hadronization, i.e. a description for the formation of hadrons from final state partons, such as the Lund string model [33] and the cluster model [34, 35].

Multiple purpose event generators include the following aspects of  $pp$  collisions: the description of the proton via an interface to PDF sets; initial state parton shower models; hard scattering processes and the subsequent decay of unstable particles; and the simulation of the final state parton shower and hadronization.

The commonly used event generators in the relevant analyses of this review article are PYTHIA [36], PYTHIA8 [37], HERWIG [38], HERWIG++ [39] and SHERPA [40]. All generators contain an extensive list of SM and BSM processes, calculated with LO matrix elements. Higher-order corrections are also available for some important processes. Several programs such as MADGRAPH [41], MCFM [42], ALPGEN [43] and BLACKHAT-SHERPA [44]

calculate matrix elements for LO and NLO processes, but do not provide a full event generation with parton showers and hadronization effects. The subsequent event generation starting from the final state parton configuration is often performed by the HERWIG and SHERPA libraries.

Since the matrix element calculations give not only a good description of the hard emission of jets in the final states, but also handle interferences of initial and final states correctly, it is desirable to combine matrix element calculations and parton showers. This combination is complicated by the fact that the phase space of NLO matrix element calculation partially overlaps with parton shower approaches. Several matching schemes have been suggested to provide a combination methodology of LO matrix element calculations for different parton multiplicities and parton shower models. These schemes avoid double counting of final state particles by reweighting techniques and veto-algorithms. The Mangano (MLM) scheme [45] and the Catani-Krauss-Kuler-Webber (CKKW) matching scheme [46] [47] are widely used for tree-level generators.

Matching schemes can only be applied for LO calculations, while the matching between parton showers and NLO matrix element calculations is more sophisticated and advanced methods have to be used. The MC@NLO approach [48] was the first prescription to match NLO matrix elements to the parton shower framework of the HERWIG generator. The basic idea is to remove all terms of the NLO matrix element expression which are generated by the subsequent parton shower. The POWHEG procedure [49] which is implemented in the POWHEGBOX framework [50] was the second approach developed for NLO matrix element matching. The POWHEG procedure assumes that the highest energy emitted parton is generated first and then feed into the shower generators of the subsequent softer radiation. In contrast to the MC@NLO approach, only positive weights appear and in addition the procedure can be interfaced to other event generators besides HERWIG.

The matching in the SHERPA generator relies on the CKKW matching scheme for LO ME and on the POWHEG scheme for NLO calculation. PYTHIA8 also includes the possibility of matching NLO matrix elements via the POWHEG approach.

A crucial ingredient for all MC event generators is the knowledge of the proton PDF. The determination of the PDFs has been performed by several groups. The CTEQ [51], MRST [52] and NNPDF [53] collaborations include all available data for their fits but differ in the treatment of the parametrization assumptions of  $f_q(x, Q^2)$  in Eqn. 2.6. The HERAPDF [54] group bases their PDF fits on a subset of the available data, i.e. mainly on the deep inelastic scattering measurements from the HERA collider. The results presented in this review rely mainly on the CTEQ and MRST PDFs.

## 2.4 SM Predictions of Diboson Production Cross Sections

Table 1 summarizes LO and NLO predictions of the diboson production in  $pp$  collisions at  $\sqrt{s} = 7$  TeV based on the MCFM generator. The uncertainties due to scales and PDF variations are also shown. The difference between LO and NLO predictions varies up to 25% depending on the final state. The difference between different PDF sets is on the order of 3%.

The most recent NNLO predictions for  $ZZ$  suggests a further increase by 11% on the inclusive cross section [11]. However, electroweak effects are not yet taken into account, which will lead to a reduction of the cross section.

**Table 1.** LO and NLO predictions of diboson production cross sections at 7 TeV in  $pp$  collisions based on MCFM for different PDF sets. The uncertainties include the PDF, renormalization, and factorization scale uncertainties. These uncertainties are evaluated based on the variation of renormalization and factorization scales up and down by a factor of two and from the eigenvector error sets of the CT10 PDF set. The  $Z$  boson is defined by the given mass range.

Process	$Z$ boson cut [GeV]	LO MSTW2008	NLO MSTW2008	NLO CT10	Uncertainty CT10 + Scales
$\sigma(pp \rightarrow W^+W^- + X)$ [pb]	-	29.1	46.3	45.3	$^{+2.1}_{-1.9}$
$\sigma(pp \rightarrow W^+Z + X)$ [pb]	66 – 116	7.3	11.6	11.4	$^{+0.7}_{-0.6}$
$\sigma(pp \rightarrow W^-Z + X)$ [pb]	66 – 116	4.1	6.5	6.2	$^{+0.4}_{-0.4}$
$\sigma(pp \rightarrow W^\pm Z + X)$ [pb]	66 – 116	11.4	18.1	17.7	$^{+1.1}_{-1.0}$
$\sigma(pp \rightarrow W^\pm Z + X)$ [pb]	60 – 120	11.4	18.1	17.7	$^{+1.1}_{-1.0}$
$\sigma(pp \rightarrow ZZ + X)$ [pb]	66 – 116	8.8	12.3	12.1	$^{+xx}_{-xx}$
$\sigma(pp \rightarrow ZZ + X)$ [pb]	60 – 120	9.0	12.5	12.3	$^{+xx}_{-xx}$

## 2.5 Description of SM Extensions and aTGCs

Since this article focuses on the LHC results at  $\sqrt{s} = 7$  TeV, we restrict ourselves to the discussion of the triple gauge boson interaction vertices and their new physics modifications, commonly called aTGCs. There are only two triple gauge vertices allowed in the SM,  $WWV$  with  $V = Z, \gamma$ . The  $WWV$  vertices are fully determined by the  $SU(2)_L \times U(1)_Y$  gauge group structure. A generic anomalous contribution to the  $WWV$  vertex can be parametrized in terms of a purely phenomenological effective Lagrangian. The most general Lagrangian that describes the trilinear interaction of electroweak gauge bosons with the smallest number of degrees of freedom [55], [56], [57], reads as

$$\begin{aligned}
i\mathcal{L}_{WWV}/g_{WWV} = & [1 + \Delta g_V^1] V^\mu (W_{\mu\nu}^- W^{+\nu} - W_{\mu\nu}^+ W^{-\nu}) \\
& + [1 + \Delta \kappa_V] W_\mu^+ W_\nu^- V^{\mu\nu} \\
& + \frac{\lambda_V}{m_W^2} V^{\mu\nu} W_\nu^{+\alpha} W_{\alpha\mu}^- \\
& + ig_V^4 W_\mu^- W_\nu^+ (\partial^\mu V^\nu + \partial^\nu V^\mu) \\
& + ig_V^5 \epsilon_{\mu\nu\alpha\beta} [(\partial^\alpha W^{-\mu}) W^{+\nu} - W^{-\mu} (\partial^\alpha W^{+\nu})] V^\beta \\
& - \frac{\tilde{\kappa}_V}{2} W_\mu^- W_\nu^+ \epsilon^{\mu\nu\alpha\beta} V_{\alpha\beta} \\
& - \frac{\tilde{\lambda}_V}{2m_W^2} W_{\rho\nu}^- W_\nu^{+\mu} \epsilon^{\nu\rho\alpha\beta} V_{\alpha\beta},
\end{aligned} \tag{2.7}$$

where  $g_{WW\gamma} = -e$  and  $g_{WWZ} = -e \cot \theta_W$  are the two couplings,  $m_W$  is the mass of the  $W$  boson,  $V^\mu$ ,  $W^\mu$ ,  $W_{\mu\nu} = \delta_\mu W_\nu - \delta_\nu W_\mu$  and  $V_{\mu\nu} = \delta_\mu V_\nu - \delta_\nu V_\mu$  are the gauge boson vector

fields and their field tensors. The anomalous couplings are described by seven parameters for each of the  $WWV$  vertices,  $\Delta g_V^1$ ,  $\Delta \kappa_V$ ,  $\lambda_V$ ,  $g_V^4$ ,  $g_V^5$ ,  $\tilde{\kappa}_V$  and  $\tilde{\lambda}_V$ . All aTGCs are set to be zero in the SM.

The first three terms in Eqn. 2.7 are  $CP$ -invariant, while the remaining four terms violate the  $C$ - and/or  $P$ -symmetry. Furthermore, electromagnetic gauge invariance requires that  $\Delta g_\gamma^1 = g_\gamma^4 = g_\gamma^5 = 0$ , while the corresponding  $Z$  boson coupling parameters  $\Delta g_Z^1$ ,  $g_Z^4$  and  $g_Z^5$  can differ from their SM values. We are left with five independent  $C$ - and  $P$ -conserving parameters  $\Delta g_Z^1$ ,  $\Delta \kappa_\gamma$ ,  $\Delta \kappa_Z$ ,  $\lambda_\gamma$  and  $\lambda_Z$ , and six  $C$ - and/or  $P$ -violating parameters  $g_Z^4$ ,  $g_Z^5$ ,  $\tilde{\kappa}_\gamma$ ,  $\tilde{\kappa}_Z$ ,  $\tilde{\lambda}_\gamma$  and  $\tilde{\lambda}_Z$ . The studies presented in this paper assume gauge invariance and conservation of  $C$  and  $P$  separately, resulting in five independent aTGC parameters.

In order to further reduce the number of independent parameters and therefore allow for a simpler experimental derivation of limits, several additional assumptions can be made. The ‘equal coupling’ scenario assumes that the anomalous triple gauge couplings are the same for  $\gamma$  and  $Z$  bosons, i.e.,  $\kappa_Z = \kappa_\gamma$ ,  $\lambda_\gamma = \lambda_Z$  and  $\Delta g_Z^1 = 0$ , and hence leads to two free parameters. The ‘LEP’ scenario is motivated by the  $SU(2) \times U(1)$  gauge invariance [58] and assumes  $\Delta \kappa_\gamma = \cos^2 \theta_W (\Delta g_1^Z - \Delta \kappa_Z) / \sin^2 \theta_W$  and  $\lambda_Z = \lambda_\gamma$ , leading to three independent parameters. The ‘HISZ’ scenario [59] assumes no cancellations between tree-level and loop contributions, leading to the constraints,  $\Delta g_1^Z = \Delta \kappa_Z / (\cos^2 \theta_W - \sin^2 \theta)$ ,  $\Delta \kappa_\gamma = 2\Delta \kappa_Z \cos^2 \theta_W / (\cos^2 \theta - \sin^2 \theta_W)$ , and  $\lambda_Z = \lambda_\gamma$ , which leave two free parameters. A review of various parametrization scenarios for aTGCs can be found in [60].

Non-zero aTGCs will lead to a change in the calculation of matrix elements. As an example, we discuss here the change of the matrix element  $\Delta \mathcal{M}_{Z_H, W_H}$ , describing the production of the  $q\bar{q} \rightarrow WZ$  process for large center-of-mass energies  $\sqrt{s} \gg M_W$  of the interacting partons [56]. The two subscripts  $Z_H$  and  $W_H$  denote the helicity of the final state bosons (0, +, and -). The expected changes read as

$$\begin{aligned}\Delta \mathcal{M}_{\pm,0} &\sim \frac{\sqrt{\hat{s}}}{2m_W} [\Delta g_Z^1 + \Delta \kappa_Z + \lambda_Z] \frac{1}{2} (1 \mp \cos \theta_Z^*), \\ \Delta \mathcal{M}_{\pm,\pm} &\sim \frac{\hat{s}}{2m_W^2} [\lambda_Z] \frac{1}{\sqrt{2}} (\sin \theta_Z^*), \\ \Delta \mathcal{M}_{0,\pm} &\sim \frac{\sqrt{\hat{s}}}{2m_W} [2\Delta g_Z^1 + \lambda_Z] \frac{1}{2} (1 \pm \cos \theta_Z^*), \\ \Delta \mathcal{M}_{0,0} &\sim \frac{\hat{s}}{2m_W^2} [\Delta g_Z^1] \frac{1}{\sqrt{2}} (\sin \theta_Z^*),\end{aligned}$$

where  $\theta_Z^*$  denotes the production angle of the  $Z$  boson with respect to the incoming quark direction. In general, the matrix element  $\mathcal{M}$  and thus the production cross section increases with increasing center-of-mass energy of the interacting partons. The LHC allows for a larger sensitivity to the  $\lambda_Z$  and  $\Delta g_Z^1$  parameters as their contribution to the production cross section increases with the squared center-of-mass energy  $s$ . In addition, different aTGCs lead to different angular distributions of the final state particles. A multi-dimensional differential cross section measurement can constrain these parameters individually.

Even though the  $ZZV$  vertex is forbidden in the SM, new physics scenarios might allow for such interaction vertices. The corresponding phenomenological effective Lagrangian

**Table 2.** Summary of  $CP$ -conserving aTGC parameters and their relevant production processes.

Parameter	aTGC-Vertex	Sensitive Process
$\Delta g_Z^1$	$WWZ$	$q\bar{q} \rightarrow Z \rightarrow WW, q\bar{q}' \rightarrow W \rightarrow ZW$
$\Delta \kappa_Z$	$WWZ$	$q\bar{q} \rightarrow Z \rightarrow WW, q\bar{q}' \rightarrow W \rightarrow ZW$
$\Delta \kappa_\gamma$	$WW\gamma$	$q\bar{q} \rightarrow \gamma \rightarrow WW, q\bar{q}' \rightarrow W \rightarrow W\gamma$
$\lambda_Z$	$WWZ$	$q\bar{q} \rightarrow Z \rightarrow WW, q\bar{q}' \rightarrow W \rightarrow WZ$
$\lambda_\gamma$	$WW\gamma$	$q\bar{q} \rightarrow \gamma \rightarrow WW, q\bar{q}' \rightarrow W \rightarrow W\gamma$
$f_5^\gamma$	$ZZ\gamma$	$q\bar{q} \rightarrow \gamma \rightarrow ZZ$
$f_5^Z$	$ZZ\gamma$	$q\bar{q} \rightarrow \gamma \rightarrow ZZ$
$h_4^\gamma$	$Z\gamma\gamma$	$q\bar{q} \rightarrow \gamma \rightarrow Z\gamma$
$h_4^Z$	$Z\gamma\gamma$	$q\bar{q} \rightarrow \gamma \rightarrow Z\gamma$

reads as

$$i\mathcal{L}_{ZZV} = -\frac{e}{M_Z^2} [f_4^V ((\delta_\mu V^{\mu\beta}) Z_\alpha (\delta^\alpha Z_\beta)) + f_5^V ((\delta^\sigma V_{\sigma\mu}) \tilde{Z}^{\mu\beta} Z_\beta)], \quad (2.8)$$

where the anomalous on-shell  $ZZ$  production is parametrized by two  $CP$ -conserving ( $f_5^V$ ) and two  $CP$ -violating ( $f_4^V$ ) parameters. Similarly, the vertex  $ZV\gamma$  [61] can be described by an effective Lagrangian, where the anomalous couplings are described by  $h_3^Z$  and  $h_4^Z$  for the  $ZZ\gamma$  vertex, and  $h_3^\gamma$  and  $h_4^\gamma$  for the  $Z\gamma\gamma$  vertex. It should be noted that the parameters  $h_i^V$  and  $f_i^V$  are partly correlated. In contrast to the  $WWV$  vertex, the effective parameters for the  $ZZV$  and  $ZV\gamma$  vertices vanish at tree level in the SM and only higher-order corrections allow for small  $CP$ -conserving couplings in the order of  $10^{-4}$ .

An overview of the properties of all aTGC parameters is given in Table 2.

The unitarity of the SM electroweak Lagrangian is preserved due to gauge invariance. The introduction of aTGCs in the Lagrangian alters its gauge structure and can lead to unitarity violations at relatively low energies. This can be seen in Eqn. 2.8, where some matrix elements are proportional to the center-of-mass energy. To avoid unitarity violations at high energies, the Lagrangian approach in Eqn. 2.7 is replaced by a form factor as

$$\lambda_s = \frac{\lambda_0}{(1 + s/\Lambda^2)^n} \quad (2.9)$$

where  $\lambda_0$  is the aTGC parameter at low energies and  $\Lambda$  is the energy cut-off scale at which new physic effects become dominant [62]. By convention,  $n = 2$  is usually chosen. In some sense, the form factor can be interpreted by treating the couplings in the Lagrangian as energy dependent<sup>2</sup>.

The choice of the form factor parametrization and the cut-off scale  $\Lambda$  is arbitrary as long as it conserves unitarity for reasonably small aTGC coupling parameters. It is not important at  $e^+e^-$  colliders as the fixed center-of-mass energy of the interaction particles allows for a well-defined translation between different choices of parametrization. The situation is different for hadron colliders, where only the center-of-mass energy of the interacting protons is known, but not the energy of the interacting partons. The measured production cross

<sup>2</sup>Strictly speaking, the Lagrangian couplings must remain constant and these are actually two different approaches.

sections are always integrated over a certain energy range and their interpretation in terms of aTGCs depends on the form factors chosen.

The cut-off scale  $\Lambda$  is usually chosen such that the extracted limits on aTGCs still preserve unitarity within a given analysis. In order to give experimental limits that are free from the arbitrary choice of the form factor, the cut-off scale is also set to  $\Lambda = \infty$ , i.e. using a constant form factor and hence violating unitarity at high energies. However, the aTGC limits based on  $\Lambda = \infty$  are the more stringent and less conservative.

The introduction of the form factor is conceptually overly restrictive, since the only physics constraint is that the theory respects the unitarity bound in the region where there is data. A newly-proposed approach for the study of aTGCs is based on effective field theories [63]. An effective field theory of the SM can be written as

$$\mathcal{L}_{eff} = \mathcal{L}_{SM} + \sum_i \frac{c_i}{\Lambda^2} O_i + \dots$$

where  $O_i$  are dimension-six operators, and  $c_i$  are coupling parameters that describe the interaction strength of new physics with the SM fields. It can be shown [59] that only three dimension-six operators affect the electroweak gauge boson self-interaction. The corresponding coefficients  $c_i$  can be related to the aTGCs that are discussed above.

There are several advantages of using effective field theories for the description of aTGCs. By construction, an effective quantum field theory is only useful up to energies of the order  $\Lambda$ . As long as the effective theory describes data, it automatically respects the unitarity bound. Hence, no further assumptions on the energy scale  $\Lambda$  have to be applied. Furthermore, the effective field theory approach has fewer parameters and is renormalizable by construction. While the results on aTGC presented in this review article are based on the modified Lagrangian approach, future measurements might use effective field theories for aTGC studies.

### 3 Experimental Aspects of Diboson Measurements at the LHC

#### 3.1 The LHC machine

The LHC [64] is currently the world's most powerful particle accelerator. It consists of several stages that successively increase the energy of the protons (and heavy ions). Protons are accelerated by the LINAC to 50 MeV, the Proton Synchrotron Booster to 1.4 GeV, the Proton Synchrotron to 26 GeV, and Super Proton Synchrotron to 450 GeV) before the final injection into the LHC ring. With a circumference of 27 km and a magnetic field of 8.3 T, the LHC can accelerate each proton beam up to 7 TeV. With a revolution frequency of 11.25 kHz, and a maximum of 2808 bunches that can be filled with up to 115 billion protons per bunch, the instantaneous luminosity can reach  $10^{34} \text{ cm}^{-2}\text{s}^{-1}$  with a beam emittance of  $16 \mu\text{m}$ , providing a bunch collision rate of 40 MHz. The two proton beams are brought together and collide head-on in four points around the LHC ring, where four large detectors - ALICE, ATLAS, CMS and LHCb - are located.

First  $pp$  collisions at the LHC were carried out in November 2009 with a proton-proton center-of-mass energy of 0.9 TeV. The LHC started operations at a center-of-mass energy of

7 TeV in March 2010 and delivered an integrated luminosity of about  $50 \text{ pb}^{-1}$  in 2010 and  $5 \text{ fb}^{-1}$  in 2011 to both ATLAS and CMS experiments. The peak instantaneous luminosity delivered by the LHC at the start of a fill increased from  $2.0 \times 10^{32} \text{ cm}^{-2}\text{s}^{-1}$  in 2010 to  $3.6 \times 10^{33} \text{ cm}^{-2}\text{s}^{-1}$  by the end of 2011. The machine increased its center-of-mass energy to 8 TeV in 2012 and delivered  $25 \text{ fb}^{-1}$  to both experiments. The peaks instantaneous luminosity of  $7.7 \times 10^{33} \text{ cm}^{-2}\text{s}^{-1}$  was reached in November 2012. This is close to the design luminosity of  $10^{34} \text{ cm}^{-2}\text{s}^{-1}$ , albeit at twice the beam crossing time. The data analyses for the 2012 run are still ongoing, and this paper only covers results from the 7 TeV run in 2011. During this period, the maximum number of bunch pairs colliding was 1331, and the minimum bunching spacing was 50 ns with a typical bunch population of  $1.2 \times 10^{11}$  protons. The maximum number of inelastic interactions per bunch crossing ('pile-up') was 20, and the average was 9.1.

### 3.2 The ATLAS and CMS Detectors

Since the topologies of new physics processes are unknown, detectors should be designed to be sensitive to all detectable particles and signatures ( $e$ ,  $\mu$ ,  $\tau$ ,  $\nu$ ,  $\gamma$ , jets,  $b$ -quarks) produced in the interactions. Both ATLAS [65] and CMS [66] detectors are general-purpose detectors and are composed of many sub-detectors, each of which has a specific task in the reconstruction of the events. Although these two detectors differ in design and conception, the basic detection structure is similar. Both detectors have fast, multi-level trigger systems to select complex signatures online; fast data acquisition systems to record all selected events; excellent inner tracking detectors allowing efficient high- $p_T$  tracking and secondary vertex reconstruction; fine-grained, high-resolution electromagnetic calorimeters for electron and photon reconstruction; full coverage hadronic calorimetry for jet and missing transverse energy measurements; and high-precision muon systems with standalone tracking capability. The layouts of the ATLAS and CMS detectors are shown in Fig. 7. ATLAS emphasizes jet, missing transverse energy, and standalone muon measurements, while CMS has prioritized electron, photon, and inner tracking measurements.

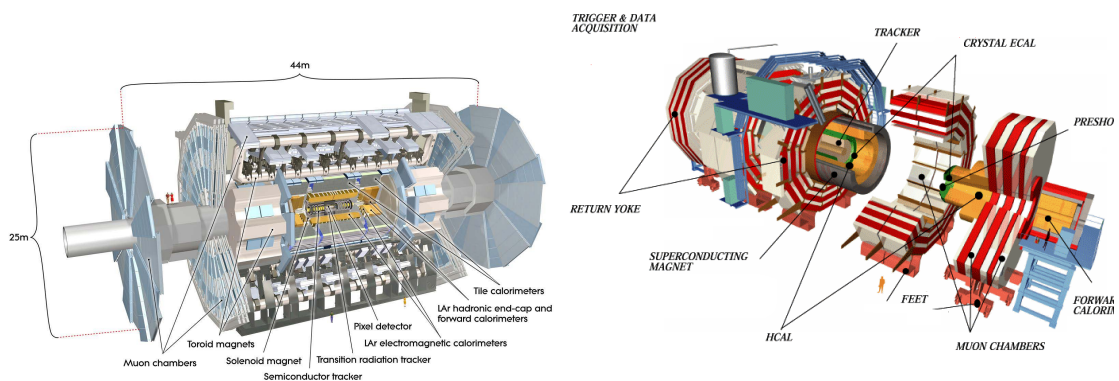


**Figure 7.** Layouts of the ATLAS (Left) and CMS (Right) detectors.

CMS has chosen to have a single huge solenoid immersing the inner tracker and elec-



tromagnetic and hadronic calorimeters inside a 4 T axial magnetic field. To reduce the occupancy of the inner tracking detector at the LHC design luminosity, the inner tracker consists solely of silicon pixel and microstrip detectors, which provide high granularity at all radii. CMS relies on the fine lateral granularity of its lead tungstate scintillating crystal electromagnetic calorimeter for electron and photon measurements. The hadronic sampling calorimeter system consists of brass absorbers and scintillating tiles readout via wavelength-shifting optical fibers guiding the light to photomultiplier tubes. The strong constraints imposed by the solenoid have resulted in a barrel hadronic calorimeter with insufficient absorption before the coil, so a tail catcher has been added around the coil to provide better protection against punch-through to the muon system. Driven by the design of the magnet, CMS relies on the high solenoidal field to bend muon tracks in the transverse plane, requiring the extrapolation of the track into the inner tracker.

ATLAS has chosen to have three different magnet systems: a thin solenoid around the inner tracking system, one eight-fold barrel and two eight-fold endcap air-core toroid magnets arranged radially around the hadron calorimeters. The inner tracker consist of silicon pixel and microstrip detectors at small radii and transition radiation tracker (TRT) at large radii. For electron and photon measurements, ATLAS relies on the fine segmentation along both the lateral and longitudinal directions of electromagnetic shower development using a lead and liquid-argon sampling technique. The hadronic calorimeter system uses a sampling technique similar to that used by CMS except iron and copper are used as absorbers. The structure of barrel and endcap toroid magnets allows standalone muon tracking inside the large area spanned by the toroids.

### 3.3 Reconstruction Objects for Physics Analysis

The  $z$ -axis of the coordinate system of both detectors is chosen to be along the beam-direction, the  $x$ -axis points to the center of the LHC, and the  $y$ -axis points upwards. The origin of the coordinate system is placed at the nominal collision point, i.e. in the center of the detectors. Two radial coordinates are used to describe event kinematics: the azimuthal angle  $\phi$  is defined in the  $xy$ -plane and the polar angle  $\theta$  is defined with respect to the  $z$ -axis. The polar angle is commonly used to define the pseudorapidity parameter  $\eta = -\log \tan \frac{\theta}{2}$ .

Observations of heavy diboson pair production processes at the LHC resulted from analyses of the fully leptonic (in which  $W$  decays to  $\ell\nu$  and  $Z$  bosons decay to  $\ell\ell$ , where  $\ell = e, \mu$ ) and semi-leptonic decay channels (in which one boson decays leptonically while the other boson decays to hadrons or neutrinos). The fully leptonic decay channels produce clean experimental signatures of one or more high- $p_T$  charged leptons and, in the case of  $W \rightarrow \ell\nu$ , large missing transverse energy  $E_T^{\text{miss}}$ . The semi-leptonic decay (or neutrino decay) channels result in the lepton+jets (or lepton+ $E_T^{\text{miss}}$ ) final states and are harder to detect experimentally due to the large  $V$ +jets background despite higher production cross sections.

The main analyses that are discussed in this review are based on the reconstruction of the electron and muon kinematics. Since the initial momenta of interacting partons in the plane transverse to the beamline is zero, the projected momenta of reconstructed objects in this plane, called transverse momenta  $p_T$ , are from special importance in event



reconstruction. Similar concept is introduced for measured energies, where the transverse energy is defined as  $E_T = E \sin \theta$ .

The data analyzed were often selected online by a single lepton ( $e$  or  $\mu$ ) or dilepton trigger with a threshold on the transverse energy in the electron case and on the transverse momentum in the muon case. Different thresholds (normally around 20 GeV for single lepton triggers and around 12 GeV for dilepton triggers) were applied depending on the average instantaneous luminosity of running periods.

The reconstruction of electrons combines electromagnetic calorimeter and inner tracker information [67, 68] and makes use of standard electron reconstruction algorithms at ATLAS and CMS. Candidate electrons are required to pass certain  $p_T$  ( $E_T$ ) threshold cuts and to be located inside the detector fiducial regions. Additional electron identification requirements are imposed which rely on electromagnetic shower shape observables, on associated track quality variables and on track-cluster matching observables, so as to preserve the highest possible efficiency while reducing the multijet background [69–71]. The  $\eta$ -coverage of the electron and photon candidate reconstruction is  $|\eta| < 2.37$  and  $|\eta| < 2.5$  for ATLAS and CMS, respectively. The regions  $1.37 < |\eta| < 1.52$  in ATLAS and  $1.44 < |\eta| < 1.57$  in CMS are typically excluded for most analyses, as they contain a significant amount of service infrastructure which reduces the reconstruction quality.

The reconstruction of photon candidates is similar to the electron case. However, specific cuts are applied on the shower-shape of the reconstructed electromagnetic clusters and on tracking information. If no track can be associated to the electromagnetic cluster, then the photon is called ‘unconverted’. An association of two tracks to the electromagnetic cluster imply a previous photon conversion into  $e^+e^-$  and therefore the corresponding photon candidates are labeled ‘converted’ photons.

Muon  $p_T$  is reconstructed using hits collected in both the inner tracker and the outer muon spectrometer and corrected for energy loss measured by the calorimeter. Good quality reconstruction is ensured by requiring a minimum number of hits associated with the track from both inner and outer tracking systems. Due to limited pseudorapidity coverage of the inner tracker and trigger detectors, muon candidates are reconstructed within  $|\eta| < 2.4$  for CMS and  $|\eta| < 2.7$  for ATLAS. However, the ATLAS inner detector only covers a region up to  $|\eta| < 2.5$  and therefore most analyses using reconstructed muons limit themselves also to  $|\eta| < 2.5$  in order to have combined muon candidates, i.e. tracks which are reconstructed in the inner detector and the muon spectrometer [72, 73].

To ensure candidate electrons and muons originate from the primary interaction vertex, some analyses required these lepton candidates to have small longitudinal and transverse impact parameters. These requirements reduce contamination from heavy flavor quark decays and cosmic rays. Leptons from heavy boson decays tend to be isolated from other particles in the event, while fake leptons or leptons from heavy quark decays will usually be close to a jet. To suppress the contribution from hadronic jets which are misidentified as leptons, electron and muon candidates are often required to be isolated in the inner tracker and (or) the electromagnetic calorimeter. Certain cuts are made on the sum of transverse energies of all clusters around the lepton or the sum of the  $p_T$  of all tracks that originate from the primary vertex and are within a certain cone around the lepton candidate. A

typical cone-size  $\Delta R = \sqrt{(\Delta\eta)^2 + (\Delta\phi)^2}$  is 0.3 in the  $(\eta, \phi)$ -plane. For the CMS case, a relative isolation variable combining the tracker and calorimeter isolation information is used.

Jets are reconstructed from topological clusters of energy in the calorimeter using the anti- $k_T$  algorithm with a certain radius parameter [74]. Jet energies are often calibrated using  $p_T$ - and  $\eta$ -dependent correction factors derived from studies based on the GEANT4 simulation [75], dijet,  $\gamma$ +jets, and  $Z$ +jets collision data. Jets are classified as originating from  $b$ -quarks by using algorithms that combine information about the impact parameter significance of tracks in a jet which has a topology of semileptonic  $b$ - or  $c$ -hadron decays. ATLAS and CMS reconstruct particle jets within regions of  $|\eta| < 4.9$  and  $|\eta| < 5.0$ , respectively [76, 77].

A summary of the identification and reconstruction features for electrons, muons, and jets of the ATLAS and CMS experiment is given in Tab. 3. The given kinematic constraints are also the basis for event selections that are discussed in the following chapters.

**Table 3.** Summary of electron, muon and jet reconstruction in the ATLAS and CMS detectors.

	ATLAS	CMS
Electron	Combination of inner tracker and calorimeter Shower shape cuts on calorimeter cluster 'loose', 'medium', 'tight' identification qualities $0 <  \eta  < 1.37$ and $1.52 <  \eta  < 2.37$ forward electrons: $2.37 <  \eta  < 4.9$ (w/o tracker)	'loose', 'tight' identification qualities $0 <  \eta  < 1.44$ and $1.57 <  \eta  < 2.5$
Muon	Combination of inner tracker and muon system combined muons up to $ \eta  < 2.5$ muon system coverage up to $ \eta  < 2.7$ muon trigger available up to $ \eta  < 2.4$	combined muons up to $ \eta  < 2.4$ muon system coverage up to $ \eta  < 2.4$
Jets	Anti- $k_T$ algorithm with $\Delta R = 0.4$ based on calorimeter information coverage up to $ \eta  < 4.9$	Anti- $k_T$ algorithm with $\Delta R = 0.5$ based on particle flow algorithm coverage up to $ \eta  < 5.0$

Weakly interacting particles such as neutrinos leave the detector unseen and can be only reconstructed indirectly. The concept of this indirect measurement is based on the fact that the momentum in the transverse plane before the  $pp$  collision is zero. Undetected energy and momentum carried out of the detector will therefore lead to a missing transverse energy,  $E_T^{\text{miss}} = |\vec{E}_T^{\text{miss}}|$ , in an event. The two-dimensional vector of  $E_T^{\text{miss}}$  is based on the calorimeter information and is calculated as the negative vector sum of the transverse energies deposited in the calorimeter towers. The latter is corrected for the under-measurement of the hadronic energy in the calorimeters and muon tracks reconstructed by the inner tracker and the muon spectrometer, leading to the following schematic definition:

$$\vec{E}_T^{\text{miss}} = - \sum_i \vec{E}_{T,i}^{\text{calo}} - \sum_i \vec{p}_{T,i}^{\mu} \quad (3.1)$$

For the traditional calorimeter-based algorithm, the correction for the under-measurement of the hadronic energy in the calorimeter is performed by replacing energies deposited by

reconstructed jets with those of the jet energy scale corrected jets. A different track-based algorithm to correct for the under-measurement of the hadronic energy in the calorimeter was also developed by both experiments. In this algorithm, the transverse momentum of each reconstructed charged particle track is added to the total missing transverse momentum, from which the corresponding transverse energy expected to be deposited in the calorimeters is subtracted.

At both ATLAS and CMS, tau reconstruction and identification concentrates on the tau hadronic decay modes which are characterized by either one or three charged pions accompanied by neutral pions [78, 79]. They are classified according to the number of reconstructed charged decay particles (prongs). Several sophisticated tau identification algorithms have been developed by both collaborations using different sets of identification variables such as tracking and calorimeter information to find the optimal set of cuts in a multi-dimensional phase space.

Detailed simulations of the ATLAS and CMS detector response have been developed over the recent years. Both simulations are based on the GEANT4 package, which describes the interactions of all final state particles with the detectors at a microscopic level. In a second step, the digitization of the simulated detector interactions is performed and the nominal data reconstruction algorithms are applied.

Despite of the great detail of the simulation software, several differences between data and MC predictions remain. To improve the agreement between data and MC simulations, several quantities such as reconstruction efficiencies or energy scales are measured independently in data and simulation. Correction factors are then determined and applied to the simulations to account for the observed differences.

### 3.4 Methodology of Cross-Section Measurements at the LHC

For the measurement of the diboson production at the LHC, it is generally assumed that both bosons are on-shell. Three different modes can be considered in the decay of heavy diboson pairs: the full hadronic decay channel where both bosons decay into quarks; the semi-leptonic decay channel in which one boson decays into quarks and the other to leptons; and the leptonic decay channel where the final state contains four leptons. The hadronic decay modes of the vector bosons are hard to be distinguished in hadron colliders due to the overwhelmingly large cross-section of jet-induced background processes. The CMS collaboration has published a combined cross section measurement based on semi-leptonic decays in  $WW$  and  $WZ$  pairs where the  $W$  boson decays leptonically while the second boson decays hadronically [80]. However, the systematic and statistical uncertainties of this measurement are significantly larger than the results based on studies of the fully leptonic decay channel, which allows for a rather clean signal selection. Due to this precise signal selection and the fact that the branching ratios of vector bosons are well known, the fully leptonic decay channel is the best channel in which precision measurements of the production cross section of diboson pairs at the LHC can be performed.

The theoretical prediction and calculation of diboson production cross sections has been discussed in Sect. 2.2. On the experimental side, the inclusive production cross section can

be calculated via the following equation:

$$\sigma_{VV}^{incl} = \frac{N_s}{\epsilon \cdot BR \cdot \int \mathcal{L} dt}. \quad (3.2)$$

The number of signal events is determined as  $N_s = N_d - N_b$ , where  $N_d$  is the number of selected events in data, and  $N_b$  is the number of background events surviving the signal selection. The factor  $\epsilon$  gives the fraction of signal events which pass the signal selection criteria. In order to correct the inclusive cross section for the choice of a specific decay channel, the total value has to be corrected by the appropriate branching ratio BR. These ratios are known to high accuracy from the LEP experiments [81]. The last term in the denominator of Eqn. 3.2 is the integrated luminosity, i.e. a measure of the size of the data sample used.

The efficiency correction factor  $\epsilon$  is usually estimated from the fraction of signal MC events passing all cuts through the full detector simulation. It should be noted that certain requirements on the final states can be applied directly at the generator level, for example, final state leptons may have to pass some minimal  $p_T$  cut. The factor  $\epsilon$  is thus defined as the ratio of all events which pass the signal selection at the reconstruction level over the number of all generated events. However, the simulation usually exhibits some differences compared to the real detector. These differences are corrected in the estimation of  $\epsilon$ , following the methods described in Sect. 3.3.

The efficiency correction  $\epsilon$  can be decomposed as the product of a fiducial acceptance ( $A$ ) and a detector-induced correction factor ( $C$ ):  $\epsilon = A \cdot C$ . The fiducial acceptance, which is the ratio of the number of events which pass the geometric and kinematic cuts in the analysis at the generator level ( $N_{\text{gen.}}^{\text{selected}}$ ) over the total number of generated events in a simulated sample of signal process ( $N_{\text{gen.}}^{\text{all}}$ ). These selection cuts at the generator level usually require geometric and kinematic constraints close to the cuts applied on the reconstructed objects. The dominant uncertainties on the fiducial acceptance are the scale and PDF uncertainties.

The detector correction factor,  $C$ , is defined as the number of selected events in the simulated sample ( $N_{\text{reco.}}^{\text{selected}}$ ) over the number of events in the fiducial phase space at the generator level ( $N_{\text{gen.}}^{\text{selected}}$ ). Hence  $\epsilon$  can be written as

$$\epsilon = C \cdot A = \frac{N_{\text{reco.}}^{\text{selected}}}{N_{\text{gen.}}^{\text{selected}}} \cdot \frac{N_{\text{gen.}}^{\text{selected}}}{N_{\text{gen.}}^{\text{all}}} = \frac{N_{\text{reco.}}^{\text{selected}}}{N_{\text{gen.}}^{\text{all}}} \quad (3.3)$$

The separation of  $\epsilon$  into  $A$  and  $C$  allows a separation of theoretical and experimental uncertainties, assuming the definition of the fiducial volume at the generator level resembles to a good extent the signal selection cuts at the reconstruction level. The fiducial cross section is defined as

$$\sigma_{VV}^{fid.} = \frac{N_d - N_b}{C \cdot BR \cdot \int \mathcal{L} dt} = \sigma_{VV}^{incl.} \cdot A, \quad (3.4)$$

which allows a measurement only effected to a small extent by theoretical uncertainties. It can therefore be used to compare measurements to theoretical predictions which might become available at a later date.

The uncertainties associated with the detector correction parameter  $C$  are dominated by experimental sources, such as limited knowledge of reconstruction or cut efficiencies and the accuracy of the energy/momentum measurements. In principle, this parameter can be larger than unity due to events outside of the fiducial region at the generator level which may migrate to the fiducial region defined at the reconstruction level. However, in practice this is usually not the case, as detector inefficiency and quality criteria on reconstructed objects have to be considered.

Equation 3.4 can be interpreted as the removal of all experimental effects due to detector acceptance, efficiencies, and resolutions from an experimental quantity to make it comparable to the theoretical prediction. Within this fiducial region, the distributions of variables can be unfolded, e.g. the transverse momenta of leptons in the final state. These distributions provide a differential cross section measurement and allow a full shape comparison with theoretical predictions.

The so-called ‘bin-by-bin’ unfolding method can be used if the purity of the underlying distribution is high, typically above 90%. This method is equivalent to calculating the cross section for each bin using Eqn. 3.4. The purity of one bin is defined as the ratio of events which have been reconstructed in the same bin as they have been generated in to the number of events generated in the chosen bin. For lower purities, advanced unfolding methods have to be used. One commonly used approach in diboson studies at the LHC is the Bayesian unfolding [82] which takes into account bin migration effects and reduces the impact of the underlying theoretical distribution which is used as input information.

## 4 Studies of the $WW$ , $WZ$ and $W\gamma$ final states

The production of  $W^+W^-$ ,  $W^\pm Z$  and  $W^\pm\gamma$  final states can occur via  $s$ -channel processes in the SM and therefore provide a test of the  $WWV$  vertex (with  $V = Z, \gamma$ ). In the following sections we describe in detail the event selection, the background estimation methods, and results of both experiments for the production cross section measurements of the  $W^+W^-$ ,  $W^\pm Z$  and  $W^\pm\gamma$  final states. In particular, we will highlight the differences in the published analyses and derive combinations of the measured cross sections.

### 4.1 WW Analysis

ATLAS and CMS have published analyses of the  $WW$  boson production based on the full available dataset at  $\sqrt{s} = 7$  TeV [83, 84]. Both analysis are based on final states in which both  $W$  bosons decay leptonically  $W^\pm \rightarrow \ell^\pm\nu$  with  $\ell = e, \mu$ . We discuss and compare these two measurements in the following sections.

#### 4.1.1 Event Selection

The experimental signature of the  $WW$  production in the leptonic decay channel is two high energetic leptons with no distinct invariant mass peak, together with a significant missing transverse momentum due to the presence of two neutrinos in the final state. Since two different-flavor leptons appear in the final state, three decay channels are studied, namely  $ee$ ,  $e\mu$  and  $\mu\mu$ . The  $\tau$ -decays of the  $W$  bosons are not directly taken into account due to

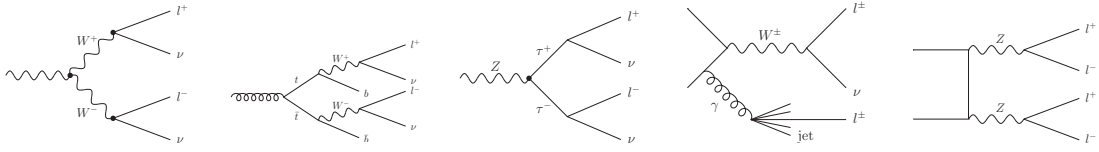


**Figure 8.**  $WW$  production in the  $s$ -channel in its leptonic decay mode and background processes ( $t\bar{t}$ ,  $Z \rightarrow \tau\tau$ ,  $W + jets$  and diboson  $ZZ$  production).

the relatively low  $\tau$ -reconstruction efficiency and significant fake rate. However, the cascade decay of the  $W$  boson via  $W \rightarrow \tau\nu \rightarrow \ell\nu\nu\nu$  is considered as signal.

The dominant SM background processes are the Drell-Yan process ( $Z/\gamma^* \rightarrow \ell^+\ell^-$ ), the top-pair production, the production of  $W$  bosons in association with jets where one jet is incorrectly identified as a signal lepton, and other diboson processes. The relevant Feynman diagrams are shown in Fig. 8.

The Drell-Yan process  $Z/\gamma^* \rightarrow \ell^+\ell^-$  has two same-flavor opposite-charge leptons with an invariant mass peaks at the  $Z$  boson mass. A mis-measurement of the missing transverse energies of the two leptons can lead to a signal similar to the signal process. It should be noted that the  $e\mu$  signal region is affected by the Drell-Yan process via the  $\tau$ -decay channel which could also lead to an  $e\mu$  final state. The top-pair production and its subsequent leptonic decay  $t\bar{t} \rightarrow W^+bW^-b \rightarrow \ell^+b\nu\ell^-b\nu$  also leads to a signal-like signature. These events are always produced with at least two additional  $b$ -jets.  $W$  production in association with jets, if the  $W$  boson decays leptonically and one of the jets is falsely identified as a signal lepton, will also fake the signal process. The leptonic decays of other diboson processes such as  $WZ$  and  $ZZ$  are also considered as background processes, in the case that one or two leptons are not reconstructed and cause large missing transverse energy in the event.

The full signal selections of the ATLAS and CMS measurements are rather complex. Since the final results do not explicitly depend on the details of the signal selection, we discuss here only the basic concept of the signal selection and the reasoning behind it. A detailed discussion can be found in [83] and [84].

A schematic  $WW$  signal selection requires exactly two high energetic, oppositely-charged and isolated leptons (e.g.  $p_T > 20$  GeV) are reconstructed and a minimal missing transverse momentum in each event. Since the latter cut is intended to suppress the Drell-Yan background, the  $E_{T,Rel}^{miss}$  variable is used since it reduces the impact of mis-measured leptons or jets compared to the standard  $E_T^{miss}$  definition. The background events due to the top-pair production can be effectively rejected by vetoing events with additional jets. The ATLAS analysis vetoes events that contain a jet with  $p_T > 25$  GeV, while CMS vetoes events with jets above 30 GeV. CMS imposes additional vetoes from two top-quark tagging techniques. It should be noted that the jet-veto criteria also rejects a significant fraction of  $WW$  events which are predicted by NLO QCD corrections. A summary of the detailed selection cuts is given in Tab. 4.

The resulting signal and background predictions compared to the yield in data, where

**Table 4.** Summary of  $WW$  selection requirements for the ATLAS and CMS experiments on the lepton transverse momentum  $p_T$ , the invariant mass ( $m_{\ell\ell}$ ) and transverse momentum ( $p_T(\ell\ell)$ ) of the dilepton system, and the relative transverse energy  $E_{T,Rel}^{\text{miss}}$  ( $N_{vtx}$  denotes the number of reconstructed vertices in the event). For ATLAS, these are also the basis for the definition of the fiducial phase-space region.

	ATLAS	CMS
$WW \rightarrow \ell\nu\ell'\nu$ ( $\ell, \ell' = e, \mu$ )	2 leptons with $p_T > 20$ GeV $ \eta^\mu  < 2.5,  \eta^e  < 2.47$ Dilepton $p_T(\ell\ell) > 30$ GeV No jet with $p_T > 25$ GeV and rapidity $Y < 4.5$	2 leptons with $p_T > 20$ GeV $ \eta^\mu  < 2.5,  \eta^e  < 2.47$ Dilepton $p_T(\ell\ell) > 45$ GeV No jet with $p_T > 30$ GeV and rapidity $Y < 4.5$
$WW \rightarrow \ell\nu\ell\nu$	dilepton mass $m_{\ell\ell} > 15$ GeV  Z boson veto $ m_{\ell\ell} - m_Z  > 15$ GeV $E_{T,Rel}^{\text{miss}} > 45$ GeV	di-electron mass $m_{ee} > 15$ GeV di-muon mass $m_{\mu\mu} > 12$ GeV Z boson veto $ m_{\ell\ell} - m_Z  > 15$ GeV $E_T^{\text{miss}} > (37 + 0.5 \cdot N_{vtx})$ GeV
$WW \rightarrow e\nu\mu\nu$	dilepton invariant mass $m_{e\mu} > 10$ GeV $E_{T,Rel}^{\text{miss}} > 25$ GeV	dilepton invariant mass $m_{e\mu} > 12$ GeV $E_T^{\text{miss}} > 20$ GeV

the SM prediction of the  $W^+W^-$  cross-section is used, are shown in Tab. 5. ATLAS expects 12%, 23% and 65% of signal events in the  $ee$ ,  $\mu\mu$  and  $e\mu$  channels, respectively. CMS has not published number for each individual channel in [84]. However, previous studies based on a smaller integrated luminosity [85], suggest very similar numbers. The final results are dominated by the contribution from the  $e\mu$  channel, as the corresponding selection cuts are relaxed due to the reduced background from the Drell-Yan process.

**Table 5.** Event yields for ATLAS and CMS for different decay channels. Signal and background estimates are also given.

Experiment	ATLAS				CMS
	$ee$	$\mu\mu$	$e\mu$	Combined	Combined
Data	174	330	821	1325	1134
$WW$ (MC)	$100 \pm 9$	$186 \pm 15$	$538 \pm 45$	$824 \pm 4 \pm 69$	$751 \pm 4 \pm 55$
Top	$22 \pm 12$	$32 \pm 15$	$87 \pm 26$	$141 \pm 30 \pm 22$	$129 \pm 13 \pm 20$
$W$ +jets	$21 \pm 11$	$7 \pm 3$	$70 \pm 31$	$98 \pm 2 \pm 43$	$60 \pm 4 \pm 21$
Drell-Yan	$12 \pm 4$	$34 \pm 12$	$5 \pm 2$	$51 \pm 7 \pm 12$	$11 \pm 5 \pm 3$
Other DiBosons	$13 \pm 2$	$21 \pm 2$	$44 \pm 6$	$78 \pm 2 \pm 10$	$48 \pm 3 \pm 5$
Total Background	$68 \pm 18$	$94 \pm 13$	$206 \pm 42$	$369 \pm 31 \pm 53$	$247 \pm 15 \pm 30$
Total Expected	$169 \pm 20$	$280 \pm 25$	$744 \pm 61$	$1192 \pm 31 \pm 87$	$1044 \pm 15 \pm 62$

#### 4.1.2 Background Estimation

The expected background contributions are summarized in Tab. 5. The dominant background contributions come from top-pair and  $W$ +jets events, which will be discussed in more detail in this section.



The background contribution due to top-quark pairs is estimated in both analysis with a data-driven method. ATLAS defines a data sample, named extended signal region (ESR), including all events which pass the signal selection cuts but without the jet-veto requirement. This sample is dominated by events from  $t\bar{t}$  and single top processes with more than one jet in each event. A control region is defined by applying the full signal selection criteria except requiring at least one  $b$ -tagged jet with  $p_T > 20$  GeV. The expected jet multiplicity distribution in the ESR is estimated from the measured control region distribution, and extrapolated to the ESR using MC predictions. The expected jet-multiplicity distribution in the ESR is fitted to the measured ESR in the higher jet-multiplicity region and the nominal value in the 0-jets bin taken as background estimate. The dominating uncertainty of this approach is due to the limited statistics in the control region.

CMS also defines a control region dominated by top-quark background events by requiring that a positive top-quark identification algorithm tags the given event. The normalization of the top-quark background is estimated via  $N^{top}(\text{not-tagged}) = N^{top}(\text{tagged}) \times (1 - \epsilon_{tt})/\epsilon_{tt}$ , where  $\epsilon_{tt}$  is the efficiency to tag a  $t\bar{t}$  event. This efficiency is estimated in a data sample selected by the nominal signal selection criteria but requiring one jet with  $p_T > 30$  GeV. The dominant uncertainty in the estimation of  $N^{top}(\text{not-tagged})$  is due to statistical and systematic uncertainties on  $\epsilon_{tt}$ .

Since the probability for a jet to be misidentified as an isolated lepton might not be modeled correctly in the MC simulations, a similar data-driven method has been used in both experiments for the  $W$ +jets background estimation. A  $W$ +jets enriched sample is selected by loosening the isolation or identification requirements on one lepton. The number of  $W$ +jet events in the signal region is then estimated via fake-factor  $f$ , which is defined as the ratio of the probability of a jet passing the nominal lepton selection over the probability of passing the loosened selection. The factor  $f$  is determined in data for muons and electrons, separately, using QCD multijet events.

The Drell-Yan background in both the  $ee$  and  $\mu\mu$  channels is estimated by inverting the  $Z$  boson veto cuts and then extrapolating from this control region into the signal region. The remaining background contributions are estimated with MC simulations, where all theoretical and experimental uncertainties have been taken into account.

The resulting distributions for the selected  $WW$  candidate events are shown in Figs. 9 and 10 for ATLAS and CMS, respectively. The expected  $WW$  signal contribution is based on MC expectations with MC@NLO used by ATLAS and MADGRAPH used by CMS.

### 4.1.3 Cross Section Measurement

The ATLAS cross section measurement is performed in each of the three decay channels and then combined, while CMS does not distinguish between the final states and directly derives a combined cross section. Furthermore, ATLAS defines a fiducial volume and separates the signal selection efficiency in acceptance and detector effects. The corresponding parameters  $\epsilon_{WW}$ ,  $A_{WW}$  and  $C_{WW}$  are shown in Tab. 6.

The efficiency factor  $\epsilon$  of the CMS analysis averages over all lepton flavors and is defined with respect to a phase space that includes all possible leptonic decay modes. The correction factor BR due to the branching ratio in Eqn. 3.2 is therefore given by



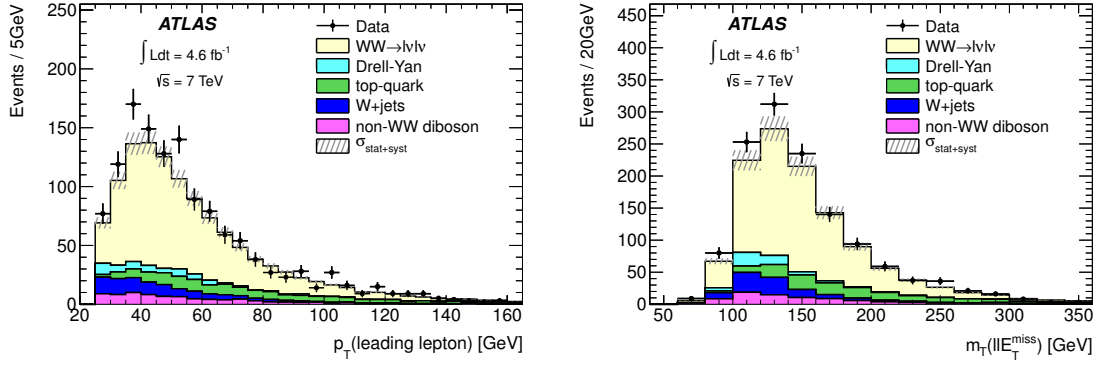


**Figure 9.** ATLAS: Leading lepton  $p_T$  (left) and  $m_T$  (right) distributions of the dilepton  $E_T^{\text{miss}}$  system for  $WW$  candidates with all selection criteria applied and combining  $ee$ ,  $\mu\mu$  and  $e\mu$  channels. The points represent data. The statistical and systematic uncertainties are shown as grey bands. The stacked histograms are from MC predictions except the background contributions from the Drell-Yan, top-quark and  $W$ +jets processes, which are obtained from data-driven methods. The prediction of the SM  $WW$  contribution is normalized to the inclusive theoretical cross section of 44.7 pb.

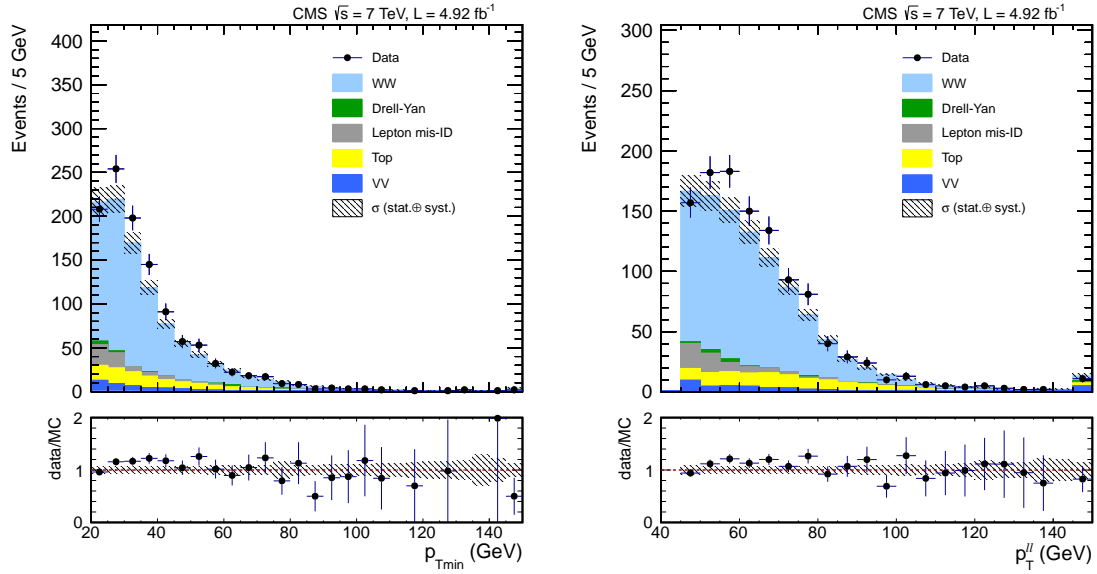


**Figure 10.** CMS:  $p_T$  of the leading lepton (left) and the invariant mass distribution of the dilepton system (right) at the  $WW$  selection level, reweighted to the data-driven estimates. All three channels ( $ee$ ,  $\mu\mu$  and  $e\mu$ ) are combined, and the uncertainty band corresponds to the statistical and systematic uncertainties on the predicted yield.

$\text{BR} = [3 \cdot \text{BR}(W \rightarrow \ell\nu)]^2$ . The efficiency correction factor  $\epsilon$  in the ATLAS analysis is defined for each decay channel with respect to a phase space that includes only the respective final states. The contributions from the cascade decay  $WW \rightarrow \tau\nu\ell\nu \rightarrow \ell'\nu\nu\ell\nu$  and  $WW \rightarrow \tau\nu\tau\nu \rightarrow \ell\nu\nu\ell'\nu\nu$  are also included.

Experimental uncertainties in Tab. 6 are dominated by lepton reconstruction efficien-

**Table 6.** Selection efficiencies and acceptance factors for ATLAS and CMS including their respective uncertainties.

Experiment	ATLAS			CMS
Channel	$ee$	$\mu\mu$	$e\mu$	combined
$A_{WW}$	$(7.5 \pm 0.4)\%$	$(8.1 \pm 0.5)\%$	$(15.9 \pm 0.9)\%$	-
$C_{WW}$	$(40.3 \pm 1.8)\%$	$(68.7 \pm 2.1)\%$	$(50.5 \pm 1.6)\%$	-
$A_{WW} \times C_{WW}$	$(3.0 \pm 0.1)\%$	$(5.6 \pm 0.2)\%$	$(8.0 \pm 0.3)\%$	$(3.28 \pm 0.26)\%$
Stat. Unc.	1.2%	0.7%	0.4%	0.6%
Detector.Unc.	3.1%	1.3%	1.6%	4.9%
Theo.Unc.	1.0%	1.0%	1.0%	2.7%
Jet.Veto Unc.	3.7%	3.7%	3.7%	4.7%
Combined Unc.	4.9%	4.0%	4.1%	7.3%

cies and energy/momentum scale uncertainties. Theoretical uncertainties are significantly different in both analyses even though the signal selection requirements are similar. Theoretical uncertainties contain contributions from the uncertainties on strong coupling constant ( $\alpha_s$ ), renormalization ( $\mu_r$ ) and factorization ( $\mu_f$ ) scales, and PDFs. The two scales are varied in the range of  $\mu_0/2$  and  $2\mu_0$  ( $\mu_0 = \mu_r = \mu_f$ ) to estimate the uncertainty. ATLAS chose to use  $\mu_0 = m_{WW}$  while CMS chose to use  $\mu_0 = m_W$ . A second and more significant difference comes from the fact that CMS calculates the above theoretical uncertainties with the jet-veto scale factor applied, while ATLAS estimates the theoretical uncertainties before applying the jet-veto requirement.

Hence the estimation of the jet-veto scale factor needs to be discussed in more detail. Both analyses use a data-driven approach to estimate the probability ( $P_{WW}^{data}$ ) for a  $WW$  signal event failing the jet-veto requirement in data. This probability is calculated as

$$P_{WW}^{data} = \frac{P_{WW}^{MC}}{P_{Z/\gamma^*}^{MC}} \times P_{Z/\gamma^*}^{Data} \quad (4.1)$$

where  $P_{Z/\gamma^*}$  denotes the probability of  $Z/\gamma^*$  boson events to pass a jet-veto requirement. Events containing a  $Z/\gamma^*$  boson can be selected with a high purity in data and the kinematic distributions of jets are expected to be similar to those in  $WW$  events. Most uncertainties on the jet-veto requirement cancel in the ratio ( $P_{WW}^{MC}/P_{Z/\gamma^*}^{MC}$ ) and therefore a reduction on the uncertainty of  $P_{WW}^{data}$  is achieved. The cancellation in the ratio is also the reason why ATLAS chose to estimate the PDF and scale uncertainties on  $\epsilon$  before applying the jet-veto requirement. The overall uncertainty on the jet-veto requirement is significantly lower in ATLAS compared to that in the CMS analysis. Another possible contribution is that ATLAS estimates the effect of higher order corrections using MC@NLO, while CMS uses MCFM. Since MC@NLO includes parton shower effects in contrast to MCFM, a better description of the jets is expected which could lead to a smaller effects from higher order corrections.

It is worthwhile noting that the uncertainties of the jet-veto probability on  $A_{WW}$  are approximately 5.6% and therefore significantly larger than its impact on  $\epsilon_{WW}$ . This is mainly due to the fact that the method of Eqn. 4.1 cannot be applied directly at the

generator level. A naive estimate of the scale and PDF uncertainties on the jet-veto requirement leads to an underestimate of the corresponding uncertainty and therefore more sophisticated methods have to be applied [86].

**Table 7.** Summary of measured and predicted inclusive cross sections  $\sigma_{WW}$  for the  $WW$  process from the ATLAS and CMS collaborations.

Channel	Measured [pb]	Predicted [pb]
ATLAS		
$WW \rightarrow e\nu e\nu$	$46.9 \pm 5.7 (stat.) \pm 8.2 (sys.) \pm 1.8 (lumi.)$	$45.3 \pm 2.0$
$WW \rightarrow \mu\nu\mu\nu$	$56.7 \pm 4.5 (stat.) \pm 5.5 (sys.) \pm 2.2 (lumi.)$	$45.3 \pm 2.0$
$WW \rightarrow e\nu\mu\nu$	$51.1 \pm 2.4 (stat.) \pm 4.2 (sys.) \pm 2.0 (lumi.)$	$45.3 \pm 2.0$
$WW \rightarrow \ell\nu\ell'\nu$	$51.9 \pm 2.0 (stat.) \pm 3.9 (sys.) \pm 2.0 (lumi.)$	$45.3 \pm 2.0$
CMS		
$WW \rightarrow \ell\nu\ell'\nu$	$52.4 \pm 2.0 (stat.) \pm 4.5 (sys.) \pm 1.2 (lumi.)$	$45.3 \pm 2.0$

The cross section results from both experiments are summarized in Tab. 7. The cross section results from three individual channels are combined by minimizing a negative log-likelihood function, which depends on the expected number of signal events in each decay channel.

The measured inclusive cross sections agree within their uncertainties for both experiments. The overall uncertainty is dominated by the systematic uncertainty, which is 7.5% for ATLAS and 8.6% for CMS. The dominant uncertainty sources come from the top-quark background estimation (3.6% at ATLAS and 2.9% at CMS) and the jet-veto selection efficiency (3.6% at ATLAS and 4.7% at CMS).

CMS also published a measurement of the cross section ratio of  $\sigma_{WW}$  to  $\sigma_Z$ , where  $\sigma_Z$  is the  $Z$  boson inclusive production cross section measured in the  $ee$  and  $\mu\mu$  channels. The ratio measurement helps to reduce or cancel experimental uncertainties on the lepton identification efficiency and the integrated luminosity, as well as theoretical uncertainties on scales and PDFs. The latter is mainly due to the fact that the dominant production mechanism for both  $Z$ -boson and  $WW$ -pair is  $q\bar{q}$  annihilation. The measured cross section ratio is found to be

$$\sigma_{WW}/\sigma_Z = (1.79 \pm 0.16) \times 10^{-3}.$$

ATLAS published in addition a fiducial cross section in each decay channel. The fiducial volume of each decay channel reassembles the corresponding selection cuts used and hence leads to a rather complex definition and is also different for each decay channel. Hence, only individual results are available and no combination has been performed.

Within the defined fiducial phase space, ATLAS also provides a normalized unfolded distribution of the leading lepton  $p_T$  in the final state with all three channels combined. The unfolding procedure follows the iterative Bayesian method introduced in Sect. 3.4. The resulting distribution is shown in Fig. 11 and is compared to the MC@NLO prediction.

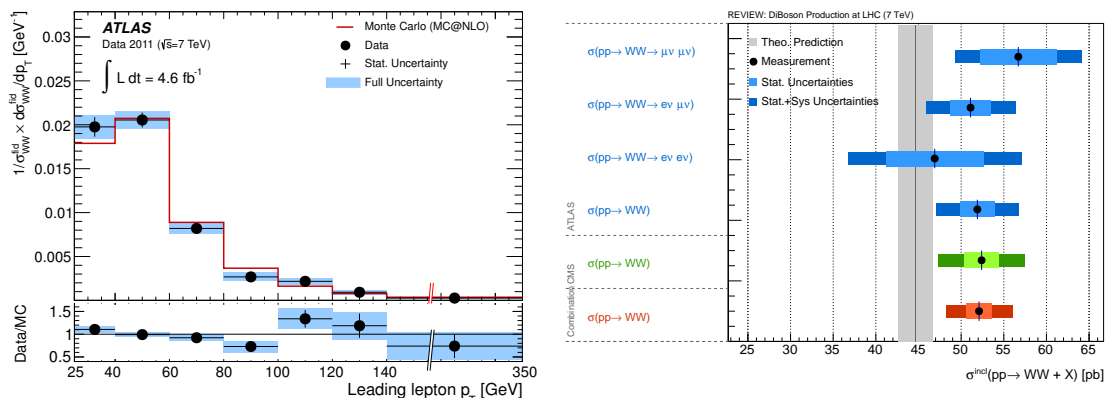


**Figure 11.** ATLAS: The normalized differential **Figure 12.** Summary of measured inclusive  $WW$  fiducial cross section as a function of the  $WW$  production cross-sections at  $\sqrt{s} = 7\text{TeV}$  leading lepton  $p_T$  compared to the SM prediction.

#### 4.1.4 Derived Results and Discussion

We first combine the measurements of the inclusive  $WW$  cross section for ATLAS and CMS at 7 TeV. For this, we assume that the uncertainties on the integrated luminosity are fully correlated among two experiments. Theoretical uncertainties on the fiducial acceptance are also assumed to be fully correlated. Even though there are differences in the signal selection criteria, the main sources of theoretical uncertainties are similar and the methods for estimating their uncertainties are the same. In particular this holds to a large extent also for uncertainties on the jet-veto requirement, which is a large source of uncertainty. The remaining experimental uncertainties on the selection efficiency, signal acceptance, and background estimations are treated fully uncorrelated.

The combination procedure follows the BLUE method [87], leading to a combined measurement of the  $WW$  production cross section

$$\sigma_{WW} = 52.1 \pm 1.5(\text{stat.}) \pm 3.6(\text{syst.}) \text{ pb.}$$

When no correlations are assumed between theoretical and jet-veto uncertainties, the mean value stays unchanged, while the systematic uncertainty reduces to 3.4 pb. The NLO QCD calculation of the cross section is  $45.3 \pm 2.0$  pb (as shown in Tab. 1) and compatible at the  $1.6\sigma$ -level with the measured cross section. This deviation cannot be caused by a SM Higgs boson with a mass around 125 GeV decaying into  $W^+W^-$ , as already discussed. A summary of the measured inclusive cross sections and their combination is shown in Fig. 12.

The definition of the fiducial phase space in the ATLAS analysis is highly complex. Hence we provide here an extrapolation to a fiducial phase space region, which is significantly simpler but keeps the theoretical uncertainties due to the required extrapolations to a minimum. Our simplified fiducial phase space is defined only in the prompt  $e$  and  $\mu$  channels (events with  $e$  or  $\mu$  from the  $\tau$  decays are removed) via the following criteria: two

leptons with  $p_T > 20$  GeV and  $|\eta| < 2.5$ ,  $p_T(\nu\nu) > 25$  GeV,  $p_T(\ell\ell) > 30$  GeV and  $m_{\ell\ell} > 20$  GeV. The extrapolation factor from the ATLAS fiducial phase space to the simplified phase space is evaluated using MC@NLO and is found to be  $2.06 \pm 0.18$ . Uncertainties due to scales and PDFs are estimated along with the above prescription. The largest uncertainty is due to the unused jet-veto criteria. This leads to a simplified fiducial cross section of  $\sigma_{WW}^{fid,simp} = 0.81 \pm 0.03(\text{stat.}) \pm 0.09(\text{syst.})$  pb.

Within this simplified fiducial phase space, one can also calculate the production cross section for  $WW$  events with the leading lepton  $p_T$  between 140 GeV and 180 GeV based on the unfolded results of the ATLAS experiment. The cross section we obtained is  $\sigma_{WW}^{fid,sim}(140 \text{ GeV} < p_T^{\text{leading lepton}} < 350 \text{ GeV}) = 24 \pm 10$  fb. This fiducial cross section is sensitive to the  $s$ -channel production of the  $WW$  process and can therefore be used to make constraints on aTGC parameters without any further experimental information.

## 4.2 WZ Analysis

ATLAS has published results on the  $WZ$  production using the full  $\sqrt{s} = 7$  TeV dataset [88], while only preliminary CMS results are available at this point [89]. Similar to the  $WW$  analysis, only final states involving muons and/or electrons are considered.

### 4.2.1 Event Selection

The process  $W^\pm Z \rightarrow \ell^\pm \nu \ell'^+ \ell'^-$  with  $\ell = e, \mu$  is characterized by three highly energetic and isolated leptons of which at least two have the same flavor and opposite charge with an invariant mass close to the  $Z$  boson pole mass. In addition a significant amount of  $E_T^{\text{miss}}$  is expected due to the escaping neutrino from the  $W$  boson decay. The possible final states are therefore  $e^+e^-e^\pm\nu$ ,  $e^+e^-\mu^\pm\nu$ ,  $\mu^+\mu^-e^\pm\nu$  and  $\mu^+\mu^-\mu^\pm\nu$ . The contribution of secondary  $\tau \rightarrow \ell\nu\nu$  decays of one or both bosons in  $WZ$  events is also regarded as signal.

SM background processes which lead to similar signatures in the detector are  $Z$ +jets,  $ZZ$ ,  $Z\gamma$ ,  $t\bar{t}$  and  $t\bar{t} + W/Z$ . The dominate background comes from  $Z$  boson production in association with at least one jet which is incorrectly identified as a signal lepton. For  $t\bar{t}$  events, two real leptons are expected in the fully leptonic decay channel and an additional third reconstructed lepton can come from a mis-identified jet. It should be noted that the probability for a jet to be identified as a signal lepton in  $t\bar{t}$  events is significantly higher than the probability in  $Z$ +jets events, since at least two  $b$ -jets are in the final state that can decay into real muons. The  $t\bar{t}$  production in association with a vector boson, i.e.  $t\bar{t} + W/Z$ , can lead to three real leptons in the final state if the associated vector boson also decays leptonically. The full leptonic decay of the  $ZZ$  pair can mimic the signal if one lepton is not reconstructed or is outside the detector acceptance, resulting in missing transverse energy. The  $Z\gamma$  process can fake a  $WZ$  signature only in the  $eee$  and  $\mu\mu e$  channels as the photon can be falsely reconstructed as an isolated electron. LO Feynman diagrams for the signal and background processes are shown in Fig. 13.

The generic signal selection of ATLAS and CMS requires two isolated leptons whose invariant mass is close to the  $Z$  boson mass. This requirement strongly suppresses the background from top-quark pair events. A third isolated lepton is assumed to come from the  $W$  boson decay and is required to pass more stringent requirements on the identification

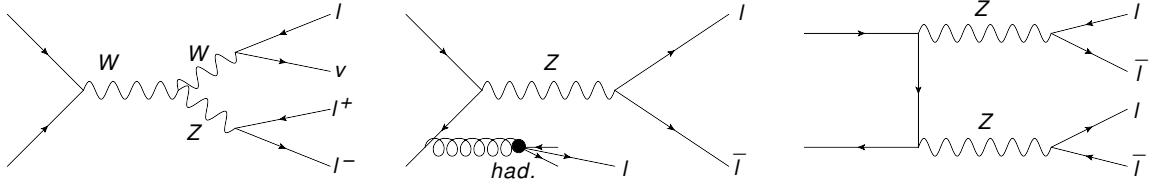


**Figure 13.** Feynman diagrams for  $s$ -channel signal processes (left) and primary background processes (middle:  $Z$ +jets, right:  $ZZ$ ) relevant for the  $WZ$  diboson analysis

quality and/or transverse momentum. The neutrino carries significant  $E_T^{\text{miss}}$  in the signal events and hence a minimal  $E_T^{\text{miss}}$  requirement is imposed. In addition, a cut on the transverse mass ( $M_T^W$ ) of the third lepton and the  $E_T^{\text{miss}}$  can be used to further reduce the background from  $Z$ +jets,  $Z\gamma$  and  $ZZ$  production. A summary of the detailed selections criteria used is given in Tab. 8.

**Table 8.** Summary of  $WZ$  selection requirements for the ATLAS and CMS experiment on the lepton transverse momenta  $p_T$  due to the  $W$  and  $Z$  bosons, the missing transverse energy  $E_T^{\text{miss}}$ , the invariant mass  $m_{\ell\ell}$  and  $p_T(\ell\ell)$  of  $Z$  boson candidate and the transverse mass of the  $W$  boson system. ATLAS requires also a minimal  $\Delta R$  distance between all leptons.

$WZ \rightarrow \ell^+ \ell^- \ell' \nu$ ( $\ell, \ell' = e, \mu$ )	$Z$ decay leptons $p_T > 15$ GeV $W$ decay lepton $p_T > 20$ GeV $ \eta^\ell  < 2.5$ $ m_Z - m_{\ell^+\ell^-}  < 10$ GeV $E_T^{\text{miss}} > 25$ GeV Minimal distance of leptons $\Delta R > 0.3$ $m_T > 20$ GeV of $W$ system	$Z$ decay leptons $p_T^{1,2} > 10, 20$ GeV $W$ decay lepton $p_T > 20$ GeV $ \eta^\ell  < 2.5$ $ m_Z - m_{\ell^+\ell^-}  < 20$ GeV $E_T^{\text{miss}} > 30$ GeV
--	---	---

The expected signal and backgrounds together with the observed data are shown in Tab. 9. ATLAS expects 17% of events in the  $eee$  channel, 23% in the  $ee\mu$  channel, 24% in the  $\mu\mu e$  channel, and 35% in the  $\mu\mu\mu$  channel. The increase in signal with decreasing number of electrons in the final state channels is due to the lower electron identification efficiency. A similar relationship is observed in the CMS analysis. It should be noted that the background expectation in the CMS analysis is significantly smaller compared to the ATLAS approach. This cannot be explained by kinematic cuts, but can be attributed to an enhanced fake-lepton rejection methodology of the CMS approach.

#### 4.2.2 Background Estimation

Because jets faking signal leptons may not be modeled correctly in MC the background contributions from  $Z$ +jets and  $t\bar{t}$  are estimated in a data-driven method in the ATLAS analysis. The basic idea of the  $Z$ +jets background estimate is a data-driven estimate of the probability,  $p_F$ , for lepton-like jets, i.e. jets that pass loose lepton identification requirements, to pass the full lepton identification. This probability  $p_F$  is determined in a control region of events which pass  $Z$  boson selection cuts, contain at least one lepton-like

**Table 9.** Event yields in data and estimations of signal and background of the  $WZ$  production in the ATLAS and CMS analyses.

Experiment	ATLAS				
	$eee$	$ee\mu$	$\mu\mu e$	$\mu\mu\mu$	combined
Data	56	75	78	108	317
$WZ$ (MC)	$38.9 \pm 3.1$	$54.0 \pm 2.2$	$56.6 \pm 1.7$	$81.7 \pm 2.1$	$231.2 \pm 4.7$
$Z$ +jets	$8.8 \pm 2.8$	$3.7 \pm 2.3$	$10.2 \pm 3.3$	$9.1 \pm 5.5$	$31.8 \pm 7.4$
$ZZ$	$3.2 \pm 0.2$	$4.9 \pm 0.2$	$5.0 \pm 0.1$	$7.9 \pm 0.2$	$21.0 \pm 0.4$
$Z\gamma$	$1.4 \pm 0.7$	0	$2.3 \pm 0.9$	0	$3.7 \pm 1.1$
top	$1.1 \pm 0.4$	$2.9 \pm 0.9$	$3.6 \pm 1.1$	$4.0 \pm 1.2$	$11.6 \pm 1.9$
Total Background	$14.5 \pm 2.9$	$11.5 \pm 2.5$	$21.0 \pm 3.5$	$21.0 \pm 5.6$	$68.0 \pm 7.6$
Total Expected	$53.4 \pm 4.2$	$65.5 \pm 3.3$	$77.6 \pm 3.9$	$102.7 \pm 6.0$	$300.2 \pm 8.9$
Experiment	CMS				
	$eee$	$ee\mu$	$\mu\mu e$	$\mu\mu\mu$	combined
Data	64	62	70	97	293
$WZ$ (MC)	$44.7 \pm 0.5$	$55.0 \pm 1.0$	$56.0 \pm 0.5$	$73.8.7 \pm 0.6$	$229.5 \pm 1.4$
$Z$ +jets	$1.2 \pm 0.8$	$1.2 \pm 0.9$	$0.8 \pm 0.6$	$0.6 \pm 0.6$	$3.8 \pm 1.5$
$ZZ$	$2.0 \pm 0.1$	$3.5 \pm 0.1$	$2.7 \pm 0.1$	$5.1 \pm 0.1$	$13.3 \pm 0.2$
$Z\gamma$	0	0	$0.5 \pm 0.5$	0	$0.5 \pm 0.5$
top	$0.3 \pm 0.1$	$0.6 \pm 0.1$	$0.6 \pm 0.1$	$1.0 \pm 0.1$	$2.5 \pm 0.2$
Total Background	$3.5 \pm 0.8$	$5.3 \pm 1.0$	$4.6 \pm 0.8$	$6.7 \pm 0.6$	$20.1 \pm 2.6$
Total Expected (MC)	$48.2 \pm 1.0$	$55.0 \pm 1.0$	$60.5 \pm 1.1$	$80.5 \pm 0.9$	$244.2 \pm 2.0$

jet, and have no significant  $E_T^{\text{miss}}$ . The measured fake probability is then applied in the signal region, where only a loose lepton identification is required. The background due to  $t\bar{t}$  is the only background whose leptonic invariant mass does not peak at the  $Z$  boson mass. Hence, by requiring two same-sign leptons to pass the  $Z$  boson mass constraint leads to a top-quark enriched control region which is used to estimate the  $t\bar{t}$  contribution in the signal region. All other backgrounds are theoretically well understood and are estimated with MC simulations. In particular the  $ZZ$  background has a sizable contribution, but since it is mainly due to limited detector acceptance it can be precisely estimated using simulated MC events.

The CMS analysis uses a common data-driven technique to estimate the background from  $t\bar{t}$  and  $Z$ +jets, which are due to fake leptons. The basic idea is to define some looser lepton identification requirements to enhance the background contribution. The probability for leptons that have passed the ‘loose’ identification criteria to also pass the nominal identification is estimated from data using independent samples. Knowing these probabilities, it is possible to construct a set of linear equations which relate the number of selected events in different event categories. Each event category is defined by the number of prompt and fake leptons. This set of equations leads to a unique solution for the number of background events in the signal region. The backgrounds from  $ZZ$  and  $Z\gamma$  are also estimated using simulated MC events.

Figure 14 shows the invariant mass of the  $M_{WZ}$  system and the  $p_T$  spectrum of the selected  $Z$  boson in the signal region for both data and MC for the ATLAS analysis.

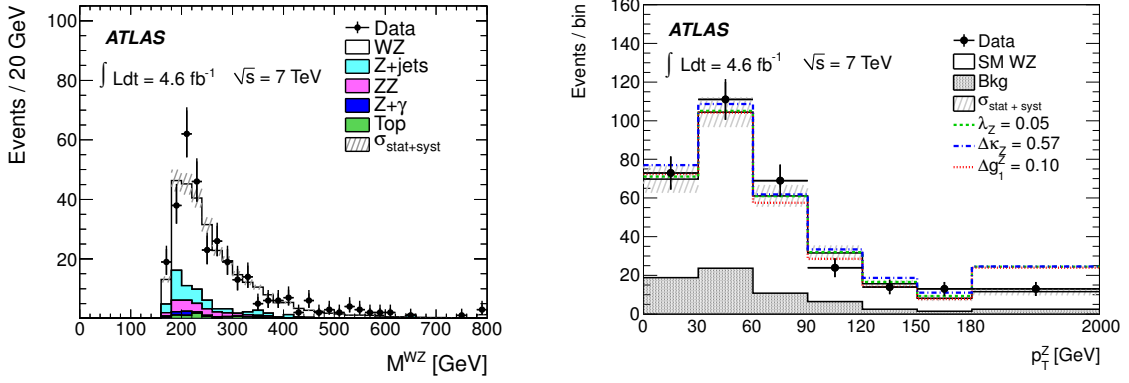


**Figure 14.** ATLAS: Invariant mass  $m_{WZ}$ -distribution (left) and  $p_T^Z$ -distribution (right) of the  $W^\pm Z$  pair after all selections. The shaded bands indicate the total statistical and systematic uncertainties of the MC prediction. The right-most bin contains overflow.

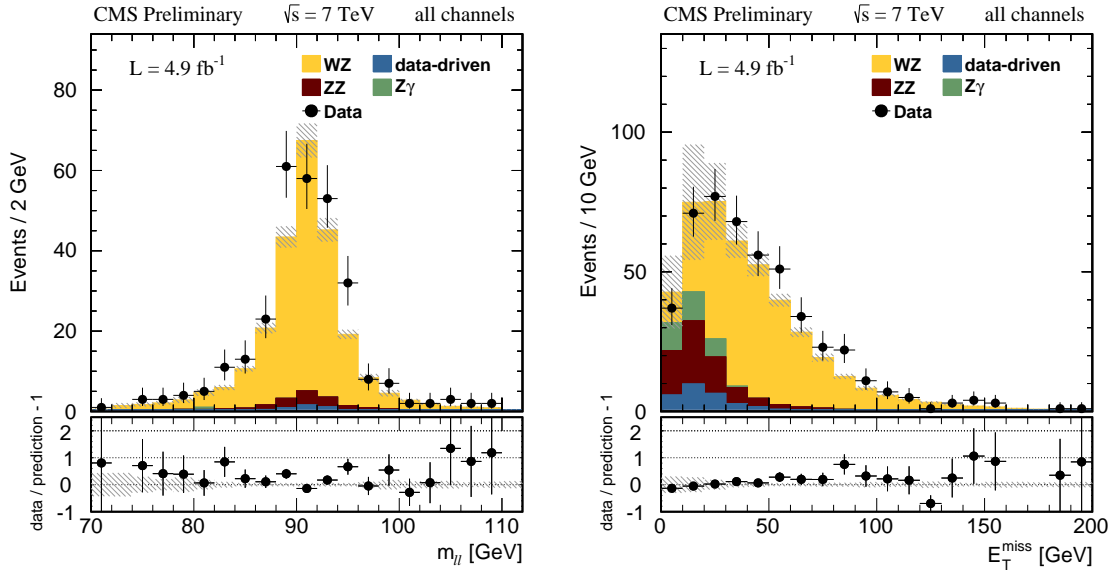


**Figure 15.** CMS:  $Z$  boson candidate lepton invariant mass  $m_{ll}$ -distribution (left) and  $E_T^{\text{miss}}$ -distribution (right) for selected  $W^\pm Z$  candidates (right). The shaded bands indicate the total statistical and systematic uncertainties of the MC prediction.

Figure 15 shows the invariant mass distribution of the  $Z$  boson candidate lepton pair and the observed  $E_T^{\text{miss}}$  spectrum for the CMS analysis. A good description of the data by the MC prediction is observed in both analyses.

### 4.2.3 Cross Section Measurement

The fiducial phase space in ATLAS at the generator level is defined along the kinematic requirements and presented in Tab. 8. The momenta of photons within  $\Delta R < 0.1$  of signal leptons are added to the respective lepton  $p_T$ . The resulting acceptance factors  $A_{WZ}$  for all decay channels range from 0.330 to 0.338. The differences are caused by final state



radiation photons. The corresponding uncertainties due to PDFs and momentum scales are evaluated similarly to the ATLAS  $WW$  analysis. The main uncertainty is due to the limited knowledge of PDFs, which leads to an uncertainty of 1.4%.

The detector correction factors  $C_{WZ}$  range from 0.8 in the  $\mu\mu\mu$  channel to 0.4 in the  $eee$  channel. The differences are due to the lower electron identification efficiencies compared to the muon channel. The primary uncertainties on  $C_{WZ}$  are due to the limited knowledge of the lepton reconstruction efficiencies and momentum scales and resolution.

CMS did not publish a fiducial cross section number. The product of the acceptance and efficiency correction factors  $A_{WZ} \cdot C_{WZ}$  are comparable to the ATLAS analyses. The dominate experimental uncertainties are due to  $E_T^{\text{miss}}$  requirement and lepton reconstruction and trigger efficiencies.

The fiducial and inclusive cross section is then calculated for each channel separately. A mass-cut of  $66 < m_{\ell^+\ell^-} < 116$  GeV is required for the inclusive cross section in order to define an on-shell  $Z$  boson. The cross sections are calculated with respect to the corresponding process  $W^\pm Z \rightarrow \ell'^{\pm}\nu\ell^+\ell^-$ , i.e. the contribution from  $\tau$  lepton decays has to be removed. This is done by multiplying the final cross-section by a factor  $(1 - N_\tau^{MC}/N_{sig}^{MC})$  where  $N_\tau^{MC}$  is the number of reconstructed and selected  $WZ$  where at least one  $\tau$ -decay is present, and  $N_{sig}^{MC}$  is the number of all reconstructed and selected  $WZ$  events. The contribution from  $\tau$  decays is in the order of 4%. The individual cross sections are then combined via a maximum likelihood method, leading to the results shown in Tab. 10. The main systematic uncertainties are due to the data-driven background estimates and contribute 4% to the total systematic uncertainty of 4.6% in the fiducial phase space.

The preliminary CMS results from [89] are also presented. The combined cross section is obtained by combining the four decay channels, requiring  $71 < m_{\ell\ell} < 111$  GeV.

**Table 10.** Summary of measured inclusive cross sections for the  $WZ$  process from the ATLAS and CMS collaborations.

	Measured	Predicted
ATLAS		
$\sigma^{fid}(WZ \rightarrow \ell^+\ell^-\ell'\nu)$	$92 \pm 7 (stat.) \pm 4 (sys.) \pm 2 (lumi.)$ fb	
$\sigma^{incl.}(WZ \rightarrow \ell^+\ell^-\ell'\nu)$	$19.0 \pm 1.4 (stat.) \pm 0.9 (sys.) \pm 0.4 (lumi.)$ pb	$17.7 \pm 1.1$ pb
CMS		
$\sigma^{incl.}(WZ \rightarrow e^+e^-e^\pm\nu)$	$23.0 \pm 3.1 (stat.) \pm 1.4 (sys.) \pm 0.5 (lumi.)$ pb	$17.7 \pm 1.1$ pb
$\sigma^{incl.}(WZ \rightarrow e^+e^-\mu^\pm\nu)$	$19.7 \pm 2.7 (stat.) \pm 1.5 (sys.) \pm 0.4 (lumi.)$ pb	$17.7 \pm 1.1$ pb
$\sigma^{incl.}(WZ \rightarrow \mu^+\mu^-e^\pm\nu)$	$19.8 \pm 2.6 (stat.) \pm 1.6 (sys.) \pm 0.4 (lumi.)$ pb	$17.7 \pm 1.1$ pb
$\sigma^{incl.}(WZ \rightarrow \mu^+\mu^-\mu^\pm\nu)$	$21.0 \pm 1.6 (stat.) \pm 1.5 (sys.) \pm 0.5 (lumi.)$ pb	$17.7 \pm 1.1$ pb
$\sigma^{incl.}(WZ \rightarrow \ell^+\ell^-\ell'^\pm\nu)$	$20.8 \pm 1.3 (stat.) \pm 1.1 (sys.) \pm 0.5 (lumi.)$ pb	$17.7 \pm 1.1$ pb

Within the fiducial region, ATLAS also published normalized unfolded distributions of  $M_{WZ}$  and  $p_T^Z$ , shown in Fig. 16. These can be used to constrain aTGC couplings without knowing details of detector effects and resolution. A good agreement with the MC prediction is seen.

CMS measured the ratio of the production cross-sections of  $W^+Z$  and  $W^-Z$ , as they

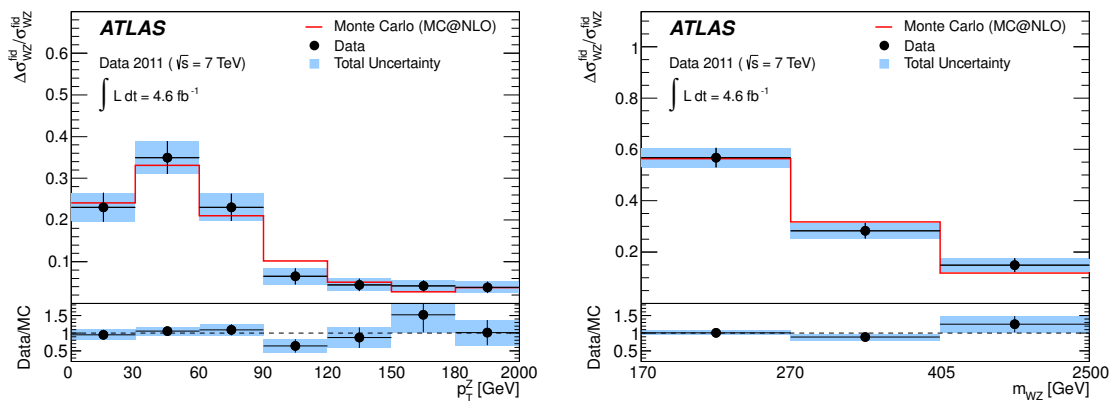


**Figure 16.** Normalized fiducial cross-sections in bins of  $p_T^Z$  (left) and  $m_{WZ}$  compared with the SM prediction. The full uncertainty contains statistical and systematic uncertainties.

are not expected to be the same in a proton-proton collider. Several systematic uncertainties cancel in the ratio, such as the luminosity uncertainty. The resulting combined cross section ratio is found to be  $\sigma_{W+Z}/\sigma_{W-Z} = 1.94 \pm 0.25(\text{stat.}) \pm 0.04(\text{syst.})$ , and is in agreement with the NLO QCD calculation of  $1.724 \pm 0.003$  using MCFM and the MSTW2008 PDF set.

#### 4.2.4 Derived Results and Discussion

For the combination of the inclusive  $WZ$  cross section measurements from both experiments, it is assumed that the uncertainties due to integrated luminosity are fully correlated while all other uncertainties are uncorrelated. The BLUE method yields a combined cross section of

$$\sigma_{WZ}^{LHC} = 19.9 \pm 1.0(\text{stat.}) \pm 0.8(\text{syst.}) \text{ pb.}$$

The measured cross section is in good agreement with the theoretical prediction of  $17.6 \pm 1.1 \text{ pb}$  (as shown in Tab. 1). In contrast to the  $WW$  measurement, the statistical uncertainty is the dominant uncertainty in the 7 TeV dataset and is expected to be reduced by a factor of  $\approx 2.5$  in the ongoing analyses of the 8 TeV dataset. However, the overall relative precision of this measurement is better by 15% compared to the  $WW$  analyses and hence provides also an improved test of the SM prediction of the diboson production.

A simplified fiducial cross section for  $WZ$  events is defined by requiring three charged leptons on the generator level with  $p_T > 20 \text{ GeV}$  and  $|\eta| < 2.5$ , one neutrino with  $p_T > 20 \text{ GeV}$  and an invariant mass cut on the leptons from the  $Z$  boson decay of  $|m_Z - m_{\ell\ell}| < 30 \text{ GeV}$ . The extrapolation factor from the ATLAS definition to the simplified phase space is evaluated with MC@NLO and leads to  $1.07 \pm 0.02$ , where uncertainties due to momentum scales and PDFs are included. The simplified cross section is found to be

$$\sigma_{WZ}^{fid,sim} = 98 \pm 7(\text{stat.}) \pm 5(\text{syst.}) \pm 2(\text{lumi.}) \text{ fb.}$$

The cross section within this simplified fiducial phase space but requiring that the  $p_T$  of the  $Z$  boson in the range  $180 \text{ GeV} < p_T^Z < 2000 \text{ GeV}$ , results in  $\sigma_{WZ}^{fid,sim}(180 \text{ GeV} < p_T^Z <$

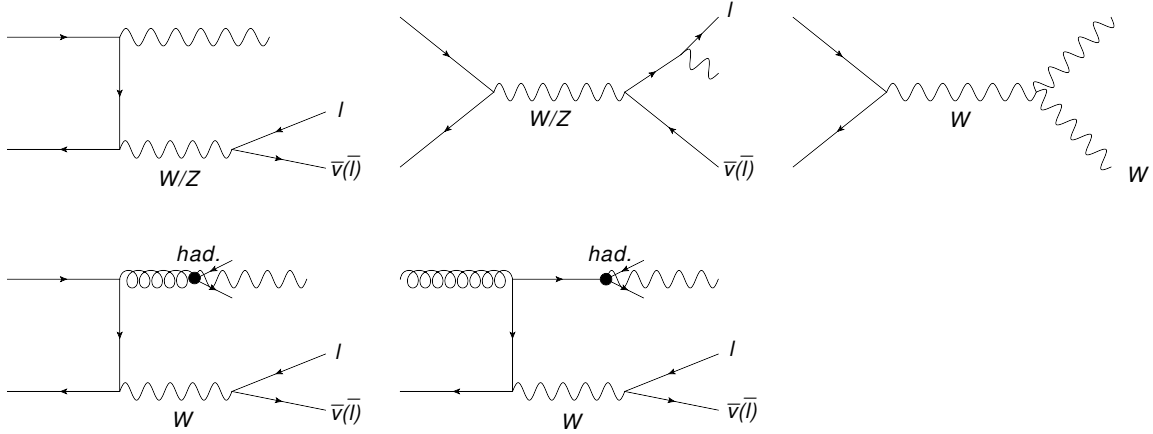


**Figure 17.** Feynman diagrams for  $W\gamma$  and  $Z\gamma$  production via the  $u$ - and  $t$ -channels (upper left), final state radiation (upper middle), and the  $s$ -channel for  $W\gamma$  production (upper right). Photons in the final state can also be produced in the fragmentation of final state quarks and gluons (lower row).

2000 GeV) =  $4.1 \pm 1.4$  fb, where the corresponding extrapolation factor is again based on MC@NLO predictions. This cross section can be used to test specifically the TGC vertex of  $WZ$  production.

### 4.3 $W\gamma$ Analysis

In the SM, the production process  $pp \rightarrow W\gamma \rightarrow \ell\nu\gamma$  ( $\ell = e, \mu$ ) originates from  $W$  production with photons radiated from initial-state quarks or directly by the  $W$  bosons. Other SM processes such as  $W$  production with photon bremsstrahlung from the charged leptons from the  $W$  boson decays or with photons from the fragmentation of secondary quarks and gluons into isolated photons can result in the same final state (see Fig. 17). Both ATLAS and CMS collaborations have measured the  $W\gamma$  production cross section in the electron and muon decay channels [90, 91].

#### 4.3.1 Event Selection

For the ATLAS  $W\gamma \rightarrow \ell\nu\gamma$  analysis, candidate events are selected by requiring exactly one lepton with  $p_T > 25$  GeV, at least one isolated photon with  $E_T > 15$  GeV, and  $E_T^{\text{miss}} > 35$  GeV. Leptons and photons are required to be within the detector fiducial region. All selected leptons must satisfy isolation requirements based on calorimeter (for electrons) or tracking (for muons) information and must be consistent with originating from the primary vertex. Electromagnetic clusters without matching tracks are directly classified as unconverted photon candidates, while clusters that are matched to tracks that originate from reconstructed conversion vertices in the tracker or to tracks consistent with coming from a conversion are considered as converted photon candidates. Tight requirements on the photon shower shapes are applied to suppress the background from multiple showers produced in meson decays. Leptons and photons have the same isolation requirement

which is  $\Delta R(\ell, \gamma) > 0.7$  in order to suppress the contributions from FSR photons in the  $W$  boson decays. The  $W\gamma$  candidates are also required to have the transverse mass of the lepton- $E_T^{\text{miss}}$  system greater than 40 GeV. A veto on reconstructed  $Z$  boson events is applied in the electron channel ( $|m_{e\gamma} - m_Z| > 15$  GeV) to reject contributions from the  $Z\gamma \rightarrow e^+e^-\gamma$  process where one of the electrons is misidentified as an isolated photon. ATLAS also measured the cross sections for events with and without the requirement of zero jets reconstructed in each event. Jets are required to have  $E_T > 30$  GeV and  $|\eta| < 4.4$ .

Similar event selection criteria are used for the CMS  $W\gamma \rightarrow \ell\nu\gamma$  analysis except that lepton candidates are required to have  $p_T > 35$  GeV and only photon candidates without associated tracks in the pixel detector are considered. No selection cut is applied on  $E_T^{\text{miss}}$  and instead the transverse mass of the lepton- $E_T^{\text{miss}}$  system is required to be greater than 70 GeV. A summary of the detailed selection cuts for both experiments of shown in Table 11.

**Table 11.** Summary of the  $W\gamma \rightarrow \ell\nu\gamma$  selection cuts used by the ATLAS and CMS collaborations.

	ATLAS	CMS
$W\gamma \rightarrow \ell\nu\gamma$	Combined muons with $p_T > 25$ GeV	Muons with $p_T > 35$ GeV
$(\ell' = e, \mu)$	Combined electrons with $E_T > 25$ GeV	Electrons with $p_T > 35$ GeV
	Photon $E_T > 15$ GeV and $E_T^{\Delta R < 0.3} < 6$ GeV	Photon $E_T > 15$ GeV, isolation and shower-shape requirements
	$E_T^{\text{miss}} > 35$ GeV, $m_T(\ell\nu) > 40$ GeV	$m_T(\ell\nu) > 70$ GeV
	$ m_{e\gamma} - m_Z  > 15$ GeV and only one lepton	only one lepton
	$\Delta R(\ell, \gamma) > 0.7$	$\Delta R(\ell, \gamma) > 0.7$

#### 4.4 Background Estimation

The primary backgrounds to the  $\ell\nu\gamma$  signal come from the  $W$ +jets,  $Z \rightarrow \ell\ell$ ,  $\gamma$ + jets, and  $t\bar{t}$ , single top quark and  $WW$  processes.

Data is used to estimate the background from the  $W$ + jets production when photons come from the decays of mesons produced in jet fragmentation. ATLAS used a two-dimensional sideband method which considered the distribution of signal and background events in a phase space defined by two uncorrelated variables for which the signal and background have different shapes. The phase space is partitioned into four regions with one signal region and three control regions in which one or both selections are reversed. The ratio of the number of background events in two control regions provides the transfer factor which is combined with events in the third control region to estimate the background contribution in the signal region. The two discriminating variables are the photon isolation and the photon identification based on the shower shape in the ATLAS analysis. CMS used a template method which relies on a maximum-likelihood fit to the data distribution of the photon energy-weighted width in pseudorapidity ( $\sigma_{\eta\eta}$ ). The fit makes use of the expected distributions ("templates") for genuine photons and misidentified jets. The distribution in  $\sigma_{\eta\eta}$  is very narrow and symmetric, and the templates are obtained from simulated  $W\gamma$  events. The  $\sigma_{\eta\eta}$  distribution for backgrounds is asymmetric with a slow falloff at large

value, and the templates are defined by events in a background-enriched isolation sideband of data. The maximum-likelihood fit is performed in several photon  $p_T$  bins. The estimated background contribution has been crosschecked with an alternative method. The prediction from the alternative approach is found to be consistent with the template method, and their difference is treated as an additional source of systematic uncertainty in the analysis.

Further background is due to the  $Z/\gamma^* \rightarrow \ell\ell$  production, when one of the leptons is misidentified as a photon or is not identified and the photon originates from initial state radiation or from bremsstrahlung from a decay lepton. ATLAS used MC simulation for its estimation, and various studies of the probability to lose one lepton from  $Z$  decay due to acceptance and the modeling of  $E_T^{\text{miss}}$  in  $Z + \gamma$  and  $Z + \text{jets}$  events have been performed and checked with collision data. ATLAS also used a two-dimensional sideband method to estimate the  $\gamma + \text{jets}$  background, with lepton isolation and  $E_T^{\text{miss}}$  as the independent variables. CMS used a data-driven method to estimate the  $Z/\gamma^* \rightarrow \ell\ell$  background. The background in the  $e\nu\gamma$  decay channel is dominated by  $Z + \text{jets}$  events, and the contribution is obtained from a fit to the invariant mass distribution of the photon and electron candidates. To determine the background in the  $\mu\nu\gamma$  decay channel where an electron is misidentified as a photon, a new sample is selected with events passing all event selection criteria except that the presence of a track in the pixel detector associated with the photon candidate is ignored. The contribution from genuine electrons misidentified as photons can therefore be derived from the total number of events in this new sample and the probability for an electron not to have a matching track. This probability can be measured from  $Z \rightarrow ee$  data by requiring stringent electron identification criteria on one electron and checking how often the other electron passes the full photon selection criteria, including the requirement of having no associated track in the pixel detector.

All other backgrounds are estimated using MC simulations for both ATLAS and CMS analyses. A summary of the expected signal and background events is given in Table 12. The primary background contribution and also the dominant associated uncertainty is due to the  $W + \text{jets}$  process for both experiments. The signal to background ratio is significantly better for the ATLAS analysis, which can be explained by the superior performance of the ATLAS electromagnetic calorimeter.

#### 4.4.1 Fiducial Cross Section Results

The expected and observed event yields after applying all selection criteria are shown in Tab. 12 for all decay channels. The photon transverse energy and  $E_T^{\text{miss}}$  distributions for all selected  $\ell\nu\gamma$  candidate events are shown in Fig. 18 for the ATLAS analysis, and the photon transverse energy distribution is shown separately for the electron and muon decay channels in Fig. 19 for the CMS analysis. Reasonable agreement between the data and expected signal and background contributions are observed from each experiment.

ATLAS measured the production cross section in an extended fiducial region defined as charged lepton  $p_T > 25$  GeV and  $|\eta| < 2.47$ , neutrino  $p_T > 35$  GeV, and photon  $E_T > 15$  GeV and  $\Delta R(\ell, \gamma) > 0.7$ . Cross sections for events with and without the requirement of zero jets are listed separately. The jets are required to have  $E_T > 30$  GeV and  $|\eta| < 4.4$ . CMS measured the production cross section in an extended fiducial region defined as photon

**Table 12.** Summary of observed  $W\gamma$  candidates in the data, background estimates, and expected signal for the individual decay modes. The first uncertainty is statistical while the second is systematic.

	ATLAS		CMS	
	$e\nu\gamma$	$\mu\nu\gamma$	$e\nu\gamma$	$\mu\nu\gamma$
$W$ +jets	$1240 \pm 160 \pm 210$	$2560 \pm 270 \pm 580$	$3180 \pm 50 \pm 300$	$5350 \pm 60 \pm 510$
$Z(\rightarrow \ell\ell) + X$	$678 \pm 18 \pm 86$	$779 \pm 19 \pm 93$	$690 \pm 20 \pm 50$	$91 \pm 1 \pm 5$
$\gamma$ +jets	$625 \pm 80 \pm 86$	$184 \pm 9 \pm 15$	N/A	N/A
$t\bar{t}$	$320 \pm 8 \pm 28$	$653 \pm 11 \pm 57$	N/A	N/A
Other backgrounds	$141 \pm 16 \pm 13$	$291 \pm 29 \pm 26$	$410 \pm 20 \pm 30$	$400 \pm 20 \pm 30$
Signal	$4390 \pm 200 \pm 250$	$6440 \pm 300 \pm 590$	$3200 \pm 100 \pm 320$	$4970 \pm 120 \pm 530$
Observed	7399	10914	7470	10809

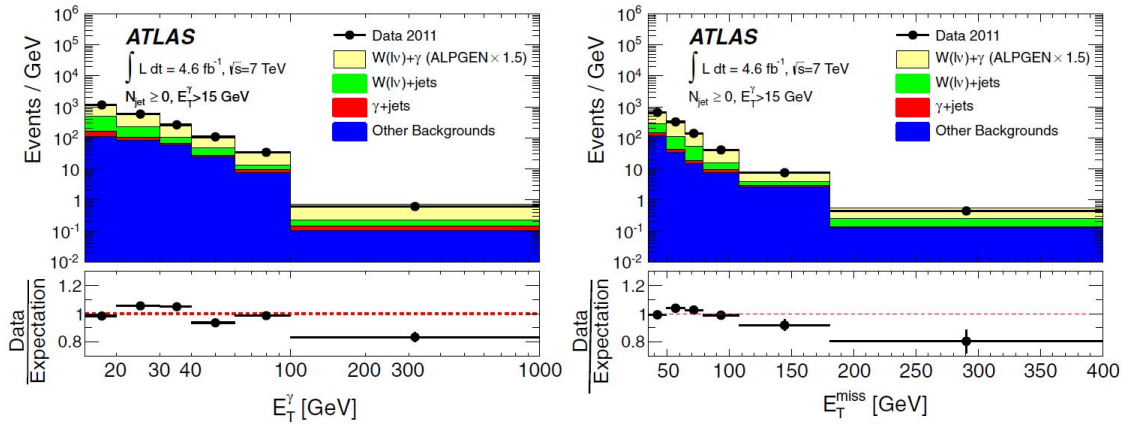


**Figure 18.** Combined distributions for  $l\nu\gamma$  candidate events in the electron and muon channels of the photon transverse energy (left) and the missing transverse energy (right) for the ATLAS analysis.

$E_T > 15$  GeV and  $\Delta R(\ell, \gamma) > 0.7$ . The measured and predicted cross sections are listed in Tab. 13. ATLAS also measured the unfolded differential cross section as a function of the photon  $E_T$  of the  $W\gamma \rightarrow l\nu\gamma'$  process. The results are shown separately for the inclusive ( $N_{jet} \geq 0$ ) and exclusive ( $N_{jet} = 0$ ) fiducial regions.

ATLAS also measured the differential cross section as a function of the photon  $E_T$  using combined electron and muon measurements in the inclusive ( $N_{jet} \geq 0$ ) and exclusive ( $N_{jet} = 0$ ) fiducial regions. CMS measured the  $W\gamma$  production cross section for three different photon  $E_T$  thresholds (15 GeV, 60 GeV, and 90 GeV). The measured cross sections are compared with several theoretical predictions as shown in Fig. 20.

#### 4.4.2 Derived Results and Discussion

Since ATLAS and CMS measured the  $W\gamma$  cross section in different phase spaces we adopt the extended fiducial region defined by the CMS collaboration in order to combine the cross sections. The CMS predicted theoretical cross section number is used and the ATLAS mea-



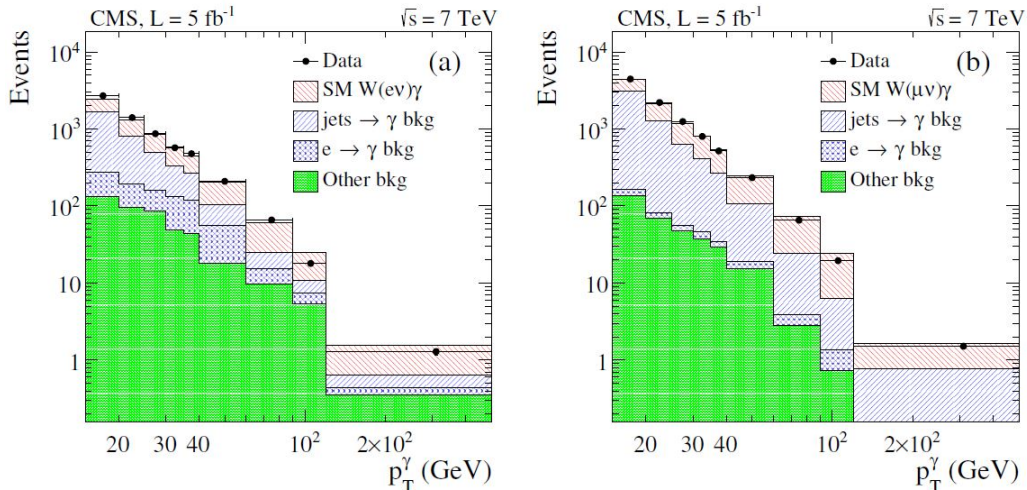


**Figure 19.** Distributions in  $p_T^\gamma$  for  $l\nu\gamma$  candidate events in data: signal and background MC simulation contributions to  $W\gamma \rightarrow e\nu\gamma$  (left) and  $W\gamma \rightarrow \mu\nu\gamma$  (right). The same channels are shown for comparison for the CMS analysis.

**Table 13.** Summary of the measured and predicted  $W\gamma \rightarrow l\nu\gamma$  cross sections from the ATLAS and CMS collaborations. Different fiducial regions are defined by the ATLAS and CMS collaborations.

	Measured [pb]	Predicted [pb]
ATLAS		
$\sigma_{W\gamma \rightarrow l\nu\gamma}^{fid} (N_{jet} \geq 0)$	$2.77 \pm 0.03$ (stat.) $\pm 0.33$ (syst.) $\pm 0.14$ (lumi.)	$1.96 \pm 0.17$
$\sigma_{W\gamma \rightarrow l\nu\gamma}^{fid} (N_{jet} = 0)$	$1.76 \pm 0.03$ (stat.) $\pm 0.21$ (syst.) $\pm 0.08$ (lumi.)	$1.39 \pm 0.13$
CMS		
$\sigma_{W\gamma \rightarrow l\nu\gamma}^{fid}$	$37.0 \pm 0.8$ (stat.) $\pm 4.0$ (syst.) $\pm 0.8$ (lumi.)	$31.8 \pm 1.8$

sured inclusive cross section number is scaled up by  $16.2 \pm 0.4$ . The statistical uncertainties for both measurements are treated independently. The uncertainties on the integrated luminosity are treated as fully correlated. Other systematic uncertainties are dominated by uncertainties related to the  $W$ +jets and  $Z$ +jets data-driven background estimation, lepton, photon and  $E_T^{\text{miss}}$  identification, and energy and resolution. These uncertainties are treated to be completely uncorrelated between the two experiments. Using the BLUE method, the combined inclusive cross section is found to be

$$\sigma(pp \rightarrow W\gamma) = 39.6 \pm 0.6(\text{stat.}) \pm 3.5(\text{syst.}) \text{ fb},$$

which is consistent with a theoretical prediction of  $31.8 \pm 1.8$  fb.

## 5 Studies of the $ZZ^{(*)}$ and $Z\gamma$ final states

In contrast to the decay channels discussed in the previous section, the  $ZZ^{(*)}$  and  $Z\gamma$  final states can occur only via  $t$ - and  $u$ -channels within the SM. The study of their production

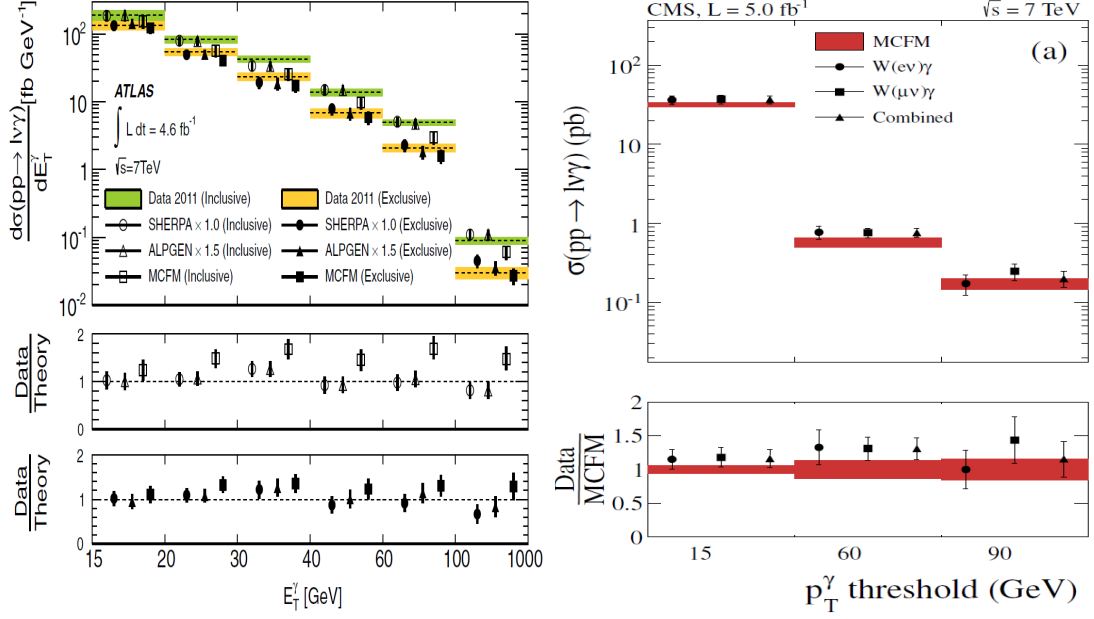


**Figure 20.** Left: Measured photon  $E_T$  differential cross section of the  $W\gamma \rightarrow \ell\nu\gamma$  process, using combined electron and muon measurements in the inclusive ( $N_{jet} \geq 0$ ) and exclusive ( $N_{jet} = 0$ ) fiducial regions. Right: Measured  $W\gamma$  cross sections for three photon  $E_T$  thresholds, compared to SM predictions.

could therefore test the existence of an anomalous  $ZZZ$ ,  $ZZ\gamma$  or  $Z\gamma\gamma$  vertex. Similar to the previous measurements, the event selection, the background estimation methods and results of both experiments for the production cross section measurements are summarized in this section. We also give special emphasis on the differences between the two experiments and derive combinations of the measured cross sections.

### 5.1 $ZZ^{(*)}$ Analysis

In the SM, non-resonant  $ZZ^{(*)}$  production proceeds via the  $t$ - and  $u$ -channel  $q\bar{q}$  interactions and via gluon-gluon fusion. Both ATLAS and CMS collaborations have measured the  $ZZ$  production cross section using events that are consistent with two  $Z$  bosons decaying to electrons or muons ( $ZZ \rightarrow \ell\ell'\ell'$  with  $\ell, \ell' = e, \mu$ ) [92, 93]. ATLAS also lowered the mass requirement for the second dilepton pair to measure the production cross section for the  $ZZ^* \rightarrow \ell\ell'\ell'$  process [92]. In addition, CMS measured the production cross section for events with one  $Z$  boson decaying to  $e^+e^-$  or  $\mu^+\mu^-$  and a second  $Z$  boson decaying to  $\tau^+\tau^-$  in four possible final states:  $\tau_h\tau_h$ ,  $\tau_e\tau_h$ ,  $\tau_\mu\tau_h$  and  $\tau_e\tau_\mu$ , where  $\tau_h$  represents a  $\tau$  decaying hadronically, while  $\tau_e$  and  $\tau_\mu$  indicate taus decaying into an electron or a muon, respectively[93]. The ATLAS collaboration also measured the  $ZZ \rightarrow \ell\nu\nu$  production cross section using events with one  $Z$  boson decaying to electrons or muons and a second  $Z$  boson decaying to neutrinos [92].



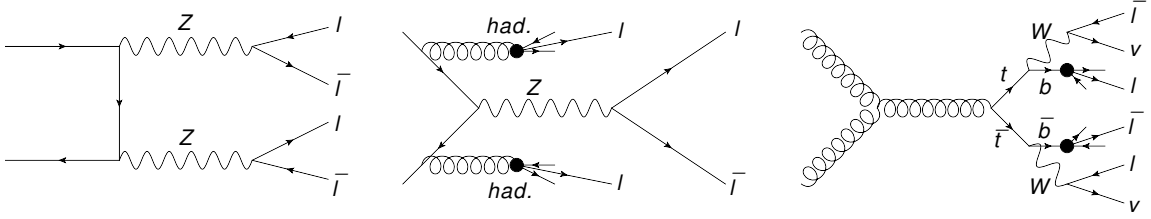


**Figure 21.** Feynman diagrams for the  $t$ -channel  $ZZ$  signal process (left) and dominant background processes (middle:  $Z$ +jets, right:  $t\bar{t}$  pair production).

### 5.1.1 Event Selection

The presence of four high- $p_T$  leptons in the final state for the  $ZZ^{(*)} \rightarrow \ell\ell'\ell'$  process provides a clean signature with only a small contribution from other SM background processes (see Fig. 21). Loose lepton selection criteria are thus applied to maximize the overall signal acceptance times efficiency. The  $ZZ \rightarrow \ell\nu\nu$  process is characterized by large  $E_T^{\text{miss}}$  and two high- $p_T$  isolated electrons or muons. It has a branching ratio six times larger than the purely leptonic decay processes  $ZZ^{(*)} \rightarrow \ell\ell'\ell'$ . However larger SM background from the  $Z$ +jets process is expected and thus tighter selection criteria are used.

For the ATLAS  $ZZ^{(*)} \rightarrow \ell\ell'\ell'$  selection, highly energetic electrons are required (i.e.  $E_T > 20$  GeV) satisfying the loose identification criterion, while muons are required only to fulfill a rather loose momentum cut of  $p_T > 7$  GeV. All selected leptons must satisfy isolation requirements based on calorimetric and tracking information and must be consistent with originating from the primary vertex. Forward spectrometer and calorimeter-tagged muons as well as calorimeter-only electrons passing the tight identification requirements are also considered in order to increase the overall signal acceptance.

Selected events are required to have at least one highly energetic electron (muon) with  $p_T > 25(20)$  GeV and to contain two pairs of same-flavor, oppositely-charged leptons. In the  $4e$  and  $4\mu$  channels, ambiguities are resolved by choosing the combination which produces the smallest sum of relative differences between the dilepton mass and the  $Z$  boson mass from each pair. At least one lepton pair is required to have an invariant mass within the  $Z$  mass window ( $66 < m_{\ell\ell} < 116$  GeV). If the second  $Z$  candidate has  $66 < m_{\ell\ell} < 116$  GeV the event is classified as a  $ZZ$  event; if the second candidate satisfies  $m_{\ell\ell} > 20$  GeV, the event is classified as a  $ZZ^*$  event.

For the CMS  $ZZ \rightarrow \ell\ell'\ell'$  selection electrons are selected with a threshold of 7 GeV and muons are selected with a threshold of 5 GeV. Events are required to have at least one  $Z \rightarrow \ell\ell$  candidate with  $60 < m_{\ell\ell} < 120$  GeV. The leading lepton must have  $p_T > 20$  GeV. Lepton isolation requirements depend on the  $ZZ$  decay mode.

The  $\tau$  leptons are required to fulfill the kinematic requirements of  $p_T > 20$  GeV and  $|\eta| < 2.3$ . Since hadronically decaying  $\tau$  leptons have much larger misidentification rates than the other leptons, tighter electron and muon isolation criteria are applied for the electrons and muons in the final states  $\tau_e\tau_h$  and  $\tau_\mu\tau_h$ .

For the ATLAS  $ZZ \rightarrow \ell\nu\nu$  selection, leptons are required to have  $p_T > 20$  GeV.

Selected candidate events are required to have exactly two same-flavor leptons with  $76 < m_{\ell\ell} < 116$  GeV. Events with a third electron or muon with  $p_T > 10$  GeV are rejected to reduce the  $WZ \rightarrow \ell\nu\ell'\ell'$  background. Events containing at least one well-reconstructed jet with  $p_T > 25$  GeV are vetoed to reduce top quark background. To remove the dominant  $Z$ +jets background, a minimal cut on the so-called axial- $E_T^{\text{miss}}$  of 75 GeV is applied<sup>3</sup>. The two  $Z$  bosons from the  $pp \rightarrow ZZ \rightarrow \ell\nu\nu$  process tend to have similar transverse momenta. To exploit this tendency, the fractional difference between  $E_T^{\text{miss}}$  and  $p_T^Z$ ,  $|E_T^{\text{miss}} - p_T^Z|/p_T^Z$ , is required to be less than 0.4.

The details of the selection criteria used for all  $ZZ^{(*)}$  analyses are summarized in Tab. 14.

**Table 14.** Summary of  $ZZ^{(*)}$  selection cuts used by the ATLAS and CMS collaborations.

	ATLAS	CMS
$ZZ^{(*)} \rightarrow$ $\ell^+\ell^-\ell'^+\ell'^-$ ( $\ell, \ell' = e, \mu$ )	Combined, forward or calorimeter-tagged muons Combined or calorimeter-only electrons $\geq$ one lepton with $p_T^{e(\mu)} > 25(20)$ GeV First $Z$ with $66 < m_{\ell\ell} < 116$ GeV Second $Z$ with $66 < m_{\ell\ell} < 116$ GeV ( $ZZ$ ) Second $Z$ with $m_{\ell\ell} > 20$ GeV ( $ZZ^*$ )	Muons with $p_T > 5$ GeV, $ \eta  < 2.4$ Electrons with $E_T > 7$ GeV, $ \eta  < 2.5$ $\geq$ one lepton with $p_T > 20$ GeV First $Z$ with $60 < m_{\ell\ell} < 120$ GeV Second $Z$ with $60 < m_{\ell\ell} < 120$ GeV
$ZZ \rightarrow$ $\ell^+\ell^-\tau^+\tau^-$ ( $\ell = e, \mu$ )		$\geq$ one lepton from $Z$ with $p_T^{e(\mu)} > 20$ GeV $\tau_{e,\mu}$ lepton with $p_T^{e(\mu)} > 10$ GeV $\tau_h$ lepton with $p_T > 20$ GeV and $ \eta  < 2.3$ $30 < m_{\tau\tau}^{\text{vis}} < 80$ GeV for $\tau_h\tau_{e,\mu}$ $30 < m_{\tau\tau}^{\text{vis}} < 90$ GeV for $\tau_e\tau_\mu$
$ZZ \rightarrow$ $\ell^+\ell^-\nu\nu$ ( $\ell = e, \mu$ )	Combined muons (electrons) $76 < m_{\ell^+\ell^-} < 106$ GeV Axial- $E_T^{\text{miss}} > 75$ GeV $ E_T^{\text{miss}} - p_T^Z /p_T^Z < 0.4$ Third lepton veto, jet veto	

### 5.1.2 Background Estimation

For the  $ZZ \rightarrow \ell\ell\ell'\ell'$  channel, the major contributions to the background are due to  $Z$  and  $WZ$  production in association with jets or  $t\bar{t}$ . In all of these cases a jet or non-isolated lepton is misidentified as an isolated lepton. The relative contribution of each background source depends on the final state. The rate for loosely-isolated objects to be misidentified as isolated ones is estimated with events with one selected  $Z$  boson and an additional probe lepton. No isolation requirement is applied to the probe lepton. The misidentification rate is defined as the ratio of the number of probe candidates that pass the isolation requirements to the initial number of probe candidates. This rate is then applied to events which pass all

<sup>3</sup>Axial- $E_T^{\text{miss}}$  is defined as the projection of the  $E_T^{\text{miss}}$  along the direction opposite to the  $Z$  candidate direction in the transverse plane.

selection requirements but requiring the probe candidate not to be isolated to estimate the number of background events in the signal region. The uncertainties on  $Z$ +jets,  $WZ$ +jets and  $t\bar{t}$  backgrounds reflect the uncertainties of the misidentification rates and the limited quantity of data in the control region, and amount to 30 – 50% depending on the decay channel.

For the  $ZZ \rightarrow \ell\nu\nu$  channel, the major contributions to the background are due to  $Z \rightarrow \tau\tau$ ,  $WW$ ,  $WZ$ ,  $Wt$  and  $t\bar{t}$  production that result in two true isolated leptons with missing transverse energy. Production of a  $Z$  (or  $W$ ) boson in association with jets can also give similar final states if the jet momenta are mismeasured or if one jet is misidentified as an isolated lepton. The contributions from  $Z \rightarrow \tau\tau$ ,  $Wt$ ,  $WW$  and  $t\bar{t}$  processes are measured by extrapolating from a control sample of events with one electron and one muon which otherwise satisfy the full  $ZZ \rightarrow \ell\nu\nu$  selection. The extrapolation from the  $e\mu$  channel to the  $ee$  or  $\mu\mu$  channel uses the relative branching fractions as well as the ratio of the efficiencies  $\epsilon_{ee}$  or  $\epsilon_{\mu\mu}$  of the  $ee$  or  $\mu\mu$  selections to the efficiency  $\epsilon_{e\mu}$  of the  $e\mu$  selection, which differs from unity due to differences in the electron and muon efficiencies. The contribution from the  $WZ$  process is estimated using the simulated samples and checked using a control region with three high- $p_T$  isolated leptons. The contribution from the  $Z$ +jets process is estimated using events with a high- $p_T$  photon and jets as a template, since the mechanism for large missing transverse energy is the same as in  $Z$ +jets events. The events are reweighted such that the photon  $p_T$  matches the observed  $Z$  boson  $p_T$  and are normalized to the observed  $Z$ +jets yield. The procedure is repeated in bins of  $Z$  boson  $p_T$  in order to obtain the  $p_T$  distribution of the  $Z$ +jets backgrounds. The background from processes in which one of the two leptons comes from the decays of a  $W$  or  $Z$  boson and the second lepton from non-prompt leptons or misidentified mesons or conversions is found to be negligible.

### 5.1.3 Inclusive and Fiducial Cross Section Results

The expected and observed event yields after applying all selection criteria are shown in Tab. 15 for all decay channels. Good agreement between data and SM expectations can be observed in all decay channels. Figure 22 shows the invariant mass of the four-lepton system for the  $ZZ^* \rightarrow \ell\ell'\ell'$  selection and the mass of the two-charged-lepton system for the  $ZZ \rightarrow \ell\nu\nu$  selection. Distributions of the four-lepton reconstructed mass for the sum of the  $4e$ ,  $4\mu$ , and  $2e2\mu$  channels and the sum of the  $2\ell 2\tau$  channels for the CMS analysis are shown in Fig. 23.

To include all the final states in the calculation of the cross section, a simultaneous fit to the numbers of observed events in all the decay channels is performed. The fit is constrained by the requirement that all the measurements come from the same initial state via different decay modes.

The joint likelihood is a combination of the likelihoods for the individual channels, which include the signal and background hypotheses. The resulting combined cross sections are compared with theoretical predictions in Tab. 16. The integrated fiducial  $ZZ^{(*)}$  cross sections for different final states are also listed from the ATLAS collaboration. The predicted cross sections are calculated with POWHEGBOX and GG2ZZ [94] for both  $Z$  bosons in the mass range  $66 < m_Z < 116$  GeV. The CMS predictions are calculated with MCFM at

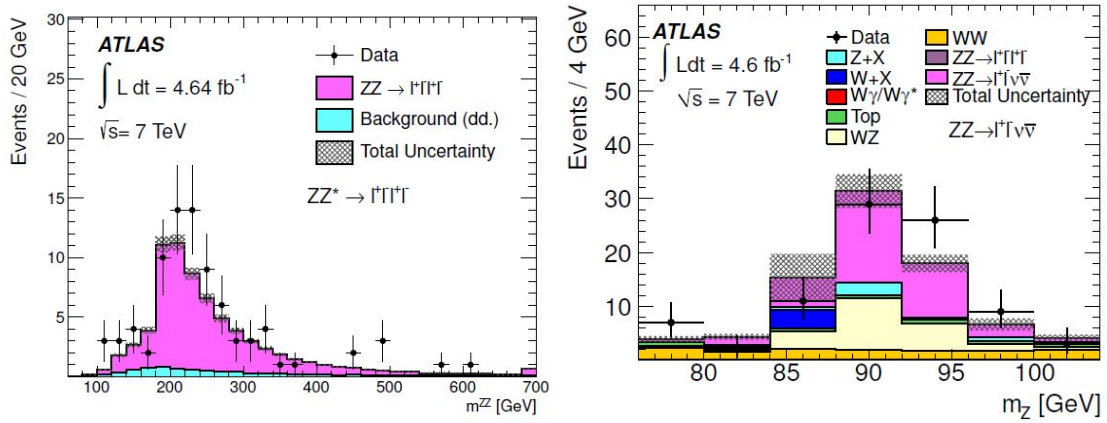


**Figure 22.** Invariant mass  $m^{ZZ}$  of the four-lepton system for the  $ZZ^{(*)} \rightarrow \ell\ell\ell'\ell'$  selection (Left) and mass  $m_Z$  of the two-charged-lepton system for the  $ZZ \rightarrow \ell\ell\nu\nu$  selection for the ATLAS analysis.

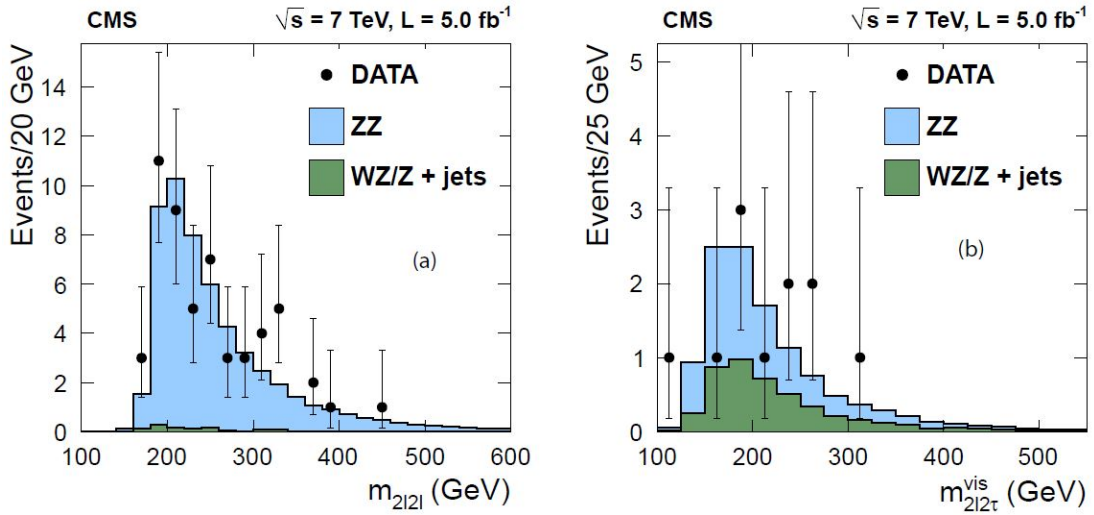


**Figure 23.** Distributions of the four-lepton reconstructed mass for the sum of the  $4e$ ,  $4\mu$ , and  $2e2\mu$  channels (Left) and the sum of the  $2\ell 2\tau$  channels (Right) for the CMS analysis.

NLO for  $q\bar{q} \rightarrow ZZ$  and LO for  $gg \rightarrow ZZ$  for both  $Z$  bosons in the mass range  $60 < m_Z < 120$  GeV.

ATLAS also measured the unfolded differential cross section as a function of the four-lepton invariant mass  $m_{ZZ}$  of the  $ZZ \rightarrow \ell\ell\ell'\ell'$  process and transverse mass  $m_T^{ZZ}$  of the  $ZZ \rightarrow \ell\ell\nu\nu$  process. The results are shown in Fig. 24.

#### 5.1.4 Derived Results and Discussion

Since ATLAS and CMS used different  $Z$  mass requirements for the final reported inclusive cross section measurement, for the combination, we adapt the ATLAS result to the phase space defined by the CMS collaboration (both  $Z$  bosons must have  $60 < m_Z < 120$  GeV).

**Table 15.** Summary of observed  $ZZ \rightarrow \ell\ell\ell'\ell'$ ,  $ZZ^* \rightarrow \ell\ell\ell'\ell'$ ,  $ZZ \rightarrow \ell\nu\nu$  and  $ZZ \rightarrow \ell\ell\tau\tau$  candidates in the data, total background estimates and expected signal for the individual decay modes. The first uncertainty is statistical while the second is systematic. The uncertainty on the integrated luminosity (3.9%) is not included for ATLAS numbers.

	Expected signal	Background	Observed
ATLAS			
$ZZ \rightarrow \ell\ell\ell'\ell'$	$80.9 \pm 1.1 \pm 0.7$	$0.9 \pm 1.1 \pm 0.7$	66
$ZZ^* \rightarrow \ell\ell\ell'\ell'$	$64.4 \pm 0.4 \pm 4.0$	$9.1 \pm 2.3 \pm 1.3$	84
$ZZ \rightarrow \ell\nu\nu$	$39.3 \pm 0.4 \pm 3.7$	$46.9 \pm 4.8 \pm 1.9$	87
CMS			
$ZZ \rightarrow \ell\ell\ell'\ell'$	$53.15 \pm 0.12 \pm 2.96$	$1.35 \pm 0.34 \pm 0.35$	54
$ZZ \rightarrow \ell\ell\tau\tau$	$7.05 \pm 0.04 \pm 0.20$	$4.37 \pm 0.80 \pm 0.29$	11

**Table 16.** Summary of measured and predicted inclusive and fiducial cross sections for the  $ZZ^{(*)}$  process from the ATLAS and CMS collaborations.

	Measured (fb)	Predicted (fb)
ATLAS		
$\sigma_{ZZ \rightarrow \ell^+ \ell^- \ell'^+ \ell'^-}^{fid}$	$25.4^{+3.3}_{-3.0}$ (stat.) $^{+1.2}_{-1.0}$ (syst.) $\pm 1.0$ (lumi.)	$20.9 \pm 0.1$ (stat.) $^{+1.1}_{-0.9}$ (theory)
$\sigma_{ZZ^* \rightarrow \ell^+ \ell^- \ell'^+ \ell'^-}^{fid}$	$29.8^{+3.8}_{-3.5}$ (stat.) $^{+1.7}_{-1.5}$ (syst.) $\pm 1.2$ (lumi.)	$25.6 \pm 0.1$ (stat.) $^{+1.3}_{-1.1}$ (theory)
$\sigma_{ZZ \rightarrow \ell^+ \ell^- \nu\nu}^{fid}$	$12.7^{+3.1}_{-2.9}$ (stat.) $\pm 1.7$ (syst.) $\pm 0.5$ (lumi.)	$12.5 \pm 0.1$ (stat.) $^{+1.0}_{-1.1}$ (theory)
$\sigma_{ZZ}^{tot}$	$6700 \pm 700$ (stat.) $^{+400}_{-300}$ (syst.) $\pm 300$ (lumi.)	$5890^{+220}_{-180}$
CMS		
$\sigma_{ZZ}^{tot}$	$6240^{+860}_{-800}$ (stat.) $^{+410}_{-320}$ (syst.) $\pm 140$ (lumi.)	$6300 \pm 400$

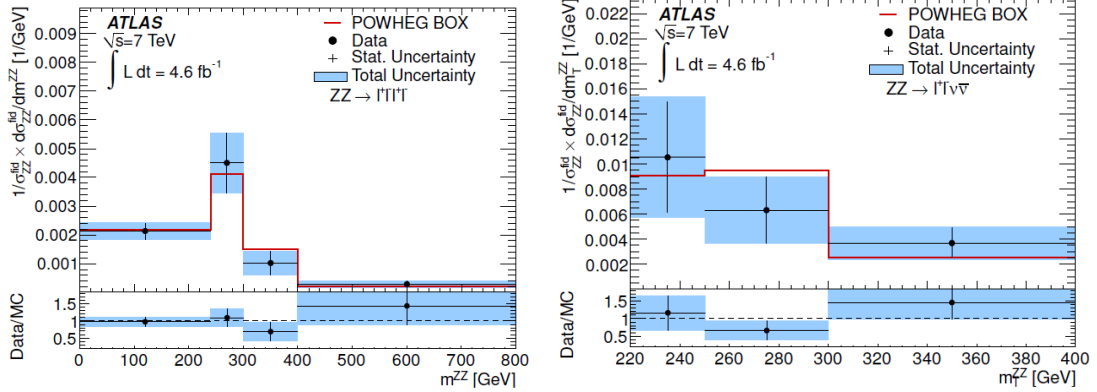


**Figure 24.** Unfolded  $ZZ$  fiducial cross sections in bins of  $m_{ZZ}$  for the  $ZZ \rightarrow \ell\ell\ell'\ell'$  selection and  $m_T^{ZZ}$  for the  $ZZ \rightarrow \ell\nu\nu$  selection.

The CMS predicted theoretical cross section number is used and the ATLAS measured inclusive cross section number is scaled up by 7%. The overall uncertainty is dominated

by statistical uncertainty for both measurements which are treated independently. The uncertainties on the integrated luminosity are fully correlated between the two experiments. Other major contributors to systematic uncertainties are those due to lepton and jet identification, jet-energy and jet-resolution, and also in the  $Z$ +jets data-driven background estimation. These uncertainties are treated as uncorrelated between the two experiments. Using the BLUE method, the combined inclusive cross section is found to be

$$\sigma(pp \rightarrow ZZ) = 6727 \pm 682(\text{stat.}) \pm 400(\text{syst.}) \text{ fb},$$

which is consistent with a theoretical prediction of  $6300 \pm 400$  fb. The fiducial cross section measurements for  $ZZ^{(*)} \rightarrow \ell\ell'\ell'$  and  $ZZ \rightarrow \ell\ell\nu\nu$  are not combined into a common fiducial phase space due to their very different detector signatures.

## 5.2 $Z\gamma$ Analysis

In the SM, the  $Z$  boson cannot directly emit a photon. Hence the study of the  $pp \rightarrow Z\gamma$  process allows a precise test of this prediction. Both ATLAS and CMS collaborations have measured the production cross section in the  $Z \rightarrow \ell\ell(\ell = e, \mu)$  and  $Z \rightarrow \nu\bar{\nu}$  decay channels [90, 91].

### 5.2.1 Event Selection

For the ATLAS  $Z\gamma \rightarrow \ell\ell\gamma$  analysis, lepton and photon identification criteria are exactly the same as used in the  $W\gamma$  analysis. The  $Z\gamma$  candidates are selected by requiring exactly two oppositely charged same-flavor leptons with an invariant mass greater than 40 GeV and one isolated photon with  $E_T > 15$  GeV. The  $\nu\bar{\nu}$  candidates are selected by requiring one isolated photon with  $E_T > 100$  GeV and  $E_T^{\text{miss}} > 90$  GeV. The reconstructed photon,  $E_T^{\text{miss}}$ , and jets are required to be well separated in the transverse plane in order to reduce the  $\gamma$ +jet background. Events with identified electrons and muons are vetoed to reject  $W$ +jets and  $W\gamma$  background. The selection criteria to identify the electrons and muons are the same as in the  $Z(\ell\ell)\gamma$  analysis. ATLAS also measured the cross sections for events with and without the requirement of zero jets in each event. Jets are required to have  $E_T > 30$  GeV and  $|\eta| < 4.4$ .

Similar event selection criteria are used for the CMS  $Z\gamma \rightarrow \ell\ell\gamma$  analysis except lepton candidates are required to have  $p_T > 20$  GeV and the invariant mass of the two leptons is required to satisfy  $m_{\ell\ell} > 50$  GeV. The  $\nu\bar{\nu}$  candidates are selected by requiring one isolated photon with  $E_T > 145$  GeV and  $E_T^{\text{miss}} > 130$  GeV. Only photons reconstructed in the barrel EM calorimeter region ( $|\eta| < 1.4$ ) are used. Events are vetoed if they contain other particles of significant energy or momentum.

### 5.2.2 Background Estimation

The main background to the  $\ell\ell\gamma$  signal originates from events with  $Z$ +jets where jets are misidentified as photons. Background to the  $\nu\bar{\nu}\gamma$  signal originates mainly from  $W(e\nu)$  events when the electron is misidentified as a photon,  $Z(\nu\bar{\nu})$ +jets and multijet events when one of the jets in the event is misidentified as a photon, and  $\tau\nu\gamma$  and  $\ell\nu\gamma$  events from  $W\gamma$

**Table 17.** Summary of the  $Z\gamma \rightarrow \ell\ell\gamma$  and  $Z\gamma \rightarrow \nu\nu\gamma$  selection cuts used by the ATLAS and CMS collaborations.

	ATLAS	CMS
$Z\gamma \rightarrow \ell\ell\gamma$ ( $\ell' = e, \mu$ )	Combined muons with $p_T > 25$ GeV	Muons with $p_T > 20$ GeV
	Combined electrons with $E_T > 25$ GeV	Electrons with $p_T > 20$ GeV
	Photon $E_T > 15$ GeV and $E_T^{\Delta R < 0.3} < 6$ GeV	Photon $E_T > 15$ GeV, isolation and shower-shape requirements
	$m_{\ell\ell} > 40$ GeV	$m_{\ell\ell} > 50$ GeV
	$\Delta R(\ell, \gamma) > 0.7$	$\Delta R(\ell, \gamma) > 0.7$
$Z\gamma \rightarrow \nu\nu\gamma$	Photon $E_T > 100$ GeV and $E_T^{\Delta R < 0.3} < 6$ GeV	Photon $E_T > 145$ GeV, $ \eta  < 1.4$ , isolation and shower-shape requirements
	$E_T^{\text{miss}} > 90$ GeV	$E_T^{\text{miss}} > 130$ GeV
	$\Delta\phi(E_T^{\text{miss}}, \gamma) > 2.6$ and $\Delta\phi(E_T^{\text{miss}}, \text{jet}) > 0.4$	
	Veto events with rec. leptons	Veto events with rec. leptons and jets

production when the  $\tau$  decays into hadrons or when the electron or muon from  $\tau$  or  $W$  decay is not reconstructed, and  $\gamma$ + jets events when large  $E_T^{\text{miss}}$  is created by a combination of real  $E_T^{\text{miss}}$  from neutrinos in heavy quark decays and mismeasured jet energy.

For the  $\ell\ell\gamma$  analysis, ATLAS used a sideband method similar to the one used for the  $W\gamma$  analysis to estimate the  $Z$ + jets contamination. For the  $\nu\bar{\nu}\gamma$  analysis, the sideband method is also used to estimate the  $Z(\nu\bar{\nu})$ + jets and multijet background. A similar method using the probability of electrons to be misidentified as photons is used to derive the  $W(e\nu)$  background. The  $\gamma$ + jets contamination is estimated using a semi-data-driven method. A sample is selected by applying all signal region selection criteria except for requiring  $\Delta\phi(E_T^{\text{miss}}) < 0.4$ . By requiring the  $E_T^{\text{miss}}$  direction to be close to the jet direction, the selected events in the control region are dominated by  $\gamma$ + jets background. The yield of  $\gamma$ + jets events obtained in control regions is then scaled by an extrapolation factor to predict the  $\gamma$ + jets background yield in the signal region, where the extrapolation factor is taken from a  $\gamma$ + jets MC sample. The  $\tau\nu\gamma$  and  $\ell\nu\gamma$  background is estimated using MC simulation.

For the  $\ell\ell\gamma$  analysis, CMS also chose to perform a template fit to the photon  $\sigma_{\eta\eta}$  distribution in data to determine the  $Z$ + jets contamination. For the  $\nu\bar{\nu}\gamma$  analysis, the background from misidentified photons originating in jet fragmentation and decay processes is estimated by constructing a control data sample enriched with multijet events. This sample is then used to calculate a misidentification ratio, defined as the number of events where the photon candidate satisfies the signal selection criteria to the number of events where the photon candidate satisfies looser selection criteria but fails the isolation condition. The background contribution due to misidentified jets is then estimated from the multiplication of the misidentification ratio and the number of events in the signal data sample that pass the photon selection criteria but fail the isolation requirements. The  $W(e\nu)$  background is estimated using a similar method to that used by ATLAS. All other backgrounds are estimated from MC simulation.



### 5.3 Cross Section Results

The expected and observed event yields after applying all selection criteria are shown in Tab. 18 for all decay channels. The combined photon  $ll\gamma$  invariant mass distribution for all selected  $ll\gamma$  candidate events and the photon transverse energy distribution for all selected  $\nu\bar{\nu}\gamma$  candidate events are shown in Fig. 25 for the ATLAS analysis. The photon transverse energy distribution is shown separately for the electron and muon decay channels in Fig. 26 for the CMS  $ll\gamma$  analysis. Reasonable agreement between the data and expected signal and background contributions are observed from each experiment.

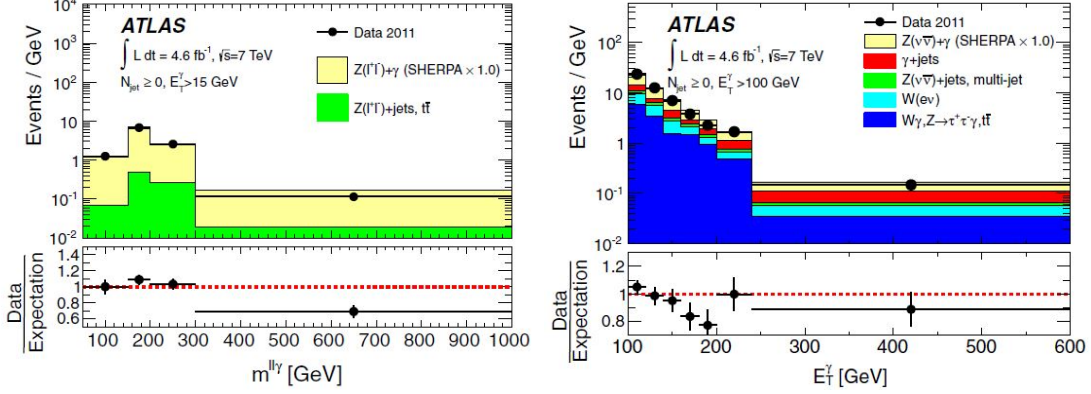


**Figure 25.** Combined distributions for  $ll\gamma$  candidate events in the electron and muon channels of the  $ll\gamma$  invariant mass (Left) for the ATLAS  $pp \rightarrow Z\gamma \rightarrow ll\gamma$  analysis and the photon transverse energy for the ATLAS  $pp \rightarrow Z\gamma \rightarrow \nu\bar{\nu}\gamma$  analysis.

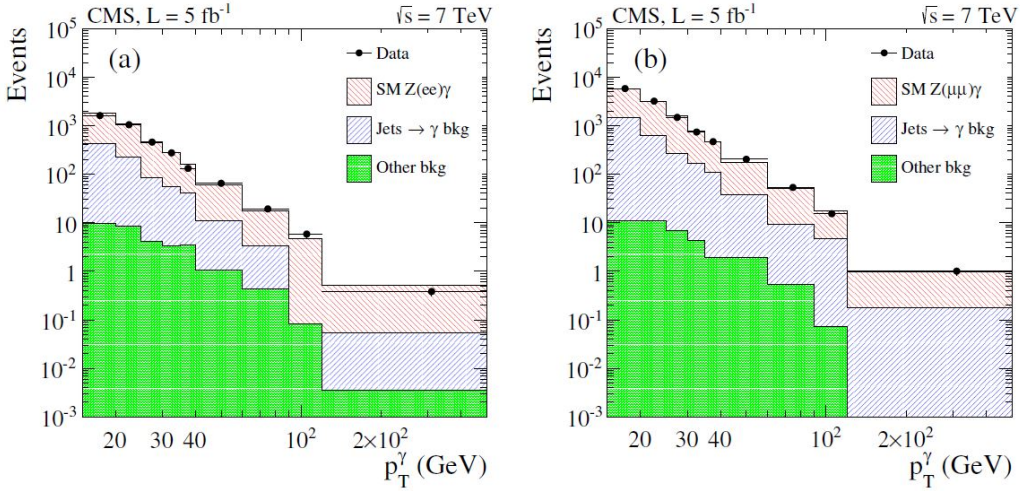


**Figure 26.** CMS distributions of  $p_T^\gamma$  for  $ll\gamma$  candidate events in data, with signal and background MC simulation contributions to  $Z\gamma \rightarrow ee\gamma$  (Left) and  $Z\gamma \rightarrow \mu\mu\gamma$  (Right).

For the  $Z\gamma \rightarrow ll\gamma$  analysis, ATLAS measured the production cross section in an extended fiducial region defined as two leptons with  $p_T > 25$  GeV and  $|\eta| < 2.47$ , dilepton



**Table 18.** Summary of observed  $Z\gamma$  candidates in the data, total background estimates and expected signal for the individual decay modes. The first uncertainty is statistical while the second is systematic.

	Decay channel	Expected signal	Background	Observed
ATLAS	$ee\gamma$	$1600 \pm 71 \pm 68$	$311 \pm 57 \pm 68$	1908
	$\mu\mu\gamma$	$2390 \pm 97 \pm 73$	$366 \pm 83 \pm 73$	2756
	$\nu\bar{\nu}\gamma$	$420 \pm 42 \pm 60$	$670 \pm 27 \pm 60$	1094
CMS	$ee\gamma$	$3160 \pm 80 \pm 90$	$950 \pm 50 \pm 40$	4108
	$\mu\mu\gamma$	$5030 \pm 100 \pm 1210$	$1424 \pm 60 \pm 80$	6463
	$\nu\bar{\nu}\gamma$	$45.3 \pm 6.9$	$30.2 \pm 6.5$	73

invariant mass  $m_{\ell\ell} > 40$  GeV, photon  $E_T > 15$  GeV, and  $\Delta R(\ell, \gamma) > 0.7$ . CMS measured the production cross section in an extended fiducial region defined as photon  $p_T > 15$  GeV,  $\Delta R(\ell, \gamma) > 0.7$  and  $m_{\ell\ell} > 50$  GeV. For the  $Z\gamma \rightarrow \nu\bar{\nu}\gamma$  analysis, ATLAS measured the production cross section in an extended fiducial region defined as  $p_T^{\nu\bar{\nu}} > 90$  GeV and photon  $E_T > 100$  GeV, while CMS measured the production cross section in an extended fiducial region defined as photon  $E_T > 145$  GeV and  $|\eta| < 1.4$ . The measured and predicted cross sections are listed in Tab. 19. ATLAS also measured the unfolded differential cross section as a function of the photon  $E_T$  of the  $Z\gamma \rightarrow \ell\ell\gamma'$  process. The results are shown separately for the inclusive ( $N_{jet} \geq 0$ ) and exclusive ( $N_{jet} = 0$ ) fiducial regions.

**Table 19.** Summary of the measured and predicted  $W\gamma \rightarrow \ell\nu\gamma$  cross sections from the ATLAS and CMS collaborations. Different fiducial regions are defined by the ATLAS and CMS collaborations.

	Measured (pb)	Predicted (pb)
ATLAS		
$\sigma_{Z\gamma \rightarrow \ell\ell\gamma}^{fid} (N_{jet} \geq 0)$	$1.31 \pm 0.02$ (stat.) $\pm 0.11$ (syst.) $\pm 0.05$ (lumi.)	$1.18 \pm 0.05$
$\sigma_{Z\gamma \rightarrow \nu\nu\gamma}^{fid} (N_{jet} \geq 0)$	$0.133 \pm 0.013$ (stat.) $\pm 0.020$ (syst.) $\pm 0.005$ (lumi.)	$0.156 \pm 0.012$
$\sigma_{Z\gamma \rightarrow \ell\ell\gamma}^{fid} (N_{jet} = 0)$	$1.05 \pm 0.02$ (stat.) $\pm 0.10$ (syst.) $\pm 0.04$ (lumi.)	$1.06 \pm 0.05$
$\sigma_{Z\gamma \rightarrow \nu\nu\gamma}^{fid} (N_{jet} = 0)$	$0.116 \pm 0.010$ (stat.) $\pm 0.013$ (syst.) $\pm 0.004$ (lumi.)	$0.115 \pm 0.009$
CMS		
$\sigma_{Z\gamma \rightarrow \ell\ell\gamma}^{fid}$	$5.33 \pm 0.08$ (stat.) $\pm 0.25$ (syst.) $\pm 0.12$ (lumi.)	$5.45 \pm 0.27$
$\sigma_{Z\gamma \rightarrow \nu\nu\gamma}^{fid}$	$0.0211 \pm 0.0042$ (stat.) $\pm 0.0043$ (syst.) $\pm 0.0005$ (lumi.)	$0.0219 \pm 0.0011$

ATLAS measured the differential cross section as a function of the photon  $E_T$  using combined electron and muon measurements in the inclusive ( $N_{jet} \geq 0$ ) and exclusive ( $N_{jet} = 0$ ) fiducial regions. CMS measured the  $Z\gamma$  production cross section for three different photon  $E_T$  thresholds (15 GeV, 60 GeV, and 90 GeV). The measured cross sections are compared with several theoretical predictions as shown in Fig. 27.

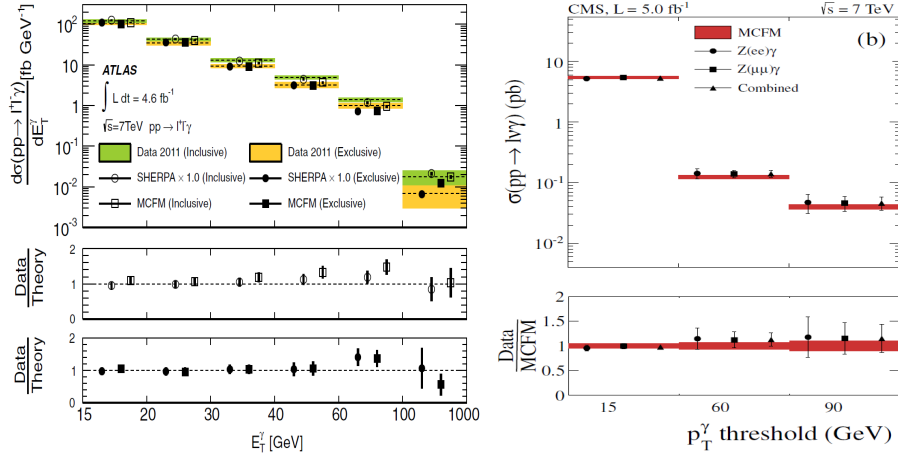


**Figure 27.** Left: Measured photon  $E_T$  differential cross section of the  $Z\gamma \rightarrow \ell\ell\gamma$  process, using combined electron and muon measurements in the inclusive ( $N_{jet} \geq 0$ ) and exclusive ( $N_{jet} = 0$ ) fiducial regions. Right: Measured  $Z\gamma$  cross sections for three photon  $E_T$  thresholds, compared to SM predictions.

### 5.3.1 Derived Results and Discussion

Since ATLAS and CMS measured the  $Z\gamma \rightarrow \ell\ell\nu\gamma$  and  $Z\gamma \rightarrow \nu\nu\gamma$  cross sections in different phase spaces, for the cross section combination, we choose the phase space defined by the CMS collaboration for  $Z\gamma \rightarrow \ell\ell\nu\gamma$  and the phase space defined by the ATLAS collaboration for  $Z\gamma \rightarrow \nu\nu\gamma$ . The ATLAS measured  $Z\gamma \rightarrow \ell\ell\gamma$  cross section is scaled up by  $4.6 \pm 0.1$ , and the CMS measured  $Z\gamma \rightarrow \nu\nu\gamma$  cross section value is scaled up by  $7.1 \pm 0.2$ . The statistical uncertainties for both measurements are treated independently. The uncertainties on the integrated luminosity are treated as fully correlated. Other systematic uncertainties are dominated by uncertainties related to the  $Z$ +jets data-driven background estimation, lepton and photon identification, and energy and resolution. These uncertainties are treated as fully uncorrelated between the two experiments. Using the BLUE method, the combined inclusive cross section is found to be

$$\sigma(pp \rightarrow Z\gamma \rightarrow \ell\ell\gamma) = 5.45 \pm 0.07 \text{ (stat.)} \pm 0.27 \text{ (sys.) fb,}$$

and

$$\sigma(pp \rightarrow Z\gamma \rightarrow \nu\nu\gamma) = 0.137 \pm 0.011 \text{ (stat.)} \pm 0.021 \text{ (sys.) fb.}$$

The corresponding predicted cross section in each fiducial region is  $5.45 \pm 0.27$  fb and  $0.156 \pm 0.012$  fb respectively.

## 6 Interpretation of Results and Outlook

### 6.1 Inclusive Cross Section Measurements

Several inclusive cross section measurements are not longer statistically limited and the associated systematic uncertainties are at percent level. The measured cross sections are

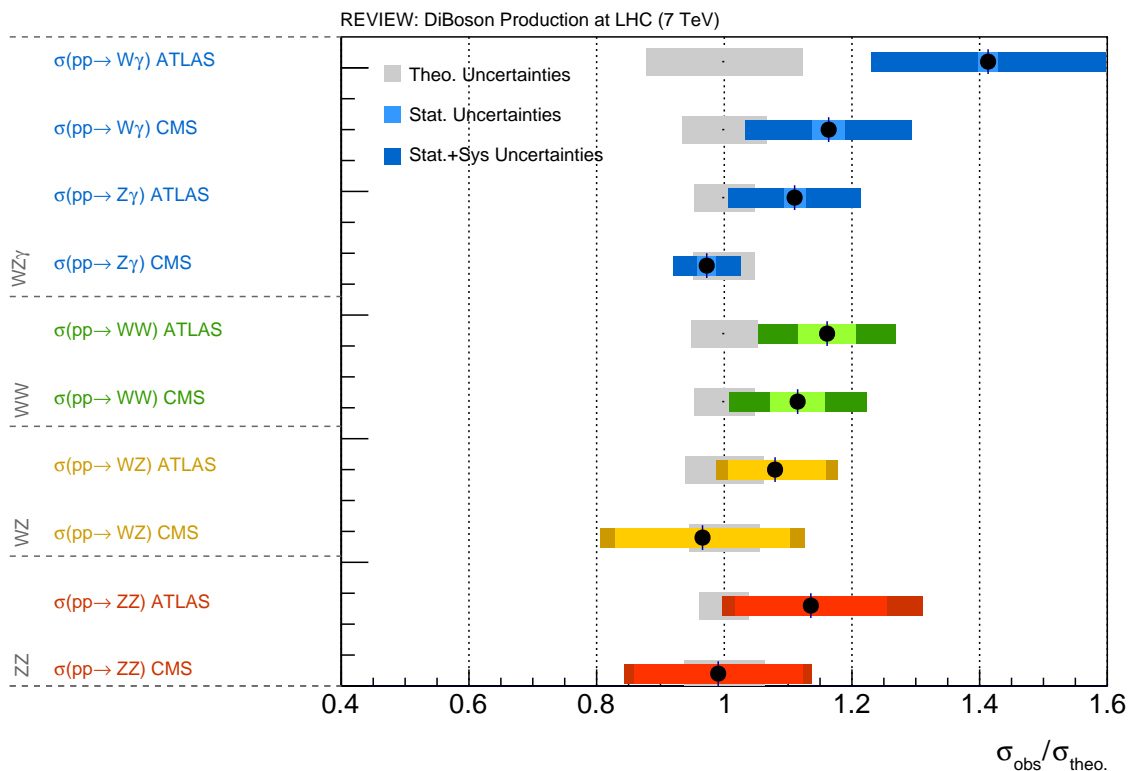


**Figure 28.** Summary of cross sections for different diboson production processes. Shown is the ratio between data and predictions. The grey bands represent the theory uncertainties, the light colored bands are the statistical uncertainties and the dark colored bands the combined statistical and systematic uncertainties.

compatible between the two experiments. Their combination, which have been derived in the Sect. 4 and 5, lead to a reduction of the overall experimental uncertainties by 20–30%. On the theoretical side, the SM predictions of the diboson cross sections are known to NLO and NNLO in  $\alpha_s$  (see Sect. 2.3). A comparison between theoretical predictions and measured and combined cross sections from both experiments is illustrated in Fig. 28. All results are compatible with the theoretical expectation within the statistical and systematic uncertainties.

In addition to the inclusive cross-section measurements, the ATLAS collaboration also published normalized differential cross section of various diboson final states. Also here, a good agreement between theoretical predictions and the measurements can be observed. However, the measured differential cross sections are still dominated by statistical uncertainties and a stringent test of these distributions is yet to come.

In summary, the good agreement between theory and experiment for the inclusive and differential diboson production cross sections is an impressive confirmation of the perturbative QCD calculations rather than a precise test of the electroweak gauge group structure,

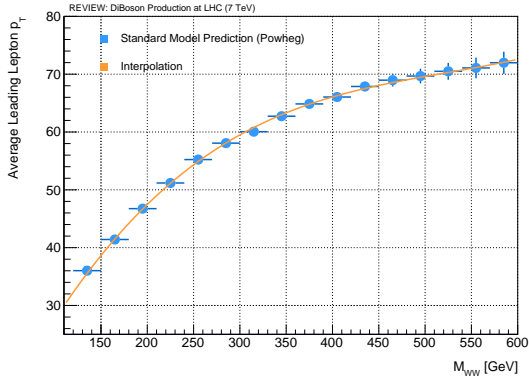


**Figure 29.** Correlation between the invariant mass of the  $W^+W^-$  system and the leading lepton transverse momentum.

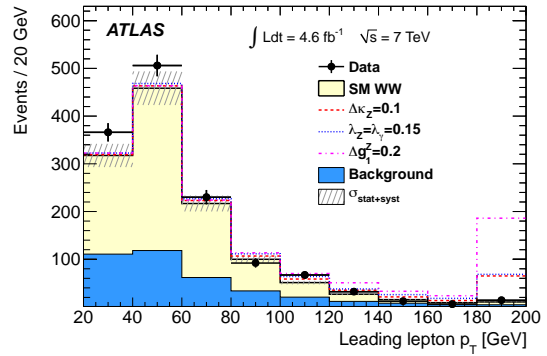


**Figure 30.** The reconstructed leading lepton  $p_T$  spectrum in data and sum of MC signal and background for the SM prediction and for three different anomalous TGC predictions. The right-most bin shows the sum of all events with the leading lepton  $p_T$  above 180 GeV.

as deviations from the latter only affect the high energetic tails of the measured phase space.

## 6.2 Limits on Anomalous Triple Gauge Couplings

The theoretical basis of aTGCs and their effect on the diboson production cross sections is introduced in Sect. 2.5. In the presence of non-zero aTGCs, the production cross section in the  $s$ -channel is enhanced. This enhancement increases with the center-of-mass energy, leading to an increase in the inclusive production cross section, and also to a change of the shape of the differential cross section. Observables which probe high center-of-mass energies are therefore of particular importance for the study of aTGCs.

If available, the full invariant mass of the diboson system can be taken as observable for aTGC studies. However, this is not available for final states which involve a  $W$  boson as the decay neutrino does not allow for a full kinematic reconstruction. The transverse momentum of the leading (highest  $p_T$ ) lepton and the reconstructed transverse momentum of the  $W$  boson can be used as sensitive variables in case of the  $WW$  and  $WZ$  analyses, respectively. The correlations between the leading lepton  $p_T$  in the  $WW$  final state with the center-of-mass energy  $\hat{s} = m_{WW}$  is shown in Fig. 29.

Since no deviations from SM expectations were observed, the measured distributions have been used to derive limits on aTGCs. This has been done on reconstruction level where the expected signal yields are compared to data. MC event generators such as MC@NLO or BHO [18] are used to generate events for a chosen set of aTGCs. These MC samples are then used in a second step to reweight a fully simulated and reconstructed standard model MC sample. As an example, the reconstructed leading lepton transverse momentum of a  $WW$  process is shown in Figure 30. Several predictions of this distributions for different aTGCs scenarios are also shown.

A maximum likelihood fit is performed in order to derive a 95% confidence limit on aT-

GCs. The likelihood  $L$  is defined as a product of Poisson probability distribution functions for the observed number of events  $N_{obs}^i$  and the number of expected signal and background events ( $N_{exp}^i$ ) for each bin  $i$  of the reconstructed distribution:

$$L = \prod_{i=1}^n \frac{e^{-N_{exp}^i} (N_{exp}^i)^{N_{obs}^i}}{N_{obs}^i!}$$

This likelihood is evaluated for one one varying aTGC parameter, while all other aTGC parameters are kept at zero, and the corresponding 95% confidence limits are derived. CMS published aTGC limits without any usage of form factors, while ATLAS derived limits with and without form factors. The cut-off scale in the ATLAS analyses is chosen to match the energy at which the unitarity is still preserved.

As previously discussed, the  $WWZ$  and  $WW\gamma$  vertices can be studied by the  $WW$ ,  $WZ$  and  $W\gamma$  final states. Both ATLAS and CMS experiments derived aTGC limits using the transverse momentum of the leading lepton in the  $WW$  final state. CMS published limits only based on the LEP scenario [84], while ATLAS provided limits assuming the LEP scenario, the equal coupling assumptions, the HISZ assumptions and no further constraints [83]. Limits on aTGCs via the  $WZ$  analysis are available from the ATLAS collaboration [88] and are based on the study of the transverse momentum spectrum of the  $Z$  boson. Both experiments derived limits via the  $W\gamma$  final state [90, 91] using the measured energy of the final state photon. A summary on aTGC parameters involving the  $WWZ$  and  $WW\gamma$  without form factors is given in Tab. 20 and illustrated in Fig. 31. The results from the  $WW$  analyses provide the most sensitive limits assuming defined relationships between the couplings. For unconstrained limits, the  $WZ$  and  $W\gamma$  analyses lead to significant improvements on the relevant coupling parameters. The effect of a form factor on the observed limits varies from a degradation of 10% for the  $WW$  analysis with a cut-off scale of  $\Lambda = 6$  TeV, to 30% for the  $WZ$ -analysis with  $\Lambda = 2$  TeV.

The  $\gamma ZZ$  and the  $\gamma\gamma Z$  vertex are forbidden in the SM and are studied using the  $ZZ$  and  $Z\gamma$  final states, respectively. In the  $ZZ$  analyses, CMS used the invariant mass of the four-lepton system [93], while ATLAS uses the transverse momentum of the  $Z$  boson to derive limits on aTGCs [92]. Both experiments used the transverse energy of the photon in the  $Z\gamma$  channel for the limit extraction [90, 91]. A summary of the derived limits assuming no form factors is given in Tab. 20 and illustrated in Fig. 31. The given limits degrade by 30% to 150% with  $\Lambda = 3$  TeV for the  $ZZ$  analyses and with  $\Lambda = 2$  TeV for the  $Z\gamma$  analyses, respectively. The limits on the  $ZZV$  and  $Z\gamma V$  vertices are partly comparable between the two experiments, where the limits on the  $ZZ\gamma$  and  $Z\gamma\gamma$  couplings are driven by the analyses of the  $Z\gamma \rightarrow \nu\nu\gamma$  process. However, CMS achieves significantly more stringent exclusion limits on  $h_V^3$  and  $h_V^4$ , which is due to an optimized binning of the sensitive signal region.

As discussed in Sect. 2.5, the present limits depend on various theoretical assumptions, thus it will be difficult to reinterpret those limits in the future when new theoretical models are proposed. One possibility to overcome those constraints is the publication of the production cross sections in sensitive regions of the phase space, which in turn can be easily used to derive limits on various theoretical scenarios. Those published cross sections

**Table 20.** Summary of the observed 95% confidence exclusion limits on anomalous couplings on the  $WWV$  vertex, assuming the LEP scenario and also with no further assumptions for the ATLAS and CMS experiment. Except for the coupling under study, all other anomalous couplings are set to zero. The results are shown for an energy cut-off scale  $\Lambda = \infty$ , i.e. no form factor has been used. The limits marked with (\*) are derived by the authors by assuming perfect error ellipses, that describe the published results of the experiments.

	ATLAS	CMS	Final State	Assumptions
$\Delta\kappa_Z$	[-0.043, 0.043]	([-0.091, 0.091]*)	$WW$	LEP
	[-0.078, 0.092]		$WW$	-
	[-0.37, 0.57]		$WZ$	-
$\lambda_Z$	[-0.062, 0.059]	[-0.048, 0.048]	$WW$	LEP
	[-0.074, 0.073]		$WW$	-
	[-0.046, 0.047]		$WZ$	-
$\lambda_\gamma$	[-0.062, 0.059]	[-0.048, 0.048]	$WW$	LEP
	[-0.152, 0.146]		$WW$	-
	[-0.060, 0.060]	[-0.050, 0.037]	$W\gamma$	-
$\Delta g_1^Z$	[-0.039, 0.052]	[-0.095, 0.095]	$WW$	LEP
	[-0.373, 0.562]		$WW$	-
	[-0.057, 0.093]		$WZ$	-
$\Delta\kappa_\gamma$	([-0.20, 0.20]*)	[-0.21, 0.22]	$WW$	LEP
	[-0.135, 0.190]		$WW$	-
	[-0.33, 0.37]	[-0.38, 0.29]	$W\gamma$	-

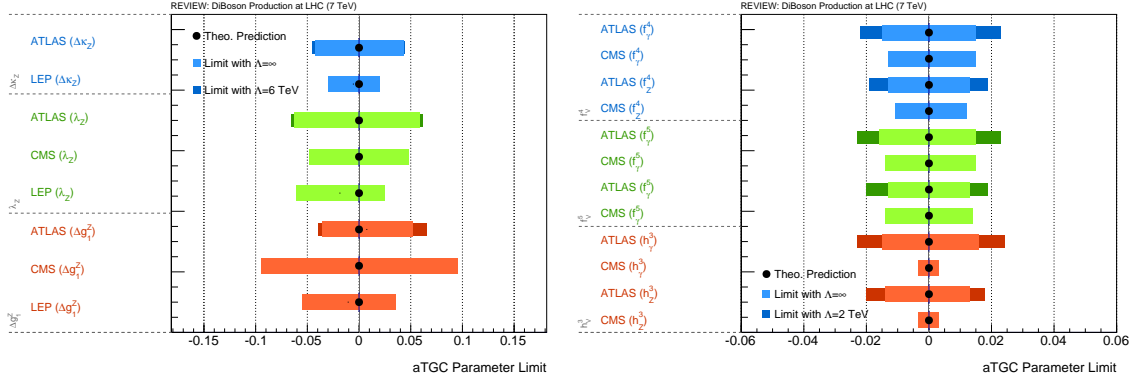


**Figure 31.** Illustration of the observed 95% confidence exclusion limits on anomalous couplings on the  $WWV$  (left), the  $ZZV$  and the  $Z\gamma V$  vertex (right) from ATLAS, CMS and the LEP experiments. The limits on the  $WWV$  are based on the LEP scenario. Except for the coupling under study, all other anomalous couplings are set to zero. The results are shown with an energy cut-off scale  $\Lambda = \infty$  (i.e. no form factor), and if applicable with  $\Lambda = 2 - 3$  GeV. The limits on  $h_V^4$  are too small to be shown in this Figure.

are model independent to a high extend and do not require any further knowledge on the detector. Examples of such cross sections are derived in Sect. 4 and 5.

In order to test the usefulness of this approach, we compare the derived limits on the  $WWV$  vertex based on the reconstructed lepton  $p_T$  distribution to the limits obtained

**Table 21.** The summary of the observed 95% C.L. on anomalous couplings on the  $ZZV$  and  $Z\gamma V$  vertex for the ATLAS and CMS experiment. Except for the coupling under study, all other anomalous couplings are set to zero. The results are shown an energy-cut of scale  $\Lambda = \infty$ , i.e. no form factor has been used.

	ATLAS	CMS	Final State
$f_\gamma^4$	[-0.015, 0.015]	[-0.013, 0.015]	$ZZ$
$f_Z^4$	[-0.013, 0.013]	[-0.011, 0.012]	$ZZ$
$f_\gamma^5$	[-0.016, 0.015]	[-0.014, 0.015]	$ZZ$
$f_Z^5$	[-0.013, 0.013]	[-0.014, 0.014]	$ZZ$
$h_\gamma^3$	[-0.015,0.016]	[-0.0032, 0.0032]	$Z\gamma$
$h_Z^3$	[-0.013,0.015]	[-0.0032, 0.0032]	$Z\gamma$
$h_\gamma^4$	[-0.000094,0.000092]	[-0.000016, 0.000016]	$Z\gamma$
$h_Z^4$	[-0.000087,0.000087]	[-0.000014, 0.000014]	$Z\gamma$

using the published differential cross sections. In a first step, we use the MCFM generator to predict the production cross sections for one aTGC parameter ( $\lambda_Z$  in this case) in the fiducial phase space defined in Sect. 4.1.4 for the leading lepton  $p_T$  between 140 GeV and 350 GeV. All other couplings are set to their SM values. In a second step, we compare the predicted cross sections for different  $\lambda_Z$  with the measured fiducial cross section in this phase space region of  $24 \pm 10$  fb. This leads to a limit of  $[-0.13, 0.13]$ , which is weaker by approximately 60%. This degradation is due to the fact that the ATLAS limit derivation is based on the full reconstructed spectra, i.e. uses the full leading lepton  $p_T$  shape information. However, the advantages of the limit derivation via fiducial cross sections remain and should be taken as a valid alternative option for future measurements.

### 6.3 Outlook on Quartic Gauge Coupling Measurements

We have concentrated on TGC studies in the above sections. Even though the available data from the LHC run in 2010 and 2011 are not sufficient to measure quartic gauge couplings (QGCs), first sensitivity studies showing the potential of the upcoming LHC results have been made available. The SM predicts four-point vertices between electroweak gauge bosons, described in Eqn. 2.1 by the term  $\mathcal{L}_{WWVV}$ . The highest cross section at the LHC is expected for the  $WW\gamma\gamma$  vertex, which can be studied in the reaction  $pp \rightarrow pW^+W^-p$  with a subsequent leptonic decay of the  $W$  boson. A schematic sketch of the involved processes is shown in Fig. 5.

The fully exclusive (“elastic”) scattering is theoretically well understood and can be modeled for example by the CALHEP [95] program. The production cross section is 1.2 fb, taking into account the leptonic branching ratios of the  $W$  boson. The same process with a similar final state can also be induced by inelastic scattering, in which one or even both protons dissociate into a low-mass system which also escapes the detection. The inelastic scattering is theoretically less well known due to strong interactions between the proton remnants (rescattering) which produce additional hadronic activity. The LO diagrams for the  $\gamma\gamma \rightarrow W^+W^-$  interactions are shown in Fig. 32. Two TGC vertices are present in the  $t$ - and  $u$ -channels, while the quartic couplings only appear in the  $s$ -channel.



The experimental signature of these processes are two high energetic, charged leptons from the  $W$  boson decay and two forward scattered protons beyond the acceptance of the detector. The dilepton system is expected to have large invariant mass and large transverse momentum. In addition, only two tracks from a common vertex are expected. Additional tracks would indicate further hadronic activity which is not expected in the  $\gamma\gamma \rightarrow W^+W^-$  process.

The main background processes are the inclusive  $pp \rightarrow W^+W^-$  production, the inclusive  $Z$  boson production with a leptonic decay, and the two photon process  $\gamma\gamma \rightarrow \ell^+\ell^-$  as shown in Fig. 33. While the first two are expected to have additional tracks associated with the production vertex, the latter process is produced in a similar way to the signal. The two photon processes have an order of magnitude times larger cross section than the signal process.

The CMS experiment has analyzed  $5 \text{ fb}^{-1}$  of data to search for the evidence of the  $\gamma\gamma \rightarrow W^+W^-$  process [96]. In order to achieve a clean signal selection, only the  $e^\pm\mu^\mp$  decay channel has been used. The requirement of two different flavor leptons greatly reduces the background contribution from the  $\gamma\gamma \rightarrow \ell^+\ell^-$  process. Signal candidates are selected by requiring two oppositely-charged leptons ( $e, \mu$ ) with  $p_T > 20 \text{ GeV}$  and  $|\eta| < 2.4$ . The two leptons must origin from a common vertex and with no other reconstructed tracks associated to the production vertex. The dilepton system is required to have  $m_{e\mu} > 20 \text{ GeV}$  and  $p_T(e\mu) > 30 \text{ GeV}$ . The corresponding signal selection efficiency is 10.6%.

Since the theoretical prediction for the proton dissociation contribution to the signal is not well known, CMS used a data-driven method to estimate the contribution from this background source. The method is based on the assumption that the process  $\gamma\gamma \rightarrow \ell^+\ell^-$  has the same probability of being produced by elastic and inelastic  $pp$  scattering as by the signal process. By studying the  $pp \rightarrow \mu^+\mu^-$  final state, which is dominated by the  $\gamma\gamma \rightarrow \mu^+\mu^-$  process, a correction factor  $F$  using events with  $m_{\mu^+\mu^-} > 160 \text{ GeV}$  is estimated. This correction factor is calculated as the number of observed dimuon events corrected for the contribution from the inclusive Drell-Yan process divided by the number of predicted events from a pure elastic scattering process. The corresponding dimuon invariant mass distribution is shown in Fig. 34. A significant undershoot of data is seen for large invariant masses, which is the dissociation region mostly affected by rescattering effects. The factor  $F$  is found to be  $3.23 \pm 0.53$  and is used to scale the predicted cross section for the  $\gamma\gamma \rightarrow W^+W^- \rightarrow e^\pm\nu\mu^\mp\nu$  process.

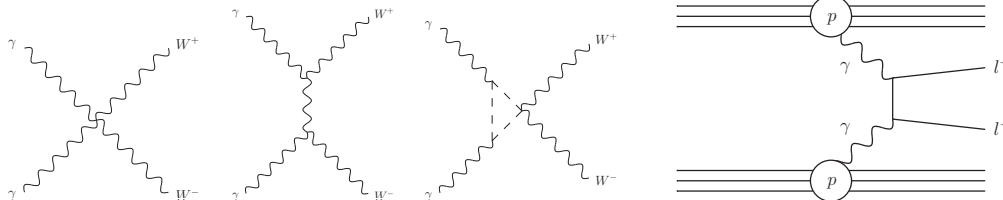


**Figure 32.** LO Feynman diagrams for the  $\gamma\gamma \rightarrow W^+W^-$  production. **Figure 33.** LO Feynman diagram for  $\gamma\gamma \rightarrow \ell^+\ell^-$ .

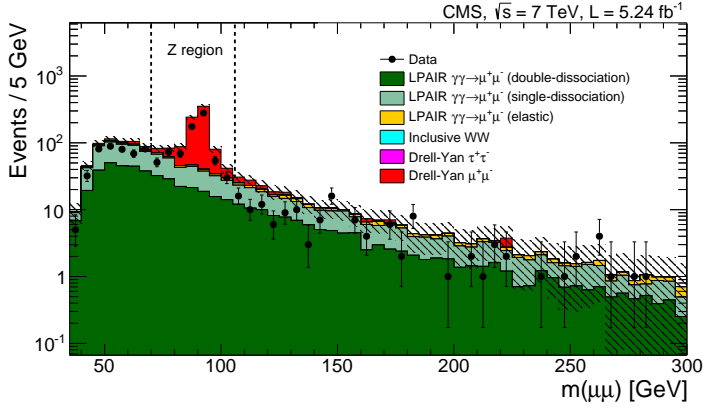


**Figure 34.** Invariant mass distribution of the muon pairs for the dissociation selection. The dashed lines indicate the  $Z$ -peak region. The hatched bands indicate the statistical uncertainty in the simulation.

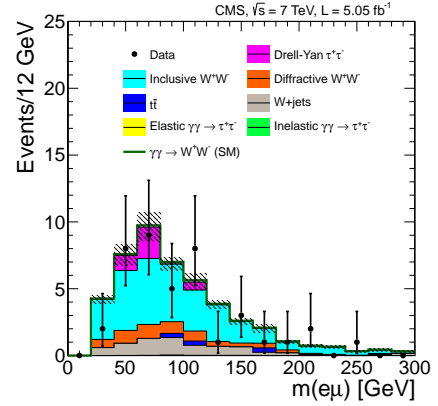


**Figure 35.** The  $e^\pm\mu^\mp$  invariant mass distribution for events with 1 – 6 extra tracks on the vertex.

The total predicted signal cross section times branching ratio is found to be  $\sigma(pp \rightarrow pW^+W^-p \rightarrow pe^\pm\nu\mu^\mp\nu p) = 4.0 \pm 0.7$  fb. The associated uncertainty is mainly due limited statistics. The modeling of background processes is tested in several control regions. The dilepton invariant mass distribution for events with 1 – 6 extra tracks and  $p_T(e\mu) > 30$  GeV is shown in Fig. 35. The background in this sample is dominated by the inclusive  $W^+W^-$  production. Good agreement between data and MC is seen.

Two events pass all selection criteria in data. The number of expected signal events is  $2.2 \pm 0.4$ , where the largest experimental uncertainty is due to the exclusive requirement on the tracks associated with the common vertex. The total background is expected to be  $0.8 \pm 0.2$  events. The  $e\mu$  invariant mass distribution and the  $E_T^{\text{miss}}$  distribution for events in the signal region including the predictions for signal and background are shown in Fig. 36. While the current statistics do not allow a definite answer on the observation of QGCs at the LHC, an upper limit on the cross section at 95% CL is placed with  $\sigma(pp \rightarrow pW^+W^-p \rightarrow pe^\pm\nu\mu^\mp\nu p) < 10.6$  fb.

The larger dataset at  $\sqrt{s} = 8$  TeV could allow a first observation. A first evidence on vector boson scattering and the electroweak production of  $W^\pm W^\pm$  with two jets in  $pp$  collisions at  $\sqrt{s} = 8$  TeV has been recently published[97]. Also a search on the production of  $WW\gamma$  and  $WZ\gamma$  with constraints on anomalous QGCs has become available [98]. The studies of QGCs in general and the scattering of two heavy vector bosons in particular, will play a critical role in the upcoming years of the LHC physics program. Even though the discovery of the Higgs boson provides a unitarization scheme for the otherwise divergent longitudinally polarized vector boson scattering cross section with increasing center-of-mass energy, various scenarios of physics beyond the SM would enhance this scattering process. Last but not least, the scattering of two heavy gauge bosons has never been experimentally observed and its proof would be a further success of the predictive power of the SM.

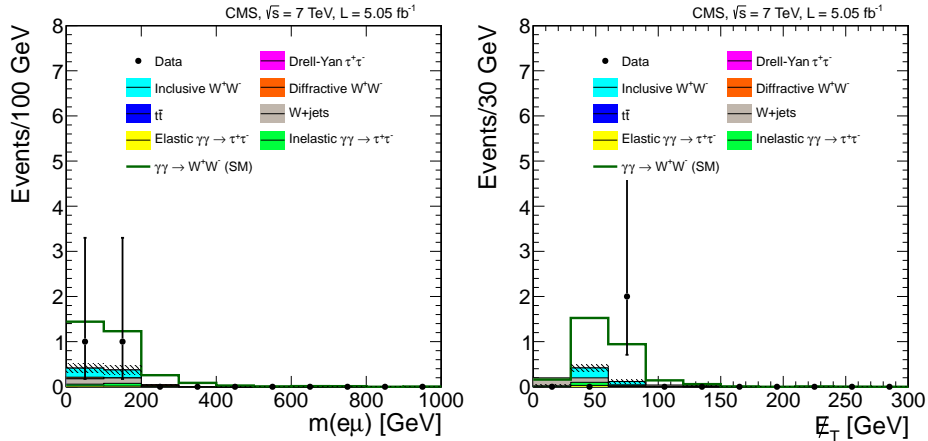


**Figure 36.** CMS: The  $e^\pm\mu^\mp$  invariant mass (left) and  $E_T^{\text{miss}}$  (right) distributions, for events in the signal region with zero extra tracks on the  $e^\pm\mu^\mp$  vertex and  $p_T(e^\pm\mu^\mp) > 30$  GeV. The backgrounds (solid histograms) are stacked with statistical uncertainties indicated by the shaded region, the signal (open histogram) is stacked on top of the backgrounds.

## 7 Summary and Outlook

A large variety of diboson production processes have been studied by the ATLAS and CMS experiments using data from the LHC runs in 2010 and 2011. The diboson results of both experiments have been reviewed in a comprehensive way for a first time in this article.

The measured inclusive cross sections are combined and compared with the Standard Model predictions and a good agreement is observed. Several inclusive cross section measurements are no longer statistically limited and the associated systematic uncertainties are in many cases at the percent level. However, the study of differential distributions can still profit from a larger dataset, allowing for more precise tests of the corresponding theoretical calculations.

The good agreement between theory and experiment was used to set limits on possible extensions of the electroweak sector, such as anomalous triple gauge couplings. While the limits on the anomalous  $WWV$  vertices are still dominated by the results from the LEP experiments, the most stringent constraints on the  $ZZV$ - and  $Z\gamma V$ -vertices are already now given by both collaborations. In addition, the possibility to use fiducial cross section measurements for the testing of these Standard Model extensions in a model independent way has been discussed.

Figure 37 illustrates the dependence of the  $WW$ ,  $WZ$ , and  $ZZ$  production cross sections on the center-of-mass energy. The available LHC measurements for  $\sqrt{s} = 8$  TeV are also shown[99–103]. While the increase of the cross section is only 20% between 7 TeV and 8 TeV, the cross section for the second LHC run at 13-14 TeV is expected to rise by a factor of  $\approx 2.5$ . This increased energy, together with the expected integrated luminosity, will allow for a new round of precision measurements of the electroweak sector to gain a better understanding of the nature of the electroweak symmetry breaking mechanism.

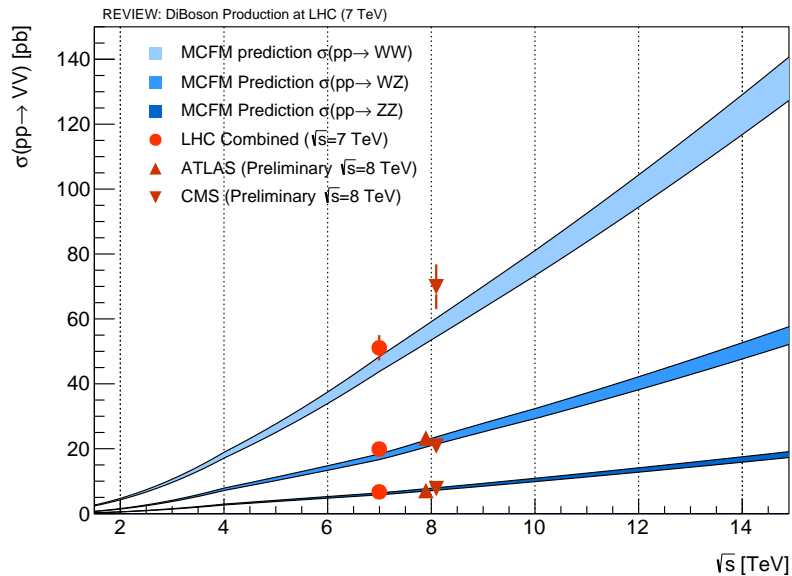


**Figure 37.** Energy dependence of the predicted diboson production cross-sections and the available measurements.

## Acknowledgements

It was our honor to participate during the first LHC run in study of diboson production in a new energy regime. It was a truly collaborative effort of the ATLAS and CMS experiments which have lead to a wide series of wonderful physics measurements. For this review article on the first diboson measurements at the LHC, we would like to thank Dr. Edward Diehl and Prof. Heinz-Georg Sander for their careful review of this paper. In addition, we thank the ATLAS and CMS working group conveners, Sasha Glazov, Alessandro Tricoli, Jeffrey Berryhill and Maxime Gouzevitch for their input. The contribution from Matthias Schott was supported by the Volkswagen Foundation and the German Research Foundation (DFG). The contribution from Junjie Zhu was supported by the Department of Energy Early Career Grant under contract DE-SC0008062 .

## References

- [1] Particle Data Group Collaboration, K. Nakamura et al., *Review of particle physics*, [J.Phys. G37 \(2010\) 075021](#).
- [2] ATLAS Collaboration, G. Aad et al., *Observation of a new particle in the search for the Standard Model Higgs boson with the ATLAS detector at the LHC*, [Phys.Lett. B716 \(2012\) 1–29](#), [arXiv:1207.7214 \[hep-ex\]](#).
- [3] CMS Collaboration, S. Chatrchyan et al., *Observation of a new boson at a mass of 125 GeV with the CMS experiment at the LHC*, [Phys.Lett. B716 \(2012\) 30–61](#), [arXiv:1207.7235 \[hep-ex\]](#).

- [4] ALEPH Collaboration Collaboration, S. Schael et al., *Improved measurement of the triple gauge boson couplings  $\gamma WW$  and  $ZWW$  in  $e^+e^-$  collisions*, [Phys.Lett. \*\*B614\*\* \(2005\) 7–26](#).
- [5] OPAL Collaboration Collaboration, G. Abbiendi et al., *Measurement of charged current triple gauge boson couplings using  $W$  pairs at LEP*, [Eur.Phys.J. \*\*C33\*\* \(2004\) 463–476](#), [arXiv:hep-ex/0308067 \[hep-ex\]](#).
- [6] L3 Collaboration Collaboration, P. Achard et al., *Measurement of triple gauge boson couplings of the  $W$  boson at LEP*, [Phys.Lett. \*\*B586\*\* \(2004\) 151–166](#), [arXiv:hep-ex/0402036 \[hep-ex\]](#).
- [7] DELPHI Collaboration Collaboration, J. Abdallah et al., *Study of triple-gauge-boson couplings  $ZZZ$ ,  $ZZ\gamma$  and  $Z\gamma\gamma$  LEP*, [Eur.Phys.J. \*\*C51\*\* \(2007\) 525–542](#), [arXiv:0706.2741 \[hep-ex\]](#).
- [8] M. S. Neubauer, *Diboson production at colliders*, [Ann.Rev.Nucl.Part.Sci. \*\*61\*\* \(2011\) 223–250](#).
- [9] CDF Collaboration Collaboration, A. Abulencia et al., *Observation of  $WZ$  Production*, [Phys.Rev.Lett. \*\*98\*\* \(2007\) 161801](#), [arXiv:hep-ex/0702027 \[hep-ex\]](#).
- [10] D0 Collaboration Collaboration, V. Abazov et al., *Measurement of the  $p\bar{p} \rightarrow WZ + X$  cross section at  $\sqrt{s} = 1.96$  TeV and limits on  $WWZ$  trilinear gauge couplings*, [Phys.Rev. \*\*D76\*\* \(2007\) 111104](#), [arXiv:0709.2917 \[hep-ex\]](#).
- [11] F. Cascioli, T. Gehrmann, M. Grazzini, S. Kallweit, P. Maierhofer, et al.,  *$ZZ$  production at hadron colliders in NNLO QCD*, [arXiv:1405.2219 \[hep-ph\]](#).
- [12] J. Campbell, K. Ellis, and C. Williams, *Vector boson pair production at the LHC*, [JHEP \*\*1107\*\* \(2011\) 018](#), [arXiv:1105.0020 \[hep-ph\]](#).
- [13] T. Nunnemann, *Vector bosons in new phenomena searches*, Habilitation Thesis, University of Munich (2007).
- [14] M. Schott and M. Dunford, *Review of single vector boson production in  $pp$  collisions at  $\sqrt{s} = 7$  TeV*, EPJC (2014), [arXiv:1405.1160 \[hep-ex\]](#).
- [15] J. Ohnemus and J. Owens, *An  $O(\alpha_s)$  calculation of hadronic  $ZZ$  production*, [Phys.Rev. \*\*D43\*\* \(1991\) 3626–3639](#).
- [16] J. Ohnemus, *An  $O(\alpha_s)$  calculation of hadronic  $W^-W^+$  production*, [Phys.Rev. \*\*D44\*\* \(1991\) 1403–1414](#).
- [17] J. Ohnemus,  *$O(\alpha_s)$  calculations of hadronic  $W^\pm\gamma$  and  $Z\gamma$  production*, [Phys.Rev. \*\*D47\*\* \(1993\) 940–955](#).
- [18] U. Baur, T. Han, and J. Ohnemus, *QCD corrections to hadronic  $W\gamma$  production with nonstandard  $WW\gamma$  couplings*, [Phys.Rev. \*\*D48\*\* \(1993\) 5140–5161](#), [arXiv:hep-ph/9305314 \[hep-ph\]](#).
- [19] U. Baur, T. Han, and J. Ohnemus,  *$WZ$  production at hadron colliders: Effects of nonstandard  $WWZ$  couplings and QCD corrections*, [Phys.Rev. \*\*D51\*\* \(1995\) 3381–3407](#), [arXiv:hep-ph/9410266 \[hep-ph\]](#).
- [20] U. Baur, T. Han, and J. Ohnemus, *QCD corrections and nonstandard three vector boson couplings in  $W^+W^-$  production at hadron colliders*, [Phys.Rev. \*\*D53\*\* \(1996\) 1098–1123](#), [arXiv:hep-ph/9507336 \[hep-ph\]](#).

- [21] U. Baur, T. Han, and J. Ohnemus, *QCD corrections and anomalous couplings in  $Z\gamma$  production at hadron colliders*, *Phys.Rev.* **D57** (1998) 2823–2836, [arXiv:hep-ph/9710416 \[hep-ph\]](#).
- [22] J. M. Campbell and R. K. Ellis, *An Update on vector boson pair production at hadron colliders*, *Phys.Rev.* **D60** (1999) 113006, [arXiv:hep-ph/9905386 \[hep-ph\]](#).
- [23] L. Dixon, Z. Kunszt, and A. Signer, *Vector boson pair production in hadronic collisions at  $O(\alpha_s)$ : lepton correlations and anomalous couplings*, *Phys.Rev.* **D60** (1999) 114037, [arXiv:hep-ph/9907305 \[hep-ph\]](#).
- [24] E. Glover and J. van der Bij, *Vector boson pair production via gluon fusion*, *Phys.Lett.* **B219** (1989) 488.
- [25] W. Hollik and C. Meier, *Electroweak corrections to  $\gamma Z$  production at hadron colliders*, *Phys.Lett.* **B590** (2004) 69–75, [arXiv:hep-ph/0402281 \[hep-ph\]](#).
- [26] E. Accomando, A. Denner, and A. Kaiser, *Logarithmic electroweak corrections to gauge boson pair production at the LHC*, *Nucl.Phys.* **B706** (2005) 325–371, [arXiv:hep-ph/0409247 \[hep-ph\]](#).
- [27] E. Accomando, A. Denner, and S. Pozzorini, *Electroweak correction effects in gauge boson pair production at the CERN LHC*, *Phys.Rev.* **D65** (2002) 073003, [arXiv:hep-ph/0110114 \[hep-ph\]](#).
- [28] E. Accomando and A. Kaiser, *Electroweak corrections and anomalous triple gauge-boson couplings in  $W^+W^-$  and  $W^\pm Z$  production at the LHC*, *Phys.Rev.* **D73** (2006) 093006, [arXiv:hep-ph/0511088 \[hep-ph\]](#).
- [29] M. Billoni, S. Dittmaier, B. Jager, and C. Speckner, *Next-to-leading-order electroweak corrections to  $pp \rightarrow WW \rightarrow 4l$  leptons in double-pole approximation at the LHC*, [arXiv:1311.5491 \[hep-ph\]](#).
- [30] R. Harlander and W. Kilgore, *Next-to-next-to-leading order Higgs production at hadron colliders*, *Phys.Rev.Lett.* **88** (2002) 201801, [arXiv:hep-ph/0201206 \[hep-ph\]](#).
- [31] S. Actis, G. Passarino, C. Sturm, and S. Uccirati, *NLO electroweak corrections to Higgs boson production at hadron colliders*, *Phys.Lett.* **B670** (2008) 12–17, [arXiv:0809.1301 \[hep-ph\]](#).
- [32] J. Butterworth, F. Maltoni, F. Moortgat, P. Richardson, S. Schumann, et al., *The tools and Monte Carlo working group summary report*, [arXiv:1003.1643 \[hep-ph\]](#).
- [33] B. Andersson, G. Gustafson, G. Ingelman, and T. Sjostrand, *Parton fragmentation and string dynamics*, *Phys.Rept.* **97** (1983) 31–145.
- [34] R. Field and S. Wolfram, *A QCD model for  $e^+e^-$  annihilation*, *Nucl.Phys.* **B213** (1983) 65.
- [35] B. Webber, *A QCD model for jet fragmentation including soft gluon interference*, *Nucl.Phys.* **B238** (1984) 492.
- [36] T. Sjostrand, S. Mrenna, and P. Skands, *PYTHIA 6.4 Physics and Manual*, *JHEP* **0605** (2006) 026, [arXiv:hep-ph/0603175 \[hep-ph\]](#).
- [37] T. Sjostrand, S. Mrenna, and P. Skands, *A brief introduction to PYTHIA 8.1*, *Comput.Phys.Commun.* **178** (2008) 852–867, [arXiv:0710.3820 \[hep-ph\]](#).
- [38] G. Corcella, I. Knowles, G. Marchesini, S. Moretti, K. Odagiri, et al., *HERWIG 6: An event*

- generator for hadron emission reactions with interfering gluons (including supersymmetric processes), *JHEP* **0101** (2001) 010, [arXiv:hep-ph/0011363 \[hep-ph\]](#).
- [39] M. Bahr, S. Gieseke, M. Gigg, D. Grellscheid, K. Hamilton, et al., *Herwig++ physics and manual*, *Eur.Phys.J.* **C58** (2008) 639–707, [arXiv:0803.0883 \[hep-ph\]](#).
- [40] T. Gleisberg, S. Hoeche, F. Krauss, M. Schonherr, S. Schumann, et al., *Event generation with SHERPA 1.1*, *JHEP* **0902** (2009) 007, [arXiv:0811.4622 \[hep-ph\]](#).
- [41] J. Alwall, M. Herquet, F. Maltoni, O. Mattelaer, and T. Stelzer, *MadGraph 5 : going beyond*, *JHEP* **1106** (2011) 128, [arXiv:1106.0522 \[hep-ph\]](#).
- [42] J. Campbell, K. Ellis, and D. Rainwater, *Next-to-leading order QCD predictions for  $W + 2$  jet and  $Z + 2$  jet production at the CERN LHC*, *Phys.Rev.* **D68** (2003) 094021, [arXiv:hep-ph/0308195 \[hep-ph\]](#).
- [43] M. Mangano, M. Moretti, F. Piccinini, R. Pittau, and A. Polosa, *ALPGEN, a generator for hard multiparton processes in hadronic collisions*, *JHEP* **0307** (2003) 001, [arXiv:hep-ph/0206293 \[hep-ph\]](#).
- [44] C. Berger, Z. Bern, L. Dixon, F. Febres Cordero, D. Forde, et al., *An automated implementation of on-shell methods for one-loop amplitudes*, *Phys.Rev.* **D78** (2008) 036003, [arXiv:0803.4180 \[hep-ph\]](#).
- [45] M. Mangano, M. Moretti, and R. Pittau, *Multijet matrix elements and shower evolution in hadronic collisions:  $Wb\bar{b} + n$  jets as a case study*, *Nucl.Phys.* **B632** (2002) 343–362, [arXiv:hep-ph/0108069 \[hep-ph\]](#).
- [46] S. Catani, F. Krauss, R. Kuhn, and B. Webber, *QCD matrix elements + parton showers*, *JHEP* **0111** (2001) 063, [arXiv:hep-ph/0109231 \[hep-ph\]](#).
- [47] F. Krauss, *Matrix elements and parton showers in hadronic interactions*, *JHEP* **0208** (2002) 015, [arXiv:hep-ph/0205283 \[hep-ph\]](#).
- [48] S. Frixione and B. Webber, *Matching NLO QCD computations and parton shower simulations*, *JHEP* **0206** (2002) 029, [arXiv:hep-ph/0204244 \[hep-ph\]](#).
- [49] S. Frixione, P. Nason, and C. Oleari, *Matching NLO QCD computations with parton shower simulations: the POWHEG method*, *JHEP* **0711** (2007) 070, [arXiv:0709.2092 \[hep-ph\]](#).
- [50] S. Alioli, P. Nason, C. Oleari, and E. Re, *A general framework for implementing NLO calculations in shower Monte Carlo programs: the POWHEG BOX*, *JHEP* **1006** (2010) 043, [arXiv:1002.2581 \[hep-ph\]](#).
- [51] P. Nadolsky, H.-L. Lai, Q.-H. Cao, J. Huston, J. Pumplin, et al., *Implications of CTEQ global analysis for collider observables*, *Phys.Rev.* **D78** (2008) 013004, [arXiv:0802.0007 \[hep-ph\]](#).
- [52] A. Martin, W. Stirling, R. Thorne, and G. Watt, *Parton distributions for the LHC*, *Eur.Phys.J.* **C63** (2009) 189–285, [arXiv:0901.0002 \[hep-ph\]](#).
- [53] R. Ball, V. Bertone, L. Del Debbio, S. Forte, A. Guffanti, et al., *Precision NNLO determination of  $\alpha_s(M_Z)$  using an unbiased global parton set*, *Phys.Lett.* **B707** (2012) 66–71, [arXiv:1110.2483 \[hep-ph\]](#).
- [54] ZEUS Collaboration, H1 Collaboration Collaboration, A. Cooper-Sarkar, *PDF fits at HERA*, PoS **EPS-HEP2011** (2011) 320, [arXiv:1112.2107 \[hep-ph\]](#).



- [55] K. Hagiwara, R. Peccei, D. Zeppenfeld, and K. Hikasa, *Probing the weak boson sector in  $e^+e^- \rightarrow W^+W^-$* , [Nucl.Phys. \*\*B282\*\* \(1987\) 253](#).
- [56] D. Zeppenfeld and S. Willenbrock, *Probing the three vector boson vertex at hadron colliders*, [Phys.Rev. \*\*D37\*\* \(1988\) 1775](#).
- [57] U. Baur and D. Zeppenfeld, *Probing the  $WW\gamma$  vertex at future hadron colliders*, [Nucl.Phys. \*\*B308\*\* \(1988\) 127](#).
- [58] G. Gounaris, J. Kneur, D. Zeppenfeld, Z. Ajaltouni, A. Arhrib, et al., *Triple gauge boson couplings*, [arXiv:hep-ph/9601233 \[hep-ph\]](#).
- [59] K. Hagiwara, S. Ishihara, R. Szalapski, and D. Zeppenfeld, *Low-energy effects of new interactions in the electroweak boson sector*, [Phys.Rev. \*\*D48\*\* \(1993\) 2182–2203](#).
- [60] G. Bella, D. Charlton, and P. Clarke, *Triple gauge boson parameters*, OPAL Technical Note **TN-492** (1997) .
- [61] U. Baur and E. Berger, *Probing the weak boson sector in  $Z\gamma$  production at hadron colliders*, [Phys.Rev. \*\*D47\*\* \(1993\) 4889–4904](#).
- [62] J. Ellison and J. Wudka, *Study of trilinear gauge boson couplings at the Tevatron collider*, [Ann.Rev.Nucl.Part.Sci. \*\*48\*\* \(1998\) 33–80](#), [arXiv:hep-ph/9804322 \[hep-ph\]](#).
- [63] C. Degrande, N. Greiner, W. Kilian, O. Mattelaer, H. Mebane, et al., *Effective field theory: a modern approach to anomalous couplings*, [Annals Phys. \*\*335\*\* \(2013\) 21–32](#), [arXiv:1205.4231 \[hep-ph\]](#).
- [64] L. Evans and P. Bryant, *The LHC machine*, [JINST \*\*3\*\* \(2008\) S08001](#).
- [65] ATLAS Collaboration, G. Aad et al., *The ATLAS experiment at the CERN Large Hadron Collider*, [JINST \*\*3\*\* \(2008\) S08003](#).
- [66] CMS Collaboration, S. Chatrchyan et al., *The CMS experiment at the CERN LHC*, [JINST \*\*3\*\* \(2008\) S08004](#).
- [67] CMS Collaboration, S. Chatrchyan et al., *CMS tracking performance results from early LHC Operation*, [Eur.Phys.J. \*\*C70\*\* \(2010\) 1165–1192](#), [arXiv:1007.1988 \[physics.ins-det\]](#).
- [68] ATLAS Collaboration, ATLAS Collaboration, *The ATLAS inner detector commissioning and calibration*, [Eur.Phys.J. \*\*C70\*\* \(2010\) 787–821](#), [arXiv:1004.5293 \[physics.ins-det\]](#).
- [69] ATLAS Collaboration, G. Aad et al., *Electron performance measurements with the ATLAS detector using the 2010 LHC proton-proton collision data*, [Eur.Phys.J. \*\*C72\*\* \(2012\) 1909](#), [arXiv:1110.3174 \[hep-ex\]](#).
- [70] S. Chatrchyan et al., *CMS preliminary electron performance results*, TWIKI-Site (2013) .
- [71] CMS Collaboration, S. Chatrchyan et al., *Energy calibration and resolution of the CMS electromagnetic calorimeter in  $pp$  collisions at  $\sqrt{s} = 7$  TeV*, [JINST \*\*8\*\* \(2013\) P09009](#), [arXiv:1306.2016 \[hep-ex\]](#).
- [72] ATLAS Collaboration, G. Aad et al., *Preliminary results on the muon reconstruction efficiency, momentum resolution, and momentum scale in ATLAS 2012  $pp$  collision data*, CERN-CDS **ATLAS-CONF-2013-088** (2013) .
- [73] CMS Collaboration, S. Chatrchyan et al., *Performance of CMS muon reconstruction in  $pp$  collision events at  $\sqrt{s} = 7$  TeV*, [JINST \*\*7\*\* \(2012\) P10002](#), [arXiv:1206.4071 \[physics.ins-det\]](#).

- [74] M. Cacciari, G. Salam, and G. Soyez, *The anti- $k_t$  jet clustering algorithm*, *JHEP* **0804** (2008) 063, [arXiv:0802.1189 \[hep-ph\]](#).
- [75] GEANT4 Collaboration, S. Agostinelli et al., *GEANT4: A simulation toolkit*, *Nucl.Instrum.Meth.* **A506** (2003) 250–303.
- [76] ATLAS Collaboration, G. Aad et al., *Jet energy measurement with the ATLAS detector in proton-proton collisions at  $\sqrt{s} = 7$  TeV*, *Eur.Phys.J.* **C73** (2013) 2304, [arXiv:1112.6426 \[hep-ex\]](#).
- [77] CMS Collaboration, S. Chatrchyan et al., *Particle-flow event reconstruction in CMS and performance for jets, taus, and MET*, CMS Analysis Summary **CMS-PAS-PFT-09-001** (2009) .
- [78] ATLAS Collaboration, G. Aad et al., *Performance of the reconstruction and identification of hadronic tau decays with ATLAS*, CERN CDS (2011) .
- [79] CMS Collaboration, S. Chatrchyan et al., *Performance of tau-lepton reconstruction and identification in CMS*, *JINST* **7** (2012) P01001, [arXiv:1109.6034 \[physics.ins-det\]](#).
- [80] CMS Collaboration, S. Chatrchyan et al., *Measurement of the sum of  $WW$  and  $WZ$  production with  $W + jj$  events in  $pp$  collisions at  $\sqrt{s} = 7$  TeV*, *Eur.Phys.J.* **C73** (2013) 2283, [arXiv:1210.7544 \[hep-ex\]](#).
- [81] Particle Data Group Collaboration, J. Beringer et al., *Review of Particle Physics (RPP)*, *Phys.Rev.* **D86** (2012) 010001.
- [82] G. D’Agostini, *A Multidimensional unfolding method based on Bayes’ theorem*, *Nucl.Instrum.Meth.* **A362** (1995) 487–498.
- [83] ATLAS Collaboration, G. Aad et al., *Measurement of  $W^+W^-$  production in  $pp$  collisions at  $\sqrt{s} = 7$  TeV with the ATLAS detector and limits on anomalous  $WWZ$  and  $WW\gamma$  couplings*, *Phys.Rev.* **D87** (2013) 112001, [arXiv:1210.2979 \[hep-ex\]](#).
- [84] CMS Collaboration, S. Chatrchyan et al., *Measurement of the  $W^+W^-$  cross section in  $pp$  collisions at  $\sqrt{s} = 7$  TeV and limits on anomalous  $WW\gamma$  and  $WWZ$  couplings*, *Eur.Phys.J.* **C73** (2013) 2610, [arXiv:1306.1126 \[hep-ex\]](#).
- [85] CMS Collaboration, S. Chatrchyan et al., *Measurement of the  $WW$ ,  $WZ$  and  $ZZ$  cross sections at CMS*, CERN-CDS CMS-PAS-EWK-11-010 (2011) .
- [86] I. Stewart and F. Tackmann, *Theory uncertainties for Higgs and other searches using jet bins*, *Phys.Rev.* **D85** (2012) 034011, [arXiv:1107.2117 \[hep-ph\]](#).
- [87] L. Lyons, D. Gibaut, and P. Clifford, *How to combine correlated estimates of a single physical quantity*, *Nucl.Instrum.Meth.* **A270** (1988) 110.
- [88] ATLAS Collaboration, G. Aad et al., *Measurement of  $WZ$  production in proton-proton collisions at  $\sqrt{s} = 7$  TeV with the ATLAS detector*, *Eur.Phys.J.* **C72** (2012) 2173, [arXiv:1208.1390 \[hep-ex\]](#).
- [89] CMS Collaboration, S. Chatrchyan et al., *Measurement of  $WZ$  production rate*, CERN-CDS CMS-PAS-SMP-12-006 (2011) .
- [90] ATLAS Collaboration, G. Aad et al., *Measurement of  $W\gamma$  and  $Z\gamma$  production cross sections in  $pp$  collisions at  $\sqrt{s} = 7$  TeV and limits on anomalous triple gauge couplings with the ATLAS detector*, *Phys.Lett.* **B717** (2012) 49–69, [arXiv:1205.2531 \[hep-ex\]](#).

- [91] CMS Collaboration, S. Chatrchyan et al., *Measurement of the  $W\gamma$  and  $Z\gamma$  inclusive cross sections in  $pp$  collisions at  $\sqrt{s} = 7$  TeV and limits on anomalous triple gauge boson couplings*, Phys.Rev.D **89** (2014) 092005, [arXiv:1308.6832 \[hep-ex\]](#).
- [92] ATLAS Collaboration, G. Aad et al., *Measurement of  $ZZ$  production in  $pp$  collisions at  $\sqrt{s} = 7$  TeV and limits on anomalous  $ZZZ$  and  $ZZ\gamma$  couplings with the ATLAS detector*, JHEP **1303** (2013) 128, [arXiv:1211.6096 \[hep-ex\]](#).
- [93] CMS Collaboration, S. Chatrchyan et al., *Measurement of the  $ZZ$  production cross section and search for anomalous couplings in  $2\ell 2\ell'$  final states in  $pp$  collisions at  $\sqrt{s} = 7$  TeV*, JHEP **1301** (2013) 063, [arXiv:1211.4890 \[hep-ex\]](#).
- [94] T. Binoth, M. Ciccolini, N. Kauer, and M. Kramer, *Gluon-induced  $W$ -boson pair production at the LHC*, JHEP **0612** (2006) 046, [arXiv:hep-ph/0611170 \[hep-ph\]](#).
- [95] A. Pukhov, *CalcHEP 2.3: MSSM, structure functions, event generation, batchs, and generation of matrix elements for other packages*, [arXiv:hep-ph/0412191 \[hep-ph\]](#).
- [96] CMS Collaboration, S. Chatrchyan et al., *Search for exclusive two-photon production of  $WW$  pairs in  $pp$  collisions at 7 TeV*, CERN-CDS (2011) .
- [97] ATLAS Collaboration Collaboration, G. Aad et al., *Evidence for electroweak production of  $W^\pm W^\pm jj$  in  $pp$  collisions at  $\sqrt{s} = 8$  TeV with the ATLAS Detector*, [arXiv:1405.6241 \[hep-ex\]](#).
- [98] CMS Collaboration, S. Chatrchyan et al., *A search for  $WW\gamma$  and  $WZ\gamma$  production and constraints on anomalous quartic gauge couplings in  $pp$  collisions at  $\sqrt{s} = 8$  TeV*, [arXiv:1404.4619 \[hep-ex\]](#).
- [99] CMS Collaboration, S. Chatrchyan et al., *Measurement of  $ZZ$  production cross section at 7 and 8 TeV and anomalous gauge couplings limits in  $2\ell 2\nu$  decay channel*, CERN-CDS (2012) .
- [100] CMS Collaboration, S. Chatrchyan et al., *Measurement of  $WW$  production rate*, CERN-CDS (2012) .
- [101] CMS Collaboration, S. Chatrchyan et al., *Measurement of  $WZ$  production rate*, CERN-CDS (2012) .
- [102] ATLAS Collaboration, G. Aad et al., *Measurement of the total  $ZZ$  production cross section in proton-proton collisions at  $\sqrt{s} = 8$  TeV in  $20 \text{ fb}^{-1}$  with the ATLAS detector*, CERN-CDS (2012) .
- [103] ATLAS Collaboration, G. Aad et al., *A Measurement of  $WZ$  Production in Proton-Proton Collisions at  $\sqrt{s} = 8$  TeV with the ATLAS Detector*, CERN-CDS (2012) .